

Development of MRE-based Semi-Active Seat Suspension System for the Mitigation of Whole-Body Vibration

Yimei Wang

A Thesis
In
The Department
Of
Mechanical, Industrial and Aerospace Engineering

Presented in Partial Fulfillment of the Requirements for The Degree of
Master of Applied Science in Mechanical Engineering
Concordia University
Montreal, Quebec, Canada

October 2022

© Yimei Wang, 2022

Concordia University

School of Graduate Studies

This is to certify that the thesis prepared

By: **Yimei Wang**

Entitled: **Development of MRE-based Semi-Active Seat Suspension System for the Mitigation of Whole-Body Vibration**

and submitted in partial fulfillment of the requirements for the degree of

Master of Applied Science in Mechanical Engineering

complies with the regulations of this University and meets the accepted standards with respect to originality and quality.

Signed by the final examining committee:

_____ Chair

Dr. Subhash Rakheja

_____ Examiner

Dr. Amir Aghdam

_____ Examiner

Dr. Subhash Rakheja

_____ Thesis Supervisor

Dr. Ramin Sedaghati

Approved by _____

Dr. S. Narayanswamy, Graduate Program Director

October 21, 2022 _____

Dr. M. Debbabi, Dean

Abstract

Development of MRE-based Semi-Active Seat Suspension System for Mitigating Whole Body Vibration

By Yimei Wang

This thesis concerns with the development, design optimization and control of an MRE-based semi-active seat suspension system to mitigate the whole-body vibration (WBV) transmitted to the human body. The dynamic model of a seated human-body using 4-DOF linear lumped parameter model is firstly derived. Simulation results for seat to head transmissibility (STH) using the 4-DOF model show that the WBV of a human in sitting posture is most sensitive within the frequency range of 4-12 Hz, which is confirmed by the current standard on WBV exposure assessment, ISO 2631/1:1997. The 4-DOF seated human model was then combined with the single DOF model of the seat suspension to derive the coupled 5-DOF human and seat suspension system. The 5-DOF model was utilized to obtain the optimal passive parameters (stiffness and damping) of the seat suspension to minimize the weighted average (rms) vibration acceleration input transmitted to the human operator. The frequency weighting functions, provided by both current (ISO 2631/1:1997) and old (ISO 2631/1:1985, ISO 2631/3:1985) standards, are utilized to realize the effect of weighting factors on the optimal seat suspension designs. Vibration transmissibility from the floor to the operator head in the frequency range up to 100 Hz is also evaluated using the optimal seat suspension parameters obtained using new and old standards on WBV.

An adaptive magneto-rheological elastomer (MRE) vibration isolator was optimally designed to be integrated into the passive seat suspension to semi-actively provide vibration mitigation over a relatively wide range of frequency. The MRE samples were characterized using a rotational rheometer under relatively wide ranges of magnetic and mechanical loadings. Assuming that MREs operate in a linear viscoelastic region, a field-dependent phenomenological model is developed to predict the MREs' mechanical properties (storage and loss moduli) as functions of the excitation frequency and applied magnetic field. The MRE-based vibration isolator is combined with three passive springs (two in parallel, and one in series with the isolator). The proposed configuration in this study, allows relatively large stroke of the seat suspension, while maintaining MREs samples to be operated under low deformation (<30% strain), where the nonlinear strain-softening behavior of MREs is minimum. Results showed that by increasing the applied current from zero to maximum 2 A, the equivalent stiffness of the adaptive seat suspension increased from 8.94 kN/m to 17.5 kN/m under the frequency range where human shows maximum sensitivity (4-10 Hz).

Finally, a particle swarm optimization based fuzzy neural network (PSO-FNN) controller has been designed to evaluate the close-loop performance of the proposed MRE based adaptive seat suspension under different input excitation conditions such as harmonic, random noise, harmonic superimposed with random white noise and bump shock. The simulation results show that PSO-FNN controlled seat suspension compared with the passive suspension can decrease the rms of the vibration acceleration transmitted to the operator's head by nearly 63% and 73% under harmonic superimposed with random white noise, and bump shock excitations, respectively

Acknowledgments

I would like to express my deepest gratitude to my supervisor, Prof. Ramin Sedaghati, for his constant guidance and support, encouragement and patient throughout of thesis research work.

I would like to also express my sincere gratitude to Dr. Hossein Vatandoost for his valuable advice and support during the course of this study.

Finally, I wish to acknowledge the great love of my parents, Dan and Changjian. They supported me with unconditional love and understanding.

Table of Contents

List of Figures	vii
List of Tables	ix
Nomenclature	x
Chapter 1: Introduction and Scope of Thesis	1
1.1 Literature review	3
1.1.1 Passive Suspension	3
1.1.2 Active Suspension.....	4
1.1.3 Semi-active Suspension	4
1.2 Magnetorheological Elastomers (MREs)	5
1.2.1 MRE Materials, Fabrication and Characterization	5
1.2.2 MRE Isolators	6
1.3 Biodynamic Model for Seated Human	8
1.3.1 Lumped-Parameter Models of Seated Human	9
1.4 Motivation and objectives	12
1.5 Thesis Organization	13
Chapter 2: Biodynamic Models of the Seated Human Body	15
2.1 Introduction	15
2.2 Seated Human Lumped Parameter Model.....	16
2.3 Conclusion	21
Chapter 3: Design Optimization of the Passive Seat Suspension	22
3.1 Introduction	22
3.2 Vibration Evaluation of Human Exposure to WBV	23
3.2.1 ISO 2631/1: 1985 and ISO 2631/3:1985	23
3.2.2 Standard ISO 2631/1: 1997.....	26
3.3 5-DOF Coupled Human Body/Seat Suspension Model	30
3.3.1 Transmissibility Analysis.....	30
3.3.2 Design Optimization of Seat Suspension System.....	32
3.4 Conclusion	39
Chapter 4: Development of an Adaptive MRE-Based Vibration Isolator	41
4.1 Introduction	41
4.2 Characterization of MREs	42
4.2.1 Fabrication of MRE samples	42
4.2.2 Shear mode characterization.....	42
4.2.3 Experimental data	44
4.2.4 Formulation of Dynamic Properties of MREs	48
4.3 MRE-based Isolator Design	53

4.3.1	Schematic MRE Isolator	53
4.3.2	Formulation of the Design Optimization	55
4.4	Design Optimization of the Semi-active Seat Suspension System featuring MRE	58
4.4.1	Mathematical description of seat suspension system.....	58
4.4.2	Optimization design of seat suspension system.....	59
4.5	Conclusion	61
Chapter 5: Development of Controllers for the Semi-Active Seat Suspension System		63
5.1	Introduction	63
5.2	The state-space model of 6-DOF system.....	64
5.3	On-Off Skyhook Control.....	67
5.4	Particle Swarm Optimization-Fuzzy Neural Network Control	68
5.5	PSO-FLC training procedure.....	70
5.5.1	Mamdani-Based Fuzzy Neural Network Control	70
5.5.2	Particle Swarm Optimization-Fuzzy Training Algorithm.....	73
5.6	Simulation investigation and discussion	76
5.6.1	Superimposed Harmonic Excitation	76
5.6.2	Random Noise Excitation	78
5.6.3	Simultaneous application of superimposed harmonics and random noise excitation.....	79
5.6.4	Bump Shock Excitation	81
5.7	Conclusion	84
Chapter 6: Conclusion and Future Recommendations		85
6.1	Conclusion	85
6.2	Future Recommendations.....	86

List of Figures

Figure 1.1: Schematic of MRE isolators.....	6
Figure 2.1: A 4-DOF linear lumped parameter model for assessing human exposure to vertical WBV (Wan & Schimmels, 1995).	17
Figure 2.2: Seat-to-head acceleration transmissibility variation with frequency.....	20
Figure 2.3: Driving-point-impedance variation with frequency.	20
Figure 2.4: Apparent mass variation with frequency.	21
Figure 3.1: Measurement locations and directions of WBV for a seated human (ISO 2631/1:1997).	24
Figure 3.2: The variation of acceleration weighting factors with respect to input frequency based on ISO 2631/1:1985 and ISO 2631/3:1985 (Wan & Schimmels, 1997).....	25
Figure 3.3: General procedure for assessing human exposure to vertical WBV in ISO 2631/1:1985 and ISO 2631/3:1985.	25
Figure 3.4: ‘Wk’ Frequency variation of acceleration weighting functions based on ISO 2631/1:1997.	29
Figure 3.5: General Procedure for Assessing Human Exposure to WBV in ISO 2631/1:1997....	29
Figure 3.6: Lumped parameter model of seat suspension system with occupant (Wan, 1998). ...	31
Figure 3.7: Description of band width calculation method based on ISO 2631/1:1997.....	33
Figure 3.8: cs versus objective value with varies ms: (a) ISO 2631/1:1985 and ISO 2631/3:1985; (b) ISO 2631/1:1997	36
Figure 3.9: ks versus objective value with varies ms: (a) ISO 2631/1:1985 and ISO 2631/3:1985; (b) ISO 2631/1:1997.	37
Figure 3.10: Transmissibility from cab-floor to operator head for optimal seat suspension design and no seat suspension: (a) ISO 2631/1:1985 and ISO 2631/3:1985; (b) ISO 2631/1:1997 (c) Comparison of two ISO standards. The solid lines and dotted lines represent the ISO 2631:1997 and ISO 2631: 1985, respectively.	39
Figure 4.1: MREs testing system (a) The MREs testing system; (b) schematic diagram of the rotational parallel-plate setup of the rotary rheometer equipped with magneto-rheology accessory.	43
Figure 4.2: Variation of storage (a) and Loss (b) moduli with respect to applied magnetics flux densities for different loading frequency (Strain amplitude 15%).....	45
Figure 4.3: Variation of storage (a) and Loss (b) moduli with respect to applied magnetics flux densities for different loading frequency (Strain amplitude 30%).....	46
Figure 4.4: Variation of storage (a) and Loss (b) moduli with respect to frequency for different applied magnetics flux densities (Strain amplitude 15%).....	47
Figure 4.5: Variation of storage (a) and Loss (b) moduli with respect to frequency for different applied magnetics flux densities (Strain amplitude 30%).....	48
Figure 4.6: Comparison of storage and loss modulus prediction model with experimental data (Strain 15%).	50
Figure 4.7: Comparison of storage and loss modulus prediction model with experimental data (Strain 30%).	51
Figure 4.8: Comparison of storage and loss modulus prediction model with experimental data	

(Strain 15%).....	52
Figure 4.9: Comparison of storage and loss modulus prediction model with experimental data (Strain 30%).....	53
Figure 4.10: MRE isolator with parallel and series spring.	53
Figure 4.11: Schematic of Designed MRE Isolator: (a) 3D view, and (b) 2D view.	54
Figure 4.12: 6-DOF Lumped parameter model of seated human suspension system with MRE isolator.....	58
Figure 4.13: Schematic of MRE under shear mode.....	60
Figure 4.14: Transmissibility from cab-floor to operator’s head for different currents.....	61
Figure 5.1: 6-DOF Lumped parameter model of seated human suspension system with MRE isolator.....	65
Figure 5.2: PSO-FNN Controller Diagram.....	69
Figure 5.3: FNN controllers’ optimized membership functions	70
Figure 5.4: Architecture of Mamdani-based fuzzy neural network.....	71
Figure 5.5: Flow chart of PSO algorithm.....	75
Figure 5.7: Acceleration of head in time domain under harmonic excitation.....	77
Figure 5.8: Acceleration of head in frequency domain under harmonic excitation.....	77
Figure 5.9: The control current for MRE isolator when seat suspension experiences superimposed harmonic excitation as an input.	78
Figure 5.10: Acceleration of head in time domain under random noise excitation.....	78
Figure 5.11: Acceleration of head in frequency domain under random noise excitation.....	79
Figure 5.12: Current input under random noise excitation.....	79
Figure 5.13: Acceleration of head in time domain under harmonic and random noise excitation.....	80
Figure 5.14: Acceleration of head in frequency domain under harmonic random noise excitation.....	80
Figure 5.15: Current input under harmonic random noise excitation.....	81
Figure 5.16: Acceleration of head in time domain under bump shock excitation.....	82
Figure 5.17: Acceleration of head in frequency domain under bump shock excitation.....	82
Figure 5.18: Current input under bump shock excitation.....	83

List of Tables

Table 1.1: Summary of literature on the development of lumped-parameter seated-human body (Liang & Chiang, 2006).....	10
Table 2.1: Parameter values of 4-DOF model (Wan & Schimmels, 1995).....	17
Table 3.1: Approximate indications of likely reactions to various magnitudes of weighted rms acceleration (ISO 2631/1:1997).....	27
Table 3.2: Parameters of the transfer function of the frequency weightings.	28
Table 3.3: Frequency weighting and multiplying factors in ISO 2631/1:1997.....	30
Table 3.4: Parameter values of 4-DOF human body model (Wan & Schimmels, 1995).....	31
Table 3.5: Optimal values of the seat parameters obtained using ISO 2631 standards.	35
Table 4.1: Identified parameters (strain 15%).....	49
Table 4.2: Identified parameters (strain 30%).....	49
Table 4.3: Optimization Parameters.....	57
Table 4.4: Optimized values of Parameters in MRE Isolator Design.	60
Table 4.5: Output values of optimized seat suspension.	61
Table 5.1: Synthesized Helicopter Floor Reference Signal.	67
Table 5.2: Fuzzy logic control rules of control system.	72
Table 5.4: Vibration reduction under harmonic and random noise excitation.	83
Table 5.5: Vibration reduction under bump shock excitation.	83

Nomenclature

a	Acceleration
a_w	Weighted rms acceleration
A_{core}	Cross-section area of steel core
A_{wire}	Cross-section area of the conductor wire
B	Magnetic field density
c	Damping coefficients of lumped parameter model
C	Damping matrix
C_{MRE}	Damping of MRE isolator
COA	Defuzzification values using center of area method
CD	Current density
d	Desired current value
D_{total}	Total depth of C-shaped MRE isolator
E	Error
f	Frequency
f_n	Natural frequency
F_{MRE}	Viscoelastic force of MRE isolator
G'	Storage modulus
G''	Loss modulus
h_0	Height of bump shock
H	Applied magnetic field
$H(\omega)$	Transfer function
H_h	High-pass filter
H_l	Low-pass filter
H_t	Acceleration-velocity transition filter
H_s	Upward step filter
H_{total}	Total height of C-shaped MRE isolator
I	Applied electrical current

I_n^i	Input of fuzzy neural network controller
J	Error function
k	Stiffness coefficients of lumped parameter model
$k_{\text{MRE off-state}}$	Equivalent stiffness of MRE isolator under zero current input
$k_{\text{MRE on-state}}$	Equivalent stiffness of MRE isolator under maximum current input
K	Stiffness matrix
l	Length of the mean magnetic path of the core
l_{core}	Total length of steel core
l_{MRE}	Length of MRE
L	Path length of steel core
m	Mass coefficients of lumped parameter model
M	Mass matrix
MTVV	Maximum transient vibration value
N	Copper wires' total number of turns
O_m^i	Output of fuzzy neural network controller
p_{id}	Position of the individual best particle
p_{gd}	Position of the global best particle
q, Q	Force vector
\mathcal{R}_t	Total reluctance of the circuit
\mathcal{R}_{MRE}	Reluctance of MRE
$\mathcal{R}_{\text{core}}$	Reluctance of magnetic core
S	Power spectral vector
T	Measurement time
VDV	Vibration dose value
W_k	Weighting filter
W_{total}	Total width of C-shaped MRE isolator
x	Displacement
\dot{x}	Velocity

\ddot{x}	Acceleration
α, β	Coefficients of membership functions of fuzzy inference system
μ	Permeability
μ_0	Vacuum permeability
μ_A, μ_B	Fuzzified values
ω_n	Natural circular frequency
ω_n'	Normalized warped frequency
ω_n^5	Weighting factors of fuzzy neural network controller
η	Learning rate
γ	Shear strain
ϕ	Magnetic flux

Chapter 1: Introduction and Scope of Thesis

Human operators in both air and ground vehicles (particularly rotorcrafts and off-road ground vehicles) are exposed to low frequency whole body vibration (WBV). This is of primary concern as the human body is the most sensitive in the low frequency range (3-12 Hz). Back and neck pains are frequently reported by human operators in both air and ground vehicles. Long term exposure to excessive vibration has been linked to spinal injury and chronic back and neck pain as well as reduced functioning which seriously affects the operational safety. Compared with ground vehicles, rotorcrafts impose WBV in a relatively broad frequency range of 4-20 Hz. It is worth noting that the vibration profile of rotorcrafts is mainly determined by the N/rev fundamental blade passage frequency and its multiples which differs among helicopters depending on the number of blades and rotor speed. The spectra of vibration measured at the aircrew seats in rotorcrafts, however, suggest predominance of WBV in the frequency range, 3-12 Hz in which major resonance frequencies of human body lie (Delahaye et al., 1970, 1982).

WBV can cause severe short-term and long-term diseases, such as musculoskeletal disorders of the spine and head/neck (Griffin & Erdreich, 1991), for the pilots, apart from the fatigue and sickness. WBV exposure is one of the most important factors to consider for seated rotorcraft pilots and crew, since the dominant vibration falls within the frequency range 4 Hz to 12 Hz to which seated humans are most sensitive (ISO 2631/1:1997). ISO 2631 gives the possible hazards of WBV for people exposed to vibration in the short and long terms. Fatigue and lower back pain have been reported as the two main short-term symptoms of WBV exposure (Rakheja, Dewangan, Dong, & Marcotte, 2020; Rakheja, Dewangan, Dong, Marcotte, et al., 2020). According to a survey conducted by Truszczyńska et al. (Truszczyńska et al., 2012), 70% of pilots surveyed complained of lower back pain, with 23% of them citing it as a barrier to flying helicopters.

Long-term exposure to WBV can also cause major health issues such as spinal misalignment and tremor disorders, which are characterized by thickening of the pericardial and artery walls, which can lead to serious heart difficulties (Ballard et al., 2020).

To address the adverse health effects of WBV exposure, many biodynamic models as well as seat suspension systems have been developed to investigate the vibration transmitted to human through the cab floor. Most of the biodynamic models' parameters have been optimized based on the different standards, such as the ISO 2631/1:1985, ISO 2631/3:1985 and ISO 2631/1:1997 for a limited range of frequency. A simple yet accurate biodynamic model needs to be developed

considering a larger range of frequency. Besides, typically three types of vibration isolators have been developed to date, namely, passive, semi-active, and active systems for mitigation of vibration transmitted to human body. The passive systems are capable of providing vibration isolation over a limited frequency range which have been specified at early design stages. Mistuned conditions can adversely affect the performance of the passive systems. While ground vehicles generally utilize passive suspension at the seat to mitigate transmission of WBV, their effectiveness is only limited to certain tuned operating conditions. On the other hand, the vibration isolation for the rotorcrafts' crew is typically done via viscoelastic seat cushions, which are not effective in the critical low frequency range to which human body is more sensitive (Martins, 2017). Active systems can provide significant performance gain compared with passive systems; however, they suffer from the instability and large power consumption as well as complex control hardware. Semi-active systems, on the other hand, can provide reliability and failsafe feature of the passive systems while maintaining the adaptability of the fully active systems.

Developments of smart material with controllable rheological and viscoelastic properties such as magnetorheological fluids (MRFs) and magnetorheological elastomers (MREs) have provided a unique opportunity to develop semi-active adaptive systems utilizing simple control hardware and very low power consumption (Hiemenz et al., 2008). Smart materials with both variable stiffness and damping properties may be effectively utilized for the development of adaptive seat suspension systems to mitigate WBV in wide frequency range in which human is more sensitive. MREs are promising materials for this purpose as they possess both variable stiffness and damping properties. MREs are basically solid analogue of MRFs in which micron-sized ferromagnetic particles (such as carbonyl iron powder) are dispersed in an elastomeric medium instead of a carrier fluid. While several studies have been conducted on development of MRF based semi-active devices (Ma et al., 2021), very limited studies have been conducted on development of MRE-based semi-active vibration suspension systems particularly for crew in rotorcrafts. Choi et al. (Y. T. Choi & Wereley, 2022) developed MRE-based vibration absorbers with limited vibration isolation performance for seat suspension applications. Liu et al. (Liu et al., 2020) also developed a semi-active MRE-based seat suspension system with limited vibration absorption performance due to limited stroke deformation available for MRE. However, this may not be practical for seat suspension which required a large static deflection to accommodate the human weight. Thus, a trade-off yet to be considered between best vibration isolation achievable by MRE based smart

seat suspension system operating in linear viscoelastic region while allowing large static deflection of seat.

This thesis concerns with the development, design optimization and control of an MRE-based semi-active seat suspension system to mitigate the whole-body vibration (WBV) transmitted to the human body. The thesis includes four interrelated phases including: 1- Formulation of a biodynamic seated human lumped model with 4-DOF; 2- Design optimization of a passive suspension using integrated coupled human/seat suspension system to minimize the weight average (rms) acceleration input to human operator; 3- Development of a semi-active MRE-based seat suspension isolator to reduce the WBV over a relatively wide range of frequency while allowing large vertical stroke; and 4- Development of a semi-active control strategy to evaluate the closed loop performance of the proposed adaptive seat suspension system to mitigate WBV.

1.1 Literature review

In the following a systematic literature review has been conducted on the pertinent state of the arts on passive, active ad semi-active suspension seat systems; MRE based semi-active isolators as well as seated human biodynamic models.

1.1.1 Passive Suspension

The simplest and least expensive type of vibration treatment is passive suspension systems, which typically consist of a system of springs and dampers. The natural frequency of the system will not alter when the passive suspensions are designed. Their benefits include low cost, reliability, and a straightforward design procedure. For given external vibration conditions, engineers can design a series of passive suspensions that can reduce WBV within a certain/limited tuned frequency range. For instance, Wan, Y., and Schimmels, J.M. (Wan & Schimmels, 1997) optimally designed a passive seat suspension system with cushion according to the “equivalent subjective sensitivity responses curves” provided by the ISO 2631/1:1985 and ISO 2631/3:1985. The proposed curves for each frequency band are based on the “fatigue-decreased proficiency boundary” curve used at the time (ISO 2631/1:1997). These standard curves give the vibration limit that beyond which would cause fatigue or reduced skill for a given work period. On the other hand, because the vibration isolation parameters of passive seat suspensions are basically fixed, it is difficult to obtain the satisfactory isolation results when the payload or operating condition vary. Wickramasinghe (Wickramasinghe, 2013) investigated the effectiveness of various new passive seat suspensions as

a quick, low-cost solution to improve the vibration performance of helicopter Bell-412. The results show that passive isolation systems provide satisfactory performance to reduce high-frequency band frequencies but is not capable of reducing low-frequency excitation at the frequency range that the human body shows maximum sensitivity (4-10 Hz).

1.1.2 Active Suspension

Active suspension systems provide significant performance gain compared with passive systems as they are capable of mitigating vibration over a wide frequency range. They basically include actuators to provide opposite forces to neutralize input vibration (Fereidooni et al., 2017). The typical actuators are being used for the active systems include, but not limited to, pneumatic, hydraulic, and piezoelectric. Active control systems generally require large power consumption to provide require actuation force. As the active control systems induce energy into system, they should be properly designed to avoid instability. Chen et al. (Chen et al., 2011), for instance, developed a piezoelectric based active seat suspension for a Bell-412 helicopter seat. They installed two stacked piezoelectric actuators on the seat frame to provide counteractive force to mitigate transmitted vibration to aircrew. The active system was able to provide reasonable vibration attenuation in major N/rev higher harmonics of rotor speed beyond 5.4 Hz. Chen et al.(Chen et al., 2009) also reported active seat isolation system for mitigating vibration transmitted to aircrew using modal shaker which was installed between the cabin floor and bottom of the seat as an active member. Results showed significant vibration reduction on the dominant N/rev harmonics of rotor speed. The proposed active mount also revealed a better performance in the low-frequency range of 1/NeV (5.4 Hz). Despite the outperformance of the active control suspension systems compared to passive systems, they are typically massive and bulky systems that practically demand high power consumption, many sensors, actuators, and demand sophisticated control logic.

1.1.3 Semi-active Suspension

Semi-active suspension systems have gained much attention over the last two decades as they can provide effective vibration treatment performance over a relatively wide range of loading frequencies without large power requirement (Jalili, 2002) while maintaining the high reliability of passive systems. A semi-active suspension is an adaptive device with customizable/controllable properties, such as variable damping or stiffness. Smart materials such as magneto-rheological (MR) elastomers (MREs) and MR fluids (MRFs) are recently being used to design semi-active

devices due to their fast responsiveness and controllability under the application of an external magnetic field. In the case of MR material, by applying suitable control schemes, their stiffness, or damping properties can be adapted to obtain a desirable system response. They have advantages compared with active solutions. For instance, the semi-active solution requires less weight and lower power consumption.

Semi-active seat suspension systems based on MR fluids technology have been successfully utilized to alleviate the harmful effects of the transmitted vibration to the seated occupants using their variable damping properties (Gałgorowski, 2012). Hiemenz (Hiemenz et al., 2008), for instance, has developed a semi-active seat suspension system containing two MRF dampers for a SH-60 Seahawk helicopter. However, in the lower frequency range (0.5 Hz to 8 Hz), where the 1/rev component is present, such controllable damping force did not effectively reduce the transmitted vibration to the pilot. It is noted that compared to the higher harmonics, eliminating the 1/rev component necessitates a bigger dissipation of energy. Choi and Wereley (Y.-T. Choi & Wereley, 2005) investigated the biodynamic response mitigation of a semi-active helicopter crew seat suspension based on MR fluid damper under sinusoidal vibration and shock loads. They modeled MR suspension considering body components as pelvis, upper torso, viscera, and head. The results showed that under both loading conditions, the semi-active MR seat suspension revealed higher vibration mitigation performance than both traditional passive shock absorber-based suspension systems and zero-field MR-based suspension systems.

While significant research work has been conducted on the development of MRF base seat suspension systems, very limited studies have focused on the development of semi-active seat suspension featuring MR elastomers (MREs). In contrast to MRFs, MREs can provide both variable and stiffness properties. This unique feature can be effectively used for development of novel MRE based seat suspension systems. Here a brief review of MRE materials is presented, and its application in semi-active vibration control is discussed.

1.2 Magnetorheological Elastomers (MREs)

1.2.1 MRE Materials, Fabrication and Characterization

Magneto-rheological (MR) materials belong to a broader group of materials so-called smart materials, in which their intrinsic mechanical characteristics allow them to respond to variation in the environment such as temperature, electric field, magnetic field, pH, moisture, etc. Among smart

materials, MR materials have been recently gained significant attention due to their fast-responsiveness properties when they expose to the external magnetic field (Morillas & de Vicente, 2020) and their potential for the development of high bandwidth semi-active adaptive devices and systems. MR materials contain two main parts including magnetizable particles and matrix. The magnetizable particles are typically magnetically soft carbonyl Iron particles, namely, (CIPs) due to their high magnetic saturation limit while the matrix can be fluid, foam, gel, and elastomer, which are then called MR fluids, MR foams, MR gels, and MR elastomers, respectively. MR elastomers, simply, MREs, has received much attention in the last two decades as they do not possess the drawbacks of MR materials with a fluid like matrix, in which the magnetizable particle sediment after several hours (Sutrisno et al., 2015). MREs are basically solid analogue of MR fluids (MRFs) in which they are made up of micron-sized ferromagnetic particles, mainly CIPs, dispersed in a nonmagnetic solid polymeric or elastomeric medium like silicone rubber instead of carrier fluid (Qi et al., 2018). MRE is also a remarkable composite with the ability to modify both its stiffness and damping properties (Vatandoost et al., 2020). Field dependent stiffness and damping properties of MRE have made them an ideal candidate for the development of semi-active vibration isolation/mounts devices to mitigate vibration and noise in a wide range of frequency, which have been unanimously confirmed in many studies (Y. Li et al., 2014).

1.2.2 MRE Isolators

MRE isolators have shown many potentials for applications in noise and vibration control, due to their variable stiffness and damping properties under the application of an magnetic field (Du et al., 2011; W. Li et al., 2012). Due to the fast response and their variable mechanical properties, MRE based isolators can provide real-time vibration control over wide range of frequencies. However, as compared with MRF based isolators, MRE isolators typically demand relatively larger and bulkier electromagnet units for their magnetic actuations.

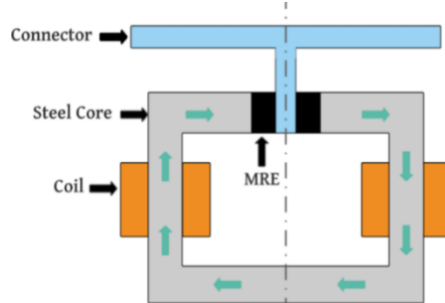


Figure 1.1: Schematic of MRE isolators.

Figure 1.1 shows the schematic of an MRE isolator that contains a closed path C-shaped magnetic core as well as two winding coil units (e.g., air gapped electromagnet). It also includes two MRE samples as well as a connecting bar that attach the MREs to the main system. The magnetic circuits for MRE isolators should be optimally designed in order to meet the design requirements in aerospace or ground vehicle seat applications. They generally include long operational time and low weight configurations while maintaining large magnetic flux density in the air gaps. Thus, designing an electromagnetic unit which can provide enough magnetic field with minimal mass and space remains a continuous challenge in this field which need to be addressed. This is particularly of paramount importance in aerospace applications (e.g., helicopter seat suspensions) as compared to the civil engineering application (MRE bridge mounts) (Yarra et al., 2018).

Despite the extensive research on the development of MRE-based vibration isolation devices, there exists a few studies for seat applications. For instance, Du et. al (Du et al., 2011) presented a conceptual design for an MRE based semi-active vibration isolator for application in vehicle seat suspension systems. The vibration control effect of the MRE isolator is evaluated in terms of driver body acceleration responses under both bump and random road conditions. Their results showed that the proposed control strategy (sub-optimal H_∞) achieves better vibration reduction performance than conventional on-off control. Moreover, Li et. al (W. Li et al., 2012) prototyped an MRE-based vibration isolator, where MRE materials operates in both shear and compression modes, for a seat suspension system. The proposed semi-active suspension systems revealed vibration isolation improvements of about 12.5% and 22% as compared with passive-suspension system under white noise and bump excitations, respectively.

The limited research studies on MRE-based semi-active seat suspension systems is due to the fact that seat suspensions practically undergo large deformation (~10-15cm) while MREs show nonlinear strain softening behavior at large deformation (Dargahi et al., 2019). At the same time, a large stiffness is required to avoid excessive deflection due to pilot weight. In contrast, low stiffness coupling helps to reduce the vibration transmissibility and the resonant frequency of the isolation system. However, mechanical coupling with a low stiffness will decrease the loading capacity of the system, which is disadvantageous in the seating suspension systems that require high loading capacity to support the weight of the driver and passenger.

Due to these complexities and conflicting requirements associated with vertical vibration

isolation of seat suspensions, researchers have had tendency to develop horizontal vibration isolation of seats using negative stiffness properties of MREs. Sun et al., (Sun et al., 2015) developed a novel negative stiffness multilayer MRE based vibration isolator for horizontal vibration mitigation of a seat. The MRE-based vibration isolator consists of an electromagnetic coil and two permanent magnets to realize negative stiffness characteristic. Results demonstrated that the proposed MRE-based vibration isolator decreased the output seat acceleration under different excitations as 44.6% (5 Hz), 44.4% (7 Hz), and 27.4% (10 Hz).

Nevertheless, vertical vibration of seat has been mostly associated with WBV problems and needed to be reduced effectively. In this regard, MRE-based vibration isolators has been rarely investigated (W. Li et al., 2012). As mentioned above, this is attributable to the fact that the stiffness of seat suspensions is required to be designed as soft as possible to have a lower natural frequency (ω_n) than excitation frequencies of interest, thereby providing effective vibration isolation above $\sqrt{2}\omega_n$ (Y. T. Choi & Wereley, 2022). At the same time, a large stiffness is required to avoid excessive deflection due to seated occupant weight. For instance, Liu et al. (Liu et al., 2020) developed an MRE-based semi-active seat suspension to provide vertical vibration isolation for seat applications. However, to avoid softening effect of MRE materials at large deformation, a low stroke limit of 5 mm was considered in their design, which may limit their practical application for seat suspensions. A semi-active suspension system based on MREs is yet to be investigated that can 1- allow large vertical deformation of the seat while maintaining MRE to operate within limited deformation regime at the same time, 2- tolerating the pilot weight, and 3- providing sufficient frequency shift/vibration isolation.

1.3 Biodynamic Model for Seated Human

In order to develop an effective control algorithm for vibration suppression of seated occupant using semi-active seat suspensions, a biodynamic model is required. The goal of creating a human model is to correctly and effectively measure the human reactions to a range of stimuli without putting real subjects in dangerous situations. The human body is a complex dynamic system whose mechanical properties change over time and across individuals (Rakheja, Dewangan, Dong, & Marcotte, 2020). As a result, many mathematical models have been developed over the past few decades to effectively simulate human body's dynamic behavior. Overly complex models can lead to predictions may unnecessarily increase computational costs while still far from experimental

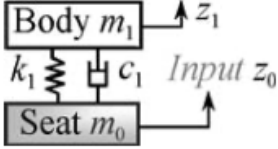
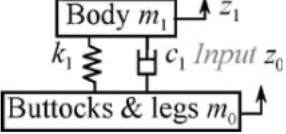
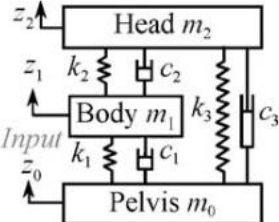
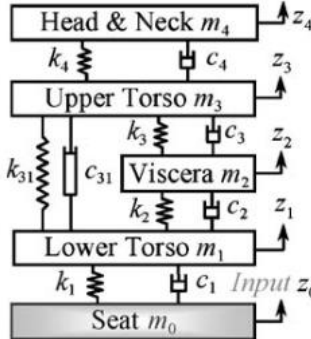
data (Wan, 1998). Lumped parameter models are models that consider the human body as a series of concentrated masses linked by linear springs and dampers. Due to their simplicity, lumped human models can be effectively used at early stages of design to assess the performance of suspension isolation systems. Wan and Schimmels developed a 4-DOF model that best fits the available experimental findings (Wan & Schimmels, 1995). This model can be simply used to examine the biodynamic reactions of sitting human subjects to vertical whole-body vibration.

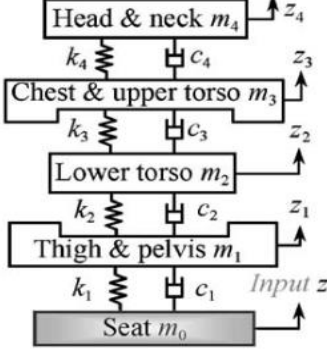
The human body is made up of several different body systems. Not only the mechanical characteristics of individual body parts can be different, but the mechanical properties of distinct bodies also behave differently. A great variety of models in various domains have been suggested to best represent the dynamic responses of the human body from the 1960s (Coermann, 1962) to the present (Gan et al., 2013; Zhang et al., 2015). These models are classified as lumped-parameter models, finite element models, and multibody models based on their modelling methodologies. Here each type of modeling approaches their pros and cons are discussed.

1.3.1 Lumped-Parameter Models of Seated Human

The biodynamic response of a seated person exposed to vertical vibration has been extensively evaluated in terms of ‘to-the-body’ and ‘through-the-body’ indexes (Rakheja, Dewangan, Dong, & Marcotte, 2020). To-the-body measures including the driving-point mechanical (DPM) impedance, and apparent mass (AM), while through-the-body measure relates to the discharge of seat vibration to the body parts including neck and head. Consideration of these measures have yielded development of many biodynamic models depending on the target of analysis. Impact tests were utilized by Cesari and Ramet (Cesari & Ramet, 1982) to determine the maximum fracture force on the pelvis and subsequently presenting a pelvic injury criteria. Axial impact experiments were performed on 19 human corpses by Alem et al. (Alem et al., 1984) to examine the mechanical characteristics of the head, neck, and spine structure and to establish the injury standard. In addition, many data have been generated by different researchers to characterize these response functions using widely varying experimental conditions (Boileau & Rakheja, 1998; Coermann, 1962; Muksian & Nash Jr, 1974; Wan & Schimmels, 1995). A more appropriate summary of these data is presented using simulations of the mathematical models listed in Liang’s study (Liang & Chiang, 2006), under a well-defined range of assumptions. Below, a brief overview of the literature of the lumped-mass models is summarized in Table 1.1.

Table 1.1: Summary of literature on the development of lumped-parameter seated-human body (Liang & Chiang, 2006).

Author, year	Model's schematic	Description
1-DOF Model (Coermann, 1962)		To simulate human body weight, a 56.8-kg mass was considered in this model. To simulate the physical attribute of a sitting human, a system of springs and dampers are used to modify the human-seat contact.
2-DOF Model (Wei & Griffin, 1998)		For the purpose of evaluating seat design, the seated body was created with two independent mass parts. It has a total mass of 51.2kg. The “Buttock and legs m_0 ” mass segment was considered to connect directly with a set of seat spring and damper in the analysis, with seat mass ignored and not included in the human-seat system.
2-DOF Model (Muksian & Nash Jr, 1974)		The seated body was constructed with three separate mass segments, with a total mass of 79.83kg.
4-DOF Model (Wan & Schimmels, 1995)		With a total human mass of 60.67kg, the seated body was made up of four independent mass segments connected by five sets of springs and dampers. This linear system is solved using the frequency-domain approach. The input excitation's sinusoidal acceleration is measured from the seat with a maximum amplitude of 5.0 m/s^2 . The fitness of 91% for seat-to-head (STH) transmissibility, 80.1% for DPM, and 86.8% for AP mass based on the projected data, with peak values at roughly 4.0, 7.2, and 3.7 Hz, respectively. Due to the linearity and simplicity which greatly facilitate the analysis and also good fitness to experimental data as well as , this model

		is likely the best for predicting the biodynamic functions listed above.
4-DOF Model (Boileau & Rakheja, 1998)		A linear model was constructed based on experimental results on live human bodies. This model has a total mass of 55.2 kg and is made up of four mass segments connected by four sets of springs and dampers. All physical parameters m_i , c_i , and k_i are identified using an optimization technique that includes human body anthropometric and biomechanical restrictions as well as measurements of STH, DPM, and AP as objective functions.

Analysis of Table 1.1 shows a gradual improvement in modeling of seated human body considering different parts of body. Each model was employed for further vehicle dynamic and vibration control analysis. Unlike the other models developed, Wan (Wan & Schimmels, 1995) presented a 4-DOF model for seated human body considering three experimental indexes, namely, STH transmissibility, DPM impedance, and AM. The corresponding model's parameters were obtained, which revealed the fitness of 91% for STH transmissibility, 80.1% for DPM, and 86.8% for AP mass based on the projected data, with peak values at roughly 4.0 Hz, 7.2 Hz, and 3.7 Hz, respectively. Furthermore, another 4-DOF system was developed by Boileau et al. (Boileau & Rakheja, 1998) in which the model's parameters were optimized considering the experimental measurements including human body anthropometric and biomechanical restrictions as well as measurements of STH transmissibility, DPM impedance, and AP mass as objective functions.

Parameters of seat suspension models should be optimized to yield maximum reduction of vibration transmitted to human body. For the linear seat suspension, Wan et al. (Wan & Schimmels, 1997) observed that the selection of the seat stiffness is much more important than selection of the seat mass. Besides, the optimal seat damping characteristic depends significantly on the selection of vibration sensitivity standard, the lower bound of the stiffness, and on vibration environments. Additionally, they noticed that the nonlinear seat suspensions outperform the linear seat suspensions, and its related results were indicative of the greater influence of vibration environments on the optimal values of all seat parameters particularly the optimal nonlinear damping value, when compared to linear seat suspensions.

As discussed previously mentioned, at early stages of design, the performance evaluation of the seat suspension system on reduction of WBV can be effectively realized using simple yet accurate lumped seated human models. The current developed biodynamic models for seated human body together with seat suspension system have not considered the new standard (ISO 2631/1:1997) criterion related to to-the-body (DPM impedance, and AM) as well as through-the-body (STH transmissibility). This can yield relatively considerable errors in the design of effective seat suspension systems. The 4-DOF model developed by Wan. et al. (Wan & Schimmels, 1997) has shown to accurately capture the essential vibration characteristics of a seated human body and thus can be combined with seat suspension system to effectively assess the performance of the seat suspension design for attenuation of the WBV.

1.4 Motivation and objectives

The semi-active MRE-based suspension systems have been, mostly, developed for horizontal vibration of the seat. The review of relevant reported studies indicated only limited knowledge on the design and control of MRE-based semi-active suspension systems for vertical isolation of the seats, although with limited success in terms of frequency shift, maximum allowable stroke, and limited space/weight. Additionally, the current developed biodynamic models for seated human body together with seat suspension system have not considered the new standard (ISO 2631/1:1997) criterion related to to-the-body (DPM impedance, and AM) as well as through-the-body (STH transmissibility). This can yield relatively considerable errors in the design of effective seat suspension systems. Tuning the parameters of the current state-of-the-art multi-degree of freedom seat suspension models according to the latest standard for predicting seated human body characteristics is thus vital for accurate design of seat suspensions. Building essential knowledge on the roles of optimal parameters of lumped mass biodynamic model together with seat suspension system are vital for establishing design guidance for semi-active seat suspension applications.

The overall goal of this thesis research is thus to develop a new semi-active MRE-based vibration isolator with minimal weight and maximum frequency shift for vertical vibration isolation of seat on the basis of an improved system with tuned lumped mass parameters according to the new standard (ISO 2631:1997). The specific goals of this research thesis are summarized below:

- a) Validate the 4-DOF lumped mass biodynamic model for seated human according to the criterion (both the “to-the-body” (DPM impedance, and AM) and “through-the-body” (STH transmissibility) measures);
- b) Design optimization of a passive seat-suspension system using 5-DOF lumped human/seat suspension coupled model based on standard ISO 2631/1: 1997;
- c) Formulating a design optimization strategy for a C-shaped MRE-based vibration isolator with minimal mass and maximum MR effect;
- d) Develop a semi-active seat suspension system employing an MRE-isolator unit together with parallel and series passive springs for vertical isolation of the seat. The suspension system should allow sufficient vertical deformation (stroke) of seat under human body weight while maintaining MRE to operate within limited deformation regime (linear region) and also it should provide sufficient frequency shift/vibration isolation;
- e) Formulate an advanced semi-active control strategy to achieve better vibration attenuation performance of the seat compared with passive suspension.

1.5 Thesis Organization

This research thesis is organized into 6 chapters. Chapter 1 includes the introduction and scope of the thesis as well as pertinent literature review and motivation and objectives of the present research. Chapter 2 presents a 4-DOF human body model and its dynamic properties such as seat-to-head transmissibility (STH), driving-point mechanical impedance (DPM), apparent mass (AM) are analyzed. Chapter 3 provides a systematic approach to design a passive seat suspension system by compiling with ISO 2631 standards (ISO 2631: 1985 & 1997). A design optimization problem has been formulated for the passive seat suspension incorporating standard ISO 2631/1:1997. The vibration transmitted to the human is weighted by its perceived discomfort to the average human and averaged in the frequency domain. Chapter 4 presents design optimization of an MRE-based vibration isolator equipped with a C-shaped electromagnet. The proposed MRE-based vibration isolator is expected to be used for seat suspension applications in the aerospace sector. A parallel-series seat suspension system is also designed and integrated with MRE isolator. The objective is to maximize frequency shift of the isolator under maximum allowable magnetic field considering the weight constraint while allowing the MRE undergo an allowable deformation. Chapter 5

presents design of a controller consists of particle swarm optimization based fuzzy neural network algorithm to adjust the current input of the MRE isolator according to the vibration input conditions. A conventional skyhook on-off controller is also synthesized to compare with the proposed PSO-FNN controller. The outcomes of the present research study together with potential future research directions are provided in Chapter 6.

Chapter 2: Biodynamic Models of the Seated Human Body

2.1 Introduction

In order to implement the various control algorithms together with design development of semi-active seat suspensions, a simple biodynamic model is of fundamental necessity. The human body is a complex dynamic system whose mechanical properties change over time and across individuals. As a result, many mathematical models have been developed over the past few decades. The description of seated human biodynamic responses depends on various modeling techniques, such as lumped parameter models, finite element models, and multibody models. The goal of creating a human model is to correctly and effectively measure human reactions to a range of stimuli without putting real subjects in dangerous situations. Overly complex models may not only be computationally expensive for parameter identification it may also lead to predictions that are far from experimental results (Wan, 1998). Lumped parameter models consider the human body as a series of concentrated masses linked by linear springs and dampers. These types of models are, indeed, beneficial for assessing the suspension isolation performance as the dynamic human/seat response can be easily modeled and analyzed by coupling the seated-human lumped model to the lumped seat suspension model, the Wan and Schimmels (Wan & Schimmels, 1997), for instance, presented a simple, yet accurate 4-DOF model that best fits the available test findings. In this research the 4-DOF model of the Wan and Schimmels has been employed to identify optimal stiffness and damping of the passive seat suspension and also assess the performance of the developed adaptive MRE-based seat suspension.

In this chapter first the biodynamic model of the seated human body is formulated. According to Wan's biodynamic model (Wan & Schimmels, 1995), the seated human body system can generally be divided into four parts: head, upper torso, viscera and lower torso. If the effects of lateral and horizontal vibrations are not taken into account, the kinetic model of the seated human upper body system can be simplified by a 4-DOF vertical vibration model as shown in Figure 2.1. The mathematical expressions of STH, DPM and AM are derived to describe the three responses of displacement, velocity and acceleration of human body, and the simulation and analysis of the 4-DOF human body vertical vibration model based on STH, DPM and AM are performed.

2.2 Seated Human Lumped Parameter Model

The lumped parameter model is a discrete model that its characteristic parameters can be easily identified using available experimental data. As mentioned before, a human body lumped parameter model should satisfy both linearity and simplicity to facilitate the analysis. Therefore, choosing a model that meets the above requirements and enables the design of subsequent seat suspension is essential. A 4-DOF seated human lumped parameter model was promoted in 1995 by Wan and Schimmel for vertical random vibration simulation (Wan & Schimmels, 1995). In their research, the seat suspension delivers the principal vibration input to the seated operator. Consequently, only the operator's head, neck, upper torso, viscera, lower torso with a total mass of 60.67 kg are considered. This model is a mechanical vibration response equivalent model, which equates the human body to mechanical elements such as mass, spring, and damping. The parameters of 4-DOF model were identified by comparing the simulation results with those of experimental results on human subjects. They have shown that the model matched the experimental data (Liang & Chiang, 2006) from 0.1 Hz to 80 Hz, which improved prediction accuracy over a broader range of vibration frequencies compared to previous studies. The lumped parameter model and the parameter values are illustrated in Figure 2.1 and Table 2.1 respectively.

It is noted that in Figure 2.1, parameters m_1, m_2, m_3, m_4 are, respectively, the mass of the lower torso, viscera, upper torso and head/neck and k_1, k_2, k_3, k_4 and c_1, c_2, c_3, c_4 are the stiffness and damping of the above-mentioned parts of the human body. Coordinates x_1, x_2, x_3, x_4 are the displacement of the center of gravity of each part of the human body and x_0 is the displacement excitation to the human at lower torso (output from seat).

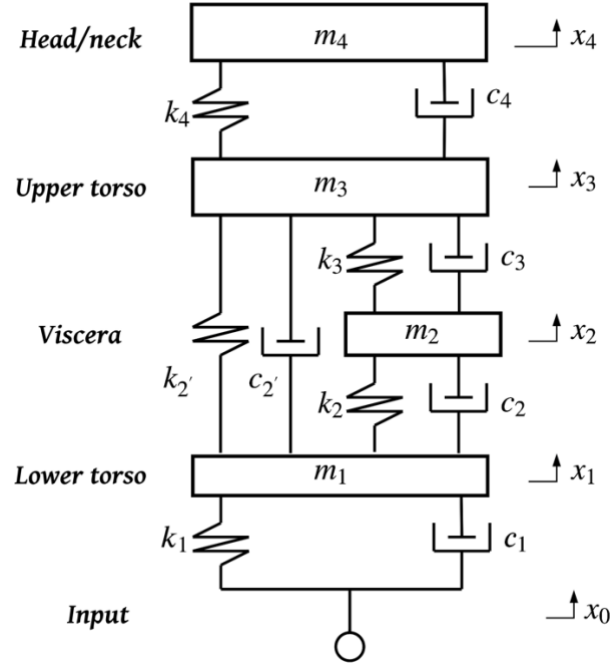


Figure 2.1: A 4-DOF linear lumped parameter model for assessing human exposure to vertical WBV (Wan & Schimmels, 1995).

Table 2.1: Parameter values of 4-DOF model (Wan & Schimmels, 1995).

m_4 (kg)	4.17	k_4 (N · m ⁻¹)	134400	c_4 (N · s · m ⁻¹)	250
m_3 (kg)	15	k_3 (N · m ⁻¹)	10000	c_3 (N · s · m ⁻¹)	200
—	—	$k_{2'}$ (N · m ⁻¹)	192000	$c_{2'}$ (N · s · m ⁻¹)	909.09
m_2 (kg)	5.5	k_2 (N · m ⁻¹)	20000	c_2 (N · s · m ⁻¹)	330
m_1 (kg)	36	k_1 (N · m ⁻¹)	49341.6	c_1 (N · s · m ⁻¹)	2475

Using the Newton's second law, the governing differential equations describing the dynamic behavior of the 4-DOF model can be described as follows:

$$m_4 \ddot{x}_4 = k_4(x_3 - x_4) + c_4(\dot{x}_3 - \dot{x}_4) \quad (2-1)$$

$$m_3 \ddot{x}_3 = k_2'(x_1 - x_3) + c_2'(\dot{x}_1 - \dot{x}_3) + k_3(x_2 - x_3) + c_3(\dot{x}_2 - \dot{x}_3) - k_4(x_3 - x_4) - c_4(\dot{x}_3 - \dot{x}_4) \quad (2-2)$$

$$m_2 \ddot{x}_2 = k_2(x_1 - x_2) + c_2(\dot{x}_1 - \dot{x}_2) - k_3(x_2 - x_3) - c_3(\dot{x}_2 - \dot{x}_3) \quad (2-3)$$

$$m_1 \ddot{x}_1 = k_1(x_0 - x_1) + c_1(\dot{x}_0 - \dot{x}_1) - k_2'(x_1 - x_3) - c_2'(\dot{x}_1 - \dot{x}_3) - k_2(x_1 - x_2) - c_2(\dot{x}_1 - \dot{x}_2) \quad (2-4)$$

where $x_0, \dot{x}_0, \ddot{x}_0$ are the input displacement, velocity and acceleration.

Three evaluation indices are widely used to commonly evaluate and characterize the biodynamic response of the seated human body: seat-to-head transmissibility (STH), driving-point mechanical impedance (DPM), and apparent mass (AP). For the convenience of assessing the model's dynamic performance, governing equations, Eqs. (2-1) to (2-4), can be cast in matrix form as:

$$[M]\{\ddot{x}\} + [C]\{\dot{x}\} + [K]\{x\} = [B]\{q\} \quad (2-5)$$

where $[M]$ is the mass matrix, $[C]$ is the damping matrix, $[K]$ is the stiffness matrix, $[B]$ and $\{q\}$ are the force matrix and vector due to the excitation. Besides, $\{\ddot{x}\}$, $\{\dot{x}\}$, $\{x\}$ are the acceleration, velocity and displacement vectors, respectively.

$$M = \begin{bmatrix} m_4 & 0 & 0 & 0 \\ 0 & m_3 & 0 & 0 \\ 0 & 0 & m_2 & 0 \\ 0 & 0 & 0 & m_1 \end{bmatrix} \quad (2-6)$$

$$K = \begin{bmatrix} k_4 & -k_4 & 0 & 0 \\ -k_4 & k_{2'} + k_3 + k_4 & -k_3 & -k_{2'} \\ 0 & -k_3 & k_2 + k_3 & -k_2 \\ 0 & -k_{2'} & -k_2 & k_1 + k_{2'} + k_2 \end{bmatrix} \quad (2-7)$$

$$C = \begin{bmatrix} c_4 & -c_4 & 0 & 0 \\ -c_4 & c_{2'} + c_3 + c_4 & -c_3 & -c_{2'} \\ 0 & -c_3 & c_2 + c_3 & -c_2 \\ 0 & -c_{2'} & -c_2 & c_1 + c_{2'} + c_2 \end{bmatrix} \quad (2-8)$$

$$B = \begin{bmatrix} 0 & 0 \\ 0 & 0 \\ 0 & 0 \\ k_1 & c_1 \end{bmatrix} \quad (2-9)$$

$$\{q\} = \begin{bmatrix} x_0 \\ \dot{x}_0 \end{bmatrix} \quad (2-10)$$

By using Fourier transform, equation (2-5) can be transformed to frequency domain as:

$$-\omega^2[M]\{x(j\omega)\} + j\omega[C]\{x(j\omega)\} + [K]\{x(j\omega)\} = [B]\{Q(j\omega)\} \quad (2-11)$$

where:

$$Q(j\omega) = \begin{bmatrix} 1 \\ (j\omega) \end{bmatrix} \{x_0(\omega)\} \quad (2-12)$$

$$\{x(j\omega)\} = [x_4(j\omega), x_3(j\omega), x_2(j\omega), x_1(j\omega)] \quad (2-13)$$

Let

$$[A] = -\omega^2[M] + j\omega[C] + [K] \quad (2-14)$$

thus, we can write:

$$[A]\{x(j\omega)\} = [B]\{Q(j\omega)\} \quad (2-15)$$

solving for $x(j\omega)$ yields:

$$\{x(j\omega)\} = [A]^{-1}[B]\{Q(j\omega)\} \quad (2-16)$$

and using Eq. (2-12):

$$\{x(j\omega)\} = [A]^{-1}[B] \begin{bmatrix} 1 \\ (j\omega) \end{bmatrix} \{x_0(\omega)\} \quad (2-17)$$

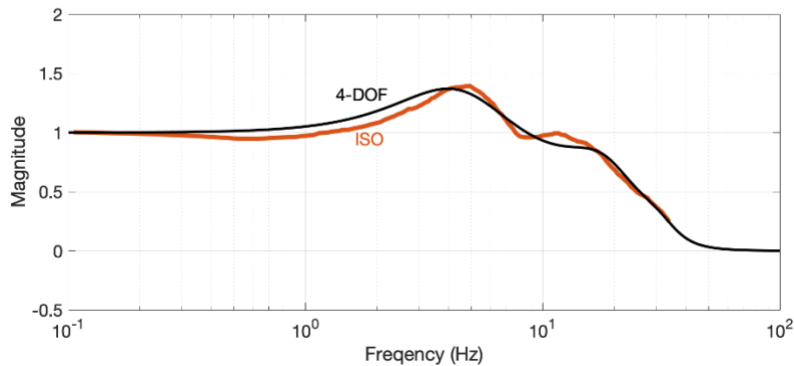
Therefore, the general transfer function of human body response may be described as:

$$H(\omega) = [H_4(\omega), H_3(\omega), H_2(\omega), H_1(\omega)]^T = [A]^{-1}[B] \begin{bmatrix} 1 \\ (j\omega) \end{bmatrix} \quad (2-18)$$

Seat-to-head (STH) acceleration transmissibility is a complex non-dimensional ratio of the head response acceleration to the imposed vibration acceleration at the seat-body interface which can be mathematically represented as:

$$STH(j\omega) = \frac{\{\ddot{x}_4(j\omega)\}}{\{\ddot{x}_0(j\omega)\}} = \frac{-\omega^2\{x_4(j\omega)\}}{-\omega^2\{x_0(j\omega)\}} = H_4(\omega) \quad (2-19)$$

Figure 2.2 displays a plot of seat-to-head (STH) transmissibility magnitude (**linear ratio**) versus frequency and a plot of transmissibility phase versus frequency. The curve “4-DOF” is for the 4-DOF seated human model shown in Figure 2.1 with parameters provided in Table 2.1. The curve “ISO” is provided by ISO 7962:1987 (ISO 7962:1987).



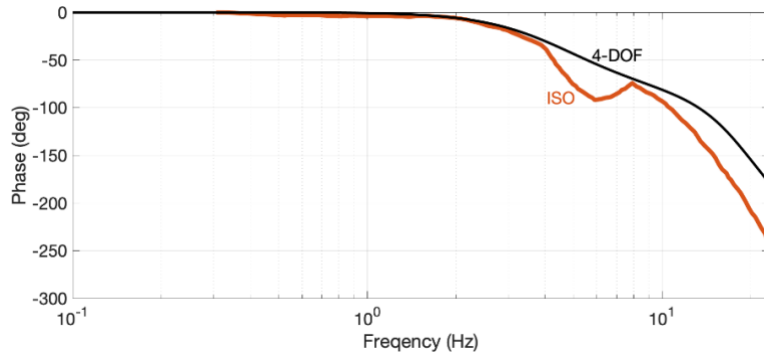


Figure 2.2: Seat-to-head acceleration transmissibility variation with frequency.

The driving-point impedance (DPM) is the complex ratio of force to the velocity at the same position in system (here at seat location).

$$DPM(j\omega) = \frac{(k_1 + j\omega c_1)[x_0(\omega) - x_1(\omega)]}{j\omega x_0(\omega)} \quad (2-20)$$

Figure 2.3 displays the driving-point impedance (DPM) versus frequency and the impedance phase versus frequency of the 4-DOF seated human model and the ISO 5982:1981 identified curve. The ‘ISO’ curve is from experimental data and the ‘ISO’ is obtained by averaging responses of human subjects.

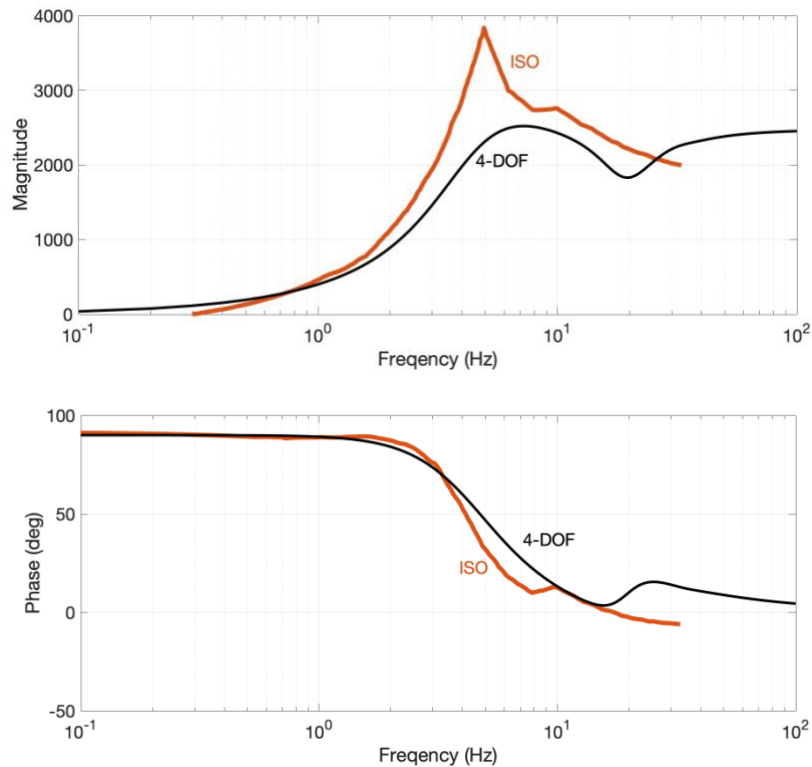


Figure 2.3: Driving-point-impedance variation with frequency.

The apparent mass (AM) is the relationship between the applied excitation force (between seat and lower torso) and the acceleration response at seat interface which can be, mathematically described as:

$$AM(j\omega) = \frac{(k_1 + j\omega c_1)[1 - H_1(\omega)]}{-\omega^2} \quad (2-21)$$

in which $H_1(\omega) = \frac{x_1(j\omega)}{x_0(j\omega)}$. Figure 2.4 shows variation of the AM amplitude and phase versus frequency for the employed 4-DOF model shown in Figure 2.4.

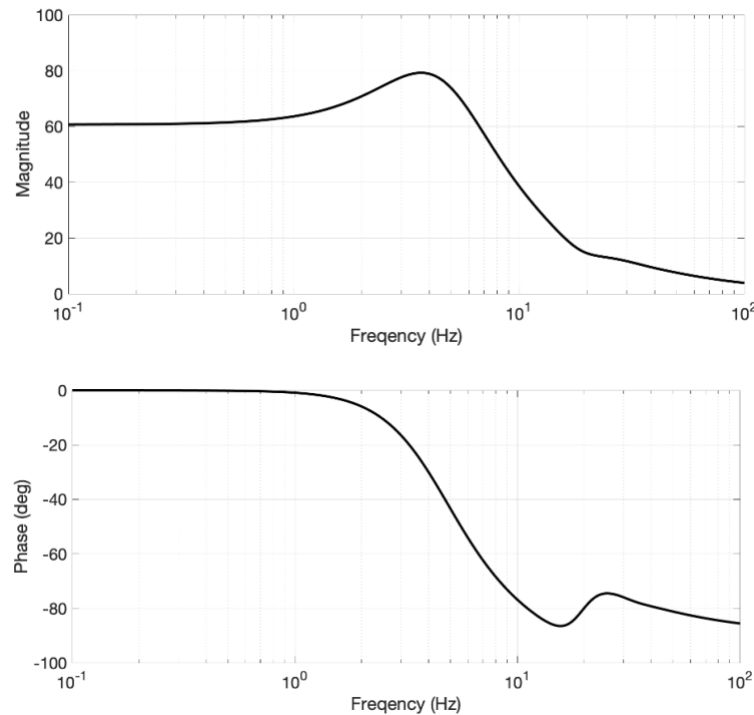


Figure 2.4: Apparent mass variation with frequency.

Results presented in Figures 2.2 to 2.4 are similar to those obtained by Wan & Schimmels (Wan & Schimmels, 1995) which agree reasonably well with experimental data on human subjects.

2.3 Conclusion

Wan's 4-DOF human body model can predict accurately the seat-to-head (STH) transmissibility, driving-point impedance (DPM) and apparent mass (AM). The changing trend of each curve is very smooth, which provides a very important basis for the design and control of subsequent seat suspension system. As mentioned above, the human body dynamics model needs to meet the characteristics of accuracy, simplicity and easily analysis. The 4-DOF lumped biodynamic model of the seated human presented in this chapter meets the above criteria.

Chapter 3: Design Optimization of the Passive Seat Suspension

3.1 Introduction

When human operators (i.e., helicopter pilots) are exposed to WBV for long periods of time, they can experience a series of health problems such as low back pain, degenerative disorders of the spine, and spinal disc disease and failure. Even short-term exposure to WBV can cause muscle fatigue and discomfort (Wickramasinghe, 2013). In recent years, the development of seat suspension systems to mitigate vibrations transmitted to the human body has gained significant attention. Wickramasinghe (Wickramasinghe, 2013) tested aircrew members exposed to different levels of vibration in Bell-412 helicopters and evaluated the effects of WBV according to ISO 2631/1:1997 (ISO 2631/1:1997). His study revealed that under most flight conditions, the comfort and health were rated as “uncomfortable” and “unsafe”. Since the reduction of helicopter vibration to pilots remains a concern, this chapter uses lumped parameter models to simulate and analyze the effect of seat suspension stiffness and damping on transmissibility, which provides a theoretical basis for further design of semi-active seat suspension.

In this chapter, a single-DOF passive seat suspension system coupled with a 4-DOF human body biodynamic model is formulated according to ISO 2631/1:1997 (ISO 2631/1:1997). It is worth noting that the employed lumped parameter bio-dynamic model is adopted from the study published by Wan and Schimmels (Wan & Schimmels, 1995). They developed a 4-DOF lumped parameter model that captures the basic dynamics of a seated person exposed to vertical vibrations and coupled to a seat suspension according to the older version of the aforesaid standard (ISO 2631/1:1985; ISO 2631/3:1985). The schematic of the aforementioned 4-DOF biodynamic model and the corresponding governing equations of motion together with its vibration characteristics including seat-to-head transmissibility (STH), driving-point mechanical impedance (DPM), and apparent mass (AP) were presented in the Chapter 2. In this chapter, the “equivalent subjective sensitive response” weighting function based on ISO 2631/1:1985 in Wan’s study was used to validate the 5-DOF seat suspension system with the seated occupant model. ISO 2631/1:1985 and ISO 2631/3:1985 have been withdrawn with the new version ISO 2631/1:1997, a design optimization was subsequently formulated to optimally design the passive seat suspension system using frequency-dependent weighting function in new ISO 2631/1:1997. A comparison between optimal parameters of the passive seat suspension in the present study and those reported in Wan’s

research work (Wan, 1998), which is based on frequency-dependent weighting function based on ISO 2631/1:1985, is also presented in this chapter.

3.2 Vibration Evaluation of Human Exposure to WBV

The ISO 2631/1:1997 standard defines methods for determining the level of discomfort that human body perceives when exposed to the WBV. The following sections introduces and compares the variations between the requirements in both old version and new version of ISO 2631 standards, including vibration directions, frequency weightings, quantification methodologies, and assessment constraints. Despite the fact that ISO 2631/1:1997 has replaced ISO 2631/1:1985 and ISO 2631/3:1985, the old version gives a more precise boundary that illustrates the relationship between the limitation of comfort evaluation and the exposure length at various vibration frequencies. In brief, the main addition of the new version includes the comfort assessment of vibration on the seat surface, seat backrest, and cabin floor, as well as new quantification methods.

3.2.1 ISO 2631/1: 1985 and ISO 2631/3:1985

The ISO 2631/1:1985 and ISO 2631/3:1985 were prepared to provide a universally acceptable evaluation of human exposure to WBV. Due to the existence of complex factors to determine the human response to vibrations, the ISO 2631/1:1985 gave a fair compromise assessing procedure between the available laboratory data from the 1930s to 1970s. The ISO 2631/1:1985 applies primarily to the condition of when vibrations are transmitted from solid surface to human body in the frequency range of 1 Hz to 80 Hz. ISO 2631/3:1985 provides general guidelines for the evaluation of human exposure to WBV in the frequency range below 1 Hz (0.1-0.63 Hz), however, because of lack of data, the recommendations of ISO 2631/3:1985 can only apply to the z-axis vibration.

The location of vibration measurement given in these two parts of ISO 2631 for a seated human in a vertical direction should be at the surface where the vibration is transmitted to the body. As Figure 3.1 illustrates, the measurement transducer should be fastened such that the rigid seat surface to be the point of the occupant's buttock where touches the seat. The seated surface is made of solid material without any resilience. However, when a human is sitting on a cushion, the transmission shall be determined and considered when calculating the actual vibration transmitted to the body.

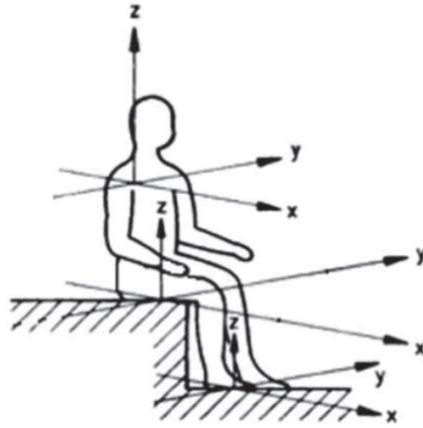


Figure 3.1: Measurement locations and directions of WBV for a seated human (ISO 2631/1:1997).

The intensity of vibration magnitude shall be acceleration (m/s^2). Although according to ISO 2631/1:1985 and ISO 2631/3:1985, the individual high crest factors caused by accidental shocks can reduce the accuracy of the vibration assessment to a certain extent, the root-mean-square (rms) method yet can be applied to all cases. There are three physical description criteria provided by ISO 2631/1:1985, namely, “fatigue-decreased proficiency boundary”, “exposure limit” and “reduced comfort boundary” within the frequency range of 1 Hz to 80 Hz. Each of these limits determines the preservation of working efficiency, health or safety, and comfort respectively. In ISO 2631/3:1985, the “motion sickness” associated with 0.1 Hz to 0.63 Hz in z-axis vibration transmission is also provided. By compiling these two standards, Wan and Schimmels proposed a weighting factor curve that covers the frequency range from 0.1 Hz to 80 Hz to facilitate the evaluation of vibration transmitted to a sitting human in the vertical direction as shown in Figure 3.2 over a relatively wider range (Wan & Schimmels, 1997). The weighting factor function shown in Figure 3.2 is basically obtained by inverting of “equivalent subjective sensitivity responses” to the vibration input curve. From 0.1 Hz to 0.63 Hz, the curve (dotted line) is identified as an inverting of ISO 2631/3:1985 presented for “severe discomfort boundaries” for vibration acceleration in the z-axis with an exposure time of 8 hours. Based on ISO 2631/3:1985, acceleration level at the center frequency of the one-third octave band is kept 0.25 m/s^2 from 0.1 Hz to 0.315 Hz and then increases linearly to 0.80 m/s^2 at the frequency of 0.63 Hz. The dotted line connects with the solid line as shown in Figure 3.2 from 0.63 Hz to 1 Hz was not experimentally obtained as mentioned in Wan and Schimmels’s study. The solid line from 1 Hz to

80 Hz shows the inverts of the “fatigue-decreased proficiency” boundary for vibration acceleration as a function of frequency based on 8 hours exposure based on ISO 2631/1:1985.

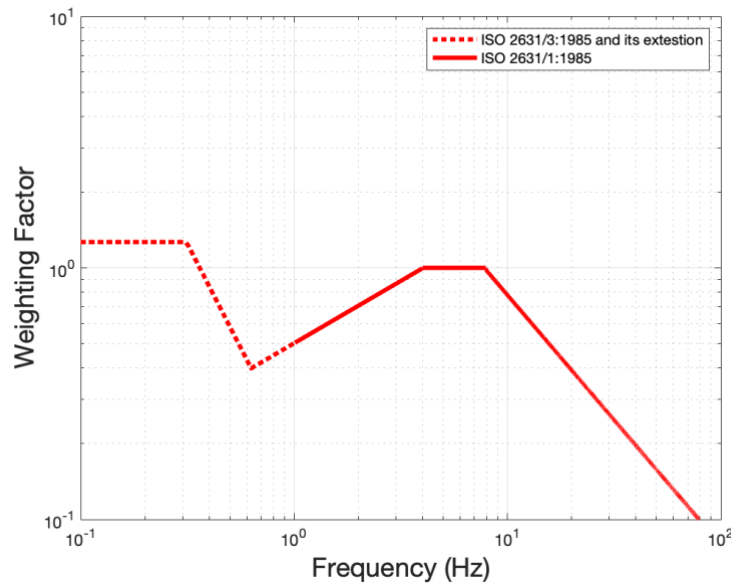


Figure 3.2: The variation of acceleration weighting factors with respect to input frequency based on ISO 2631/1:1985 and ISO 2631/3:1985 (Wan & Schimmels, 1997).

The computational procedure of assessing WBV in the z-axis direction based on ISO 2631/1:1985 and ISO 2631/3:1985 is schematically shown in Figure 3.3. When the vibration acceleration in the z-axis direction is measured at the point of the seat surface, acceleration magnitude at each 1/3 octave band frequency should be subsequently evaluated. At each center frequency 1/3 octave, the weighted rms acceleration magnitude should be integrated. By calculating the rms value, the average acceleration input to the human is used to assess the vibration exposure.

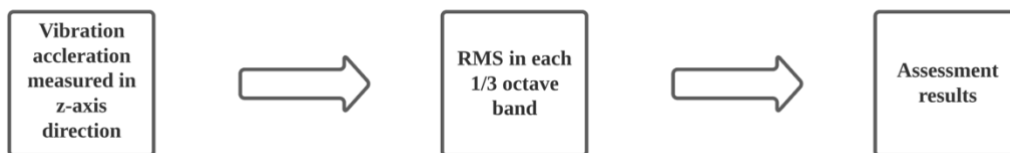


Figure 3.3: General procedure for assessing human exposure to vertical WBV in ISO 2631/1:1985 and ISO 2631/3:1985.

3.2.2 Standard ISO 2631/1: 1997

In this section the new version ISO 2631/1:1997, which establish guidelines for assessing WBV in terms of human health and comfort, probability of vibration perception, the incidence of motion sickness, is discussed. Because the present research only focuses on the vertical vibration of the seated human body, the following content only discusses the relevant assessment criteria from ISO 2631/1:1997.

The ISO 2631/1:1985 and ISO 2631/3:1985 are replaced by ISO 2631/1:1997 which provides a detailed and complete definition of the frequency weighting in each direction. The frequency range in this revision is from 0.1 Hz to 100 Hz. The frequency range below 1Hz, and the corresponding evaluation is extended in this revision. It is worth to mention that the rms method is still the basis for the measurement when the crest factor is lower than 9. Noted that the crest factor is defined as the modulus of the ratios of the maximum instantaneous peak value of the frequency-weighted acceleration signal to its rms value (ISO 2631/1:1997). Based on practical experience and related studies, a higher crest factor is considered to be a critical factor on the evaluation of vibration exposure. In this version of ISO 2631:1997, auxiliary evaluation criteria such as Maximum transient vibration value (MTVV) and the fourth power vibration dose method (VDV) are given when the crest factors are higher than 9. The concept of “fatigue-decreased-proficiency” due to vibration exposure as well as vibration exposure limits have been removed from ISO 2631/1:199. Three vibration evaluation methods provided in ISO 2631/1:1997 are briefly described in the following.

a) Weighted rms Acceleration Method.

The weighted rms acceleration method as a basic evaluation approach shall always be included in vibration evaluation. The rms formulation is (ISO 2631/1:1997):

$$a_w = \left[\frac{1}{T} \int_0^T a_w^2(t) dt \right]^{\frac{1}{2}} \quad (3-1)$$

The a_w is the weighted rms acceleration which is expressed in meters per second squared (m/s^2). This approach suggests multiplying each measured acceleration with its appropriate frequency weighted factors or functions. $a_w(t)$ is the weighted equivalent acceleration at each moment. T is the duration of measurement in seconds. The weighted rms method objectively reveals the vibration condition of the human body. Although a limit is not included in ISO 2631/1:1997, a

table of approximate indications of likely reactions to various magnitudes of overall vibration is provided in Table 3.1.

Table 3.1: Approximate indications of likely reactions to various magnitudes of weighted rms acceleration (ISO 2631/1:1997).

Overall Total Value	Indications
Less than 0.315 m · s⁻²	Not uncomfortable
0.315 – 0.63 m · s⁻²	A little uncomfortable
0.5 – 1.0 m · s⁻²	Fairly uncomfortable
0.8 – 1.6 m · s⁻²	Uncomfortable
1.25 – 2.5 m · s⁻²	Very uncomfortable
Greater than 2.0 m · s⁻²	Extremely uncomfortable

b) Maximum Transient Vibration Value (MTVV).

The running rms method is defined as (ISO 2631/1:1997):

$$a_w(t_0) = \left\{ \frac{1}{\tau} \int_{t_0-\tau}^{t_0} [a_w(t)]^2 dt \right\}^{1/2} \quad (3-2)$$

where $a_w(t)$ is the instantaneous frequency-weighted acceleration; τ is the integration time for running averaging; t_0 is the time of observation (instantaneous time). The running rms evaluation method takes into account occasional shocks and transient vibration by use of a short integration time constant. The maximum transient vibration value (MTVV) is subsequently defined as the highest magnitude of the running rms method during the measurement period as (ISO 2631/1:1997):

$$\text{MTVV} = \max [a_w(t_0)] \quad (3-3)$$

The use of MTVV measurement for evaluation represents more prominent occurrences of shock and intermittent vibration.

c) The Fourth Power Vibration Dose Method.

In this method the fourth power of the acceleration time history is used for averaging instead of the second power. Thus, the fourth power vibration dosage approach is more sensitive to the peaks than the basic weighted acceleration method. The fourth power vibration dosage value (VDV) is defined as follow in meters per second to the power 1.75 ($\text{m/s}^{1.75}$), or in radians per second to the power 1.75 ($\text{rad/s}^{1.75}$) (ISO 2631/1:1997):

$$\text{VDV} = \left\{ \int_0^T [a_w(t)]^4 dt \right\}^{\frac{1}{4}} \quad (3-4)$$

where, $a_w(t)$ is the instantaneous frequency-weighted acceleration; T is the duration of the measurement. In a sense, it amplifies the value of the weighted equivalent acceleration $a_w(t)$ to make it more sensitive to the peak value of vibration.

3.2.2.1 Frequency weighting curve in vertical direction

A frequency weighting curve in z-direction for a seated human according to ISO 2631/1:1997 is shown in Figure 3.4. This frequency weighting function is expressed as the multiplication of four transfer functions as (ISO 2631/1:1997):

$$\text{The High-pass filter: } H_h(s) = \frac{s^2}{s^2 + \frac{\omega_1}{Q_1}s + \omega_1^2} \quad (3-5)$$

$$\text{The Low-pass filter: } H_l(s) = \frac{\omega_2^2}{s^2 + \frac{\omega_2}{Q_2}s + \omega_2^2} \quad (3-6)$$

$$\text{Acceleration-velocity transition filter: } H_t(s) = \frac{\frac{\omega_4^2}{\omega_3}s + \omega_4^2}{s^2 + \frac{\omega_4}{Q_4}s + \omega_4^2} \quad (3-7)$$

$$\text{Upward step filter: } H_s(s) = \frac{s^2 + \frac{\omega_5}{Q_5}s + \omega_5^2}{s^2 + \frac{\omega_6}{Q_6}s + \omega_6^2} \quad (3-8)$$

The weighting filter is thus represented as:

$$W_k = H_h(s) \cdot H_l(s) \cdot H_t(s) \cdot H_s(s) \quad (3-9)$$

The parameters of the frequency weighting functions are provided in Table 3.2.

Table 3.2: Parameters of the transfer function of the frequency weightings.

W_k	H_h		H_l			H_t			H_s		
	$f_1(\text{Hz})$	Q_1	$f_2(\text{Hz})$	Q_2	$f_3(\text{Hz})$	$f_4(\text{Hz})$	Q_4	$f_5(\text{Hz})$	Q_5	$f_6(\text{Hz})$	Q_6
	0.4	$1/\sqrt{2}$	100	$1/\sqrt{2}$	12.5	12.5	0.63	2.37	0.91	3.3	0.91

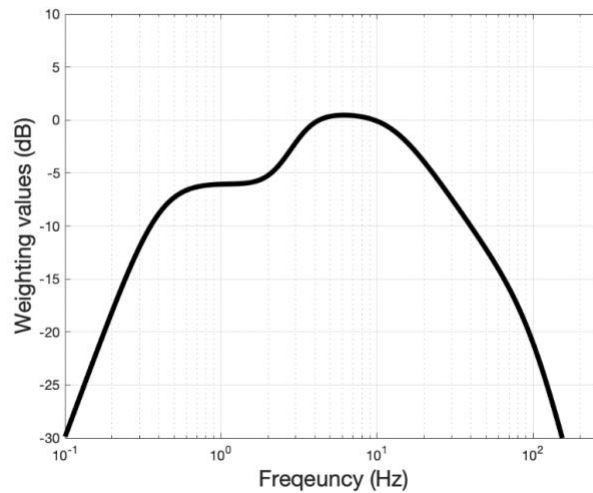


Figure 3.4: ' W_k ' Frequency variation of acceleration weighting functions based on ISO 2631/1:1997.

The computational procedure of assessing WBV in the z-axis direction according to ISO 2631/1:1997 is schematically shown in Figure 3.5.

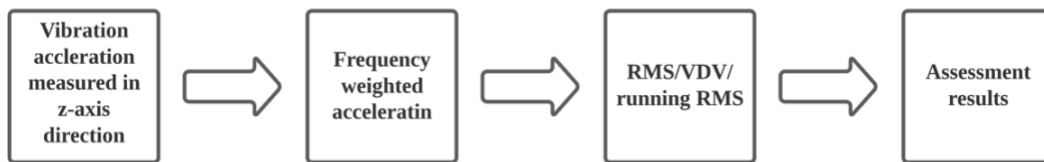


Figure 3.5: General Procedure for Assessing Human Exposure to WBV in ISO 2631/1:1997.

When the vibration acceleration in the vertical direction is measured, frequency weighted acceleration should be obtained by multiplying the acceleration at each center frequency of 1/3 octave band with the associated weighting factor given in Figure 3.4. The frequency weighted acceleration then can be effectively used in quantification methods such as the rms method, MTVV, or VDV. It is noted that frequency weighting factor should also be multiplied by a direction-related factor k , as defined in Table 3.3 to assess the effect of WBV on comfort. For seated surface in z direction which is the subject of this study, this factor is unity. Comfort reaction to vibration environment based on frequency weight rms acceleration is given in Table 3.1. The Overall total value of frequency weight rms acceleration represents the summation of all the surfaces and directions.

Table 3.3: Frequency weighting and multiplying factors in ISO 2631/1:1997.

Location	Direction	Frequency	Multiplying
Seat surface	x	W_d	1
	y	W_d	1
	z	W_k	1
Seat backrest	x	W_c	0.8
	y	W_d	0.5
	z	W_d	0.4
Feet	x	W_k	0.25
	y	W_k	0.25
	z	W_k	0.4

3.3 5-DOF Coupled Human Body/Seat Suspension Model

To study the effect of the stiffness and damping characteristics of the seat suspension on the transmitted WBV, 4-DOF lumped vibration model of human is coupled with 1-DOF seat suspension to derive the coupled 5-DOF system. The coupled model is then effectively used to identify the optimal stiffness and damping parameters of the passive system to minimize the frequency average (rms) weighted acceleration input to the human based on the standard ISO 2631/1:1997. The acceleration transmissibility from the cab-floor to the head is then obtained for different optimal configuration of the seat suspension parameters. The optimized seat suspension results provide a reference/guideline for designing the semi-active suspension featuring MRE in the subsequent chapters.

3.3.1 Transmissibility Analysis

The 4-DOF human body model previously investigated by Wan (Wan & Schimmels, 1995) is adopted in this thesis for simulation and design optimization of passive seat suspension as illustrated in Figure 3.6. The parameters of human body model are given in Table 2.1 which is also again represented here in Table 3.4. The m_s , k_s and c_s are the mass, stiffness and damping of the seat suspension and x_0 is the input excitation to the system.

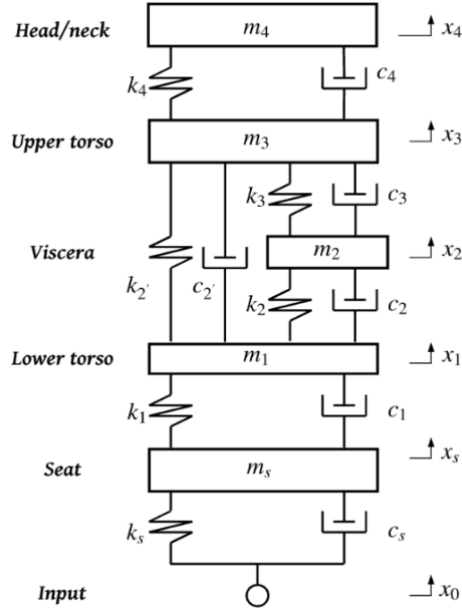


Figure 3.6: Lumped parameter model of seat suspension system with occupant (Wan, 1998).

Table 3.4: Parameter values of 4-DOF human body model (Wan & Schimmels, 1995).

\mathbf{m}_4 (kg)	4.17	\mathbf{k}_4 (N · m ⁻¹)	134400	\mathbf{c}_4 (N · s · m ⁻¹)	250
\mathbf{m}_3 (kg)	15	\mathbf{k}_3 (N · m ⁻¹)	10000	\mathbf{c}_3 (N · s · m ⁻¹)	200
—	—	$\mathbf{k}_{2'}$ (N · m ⁻¹)	192000	$\mathbf{c}_{2'}$ (N · s · m ⁻¹)	909.09
\mathbf{m}_2 (kg)	5.5	\mathbf{k}_2 (N · m ⁻¹)	20000	\mathbf{c}_2 (N · s · m ⁻¹)	330
\mathbf{m}_1 (kg)	36	\mathbf{k}_1 (N · m ⁻¹)	49341.6	\mathbf{c}_1 (N · s · m ⁻¹)	2475

The governing dynamic equations for the 5-DOF coupled human/seat model are derived using second's law of Newton as:

$$m_4 \ddot{x}_4 = k_4(x_3 - x_4) + c_4(\dot{x}_3 - \dot{x}_4) \quad (3-10)$$

$$m_3 \ddot{x}_3 = k_{2'}(x_1 - x_3) + c_{2'}(\dot{x}_1 - \dot{x}_3) + k_3(x_2 - x_3) + c_3(\dot{x}_2 - \dot{x}_3) - k_4(x_3 - x_4) - c_4(\dot{x}_3 - \dot{x}_4) \quad (3-11)$$

$$m_2 \ddot{x}_2 = k_2(x_1 - x_2) + c_2(\dot{x}_1 - \dot{x}_2) - k_3(x_2 - x_3) - c_3(\dot{x}_2 - \dot{x}_3) \quad (3-12)$$

$$m_1 \ddot{x}_1 = k_1(x_s - x_1) + c_1(\dot{x}_s - \dot{x}_1) - k_{2'}(x_1 - x_3) - c_{2'}(\dot{x}_1 - \dot{x}_3) - k_2(x_1 - x_2) - c_2(\dot{x}_1 - \dot{x}_2) \quad (3-13)$$

$$m_s \ddot{x}_s = k_s(x_0 - x_s) + c_s(\dot{x}_0 - \dot{x}_s) - k_1(x_s - x_1) - c_1(\dot{x}_s - \dot{x}_1) \quad (3-14)$$

Similar to procedure for lumped model of human body in section 2.2, the above equation can be

formulated in matrix in frequency domain using Fourier transform as:

$$-\omega^2[M]\{x(j\omega)\} + j\omega[C]\{x(j\omega)\} + [K]\{x(j\omega)\} = [B]\{Q(\omega)\} \quad (3-15)$$

which again

$$Q(\omega) = \begin{bmatrix} 1 \\ (j\omega) \end{bmatrix} \{x_0(\omega)\} \quad (3-16)$$

and displacement vector of lumped masses:

$$\{x(j\omega)\} = [x_4(j\omega), x_3(j\omega), x_2(j\omega), x_1(j\omega), x_s(j\omega)] \quad (3-17)$$

Let us assume:

$$[A] = -\omega^2[M] + j\omega[C] + [K] \quad (3-18)$$

Thus, one can write:

$$[A]\{x(j\omega)\} = [B]\{Q(\omega)\} \quad (3-19)$$

and solving for $x(j\omega)$ yields:

$$\{x(j\omega)\} = [A]^{-1}[B]\{Q(\omega)\} \quad (3-20)$$

$$\{x(j\omega)\} = [A]^{-1}[B] \begin{bmatrix} 1 \\ (j\omega) \end{bmatrix} \{x_0(\omega)\} \quad (3-21)$$

therefore, the general transfer function of coupled human body/seat response is

$$H(\omega) = [H_4(\omega), H_3(\omega), H_2(\omega), H_1(\omega), H_s(\omega),]^T = [A]^{-1}[B] \begin{bmatrix} 1 \\ (j\omega) \end{bmatrix} \quad (3-22)$$

The cab floor-to-head acceleration transmissibility can subsequently be described as:

$$S(\omega) = \frac{\{x_4(j\omega)\}}{x_0(j\omega)} = H_4(\omega) \quad (3-23)$$

3.3.2 Design Optimization of Seat Suspension System

Wan (Wan, 1998) formulated a design optimization procedure for the seat suspension systems in which rms acceleration of the seat suspension output based on a specific exposure time was considered as the objective function to be minimized. This exposure time must be smaller than the acceleration limit provided by the ISO 2631 standard. In this study, a relatively similar design optimization procedure has been used for optimal design of passive seat suspension system. Unlike Wan's approach, the frequency weighting function according to new version of ISO 2631 (ISO 2631/1:1997) has been used to find the frequency weighted accelerated input. The optimal suspension parameters obtained based on old and new version ISO 2631 are then compared. A white-noise signal (random signal with constant power spectral density) with zero mean is

considered as the vibration input to the suspension system from the cab floor. The objective of the optimization is to minimize the vertical WBV transmitted to the operator. More precisely, the aim is to minimize the frequency weighted average acceleration (rms) input (acceleration out from seat mass) to human operator which can be mathematically described as:

$$\text{Objective function} = \sqrt{\int_{\omega_1}^{\omega_f} |H_s(\omega)|^2 S_{\ddot{x}_0} w_f^2 d\omega} \quad (3-24)$$

where $\omega_f = 2\pi f_u$ and $\omega_1 = 2\pi f_l$ are the upper and lower bound of the considered frequency range in rad/s, $H_s(\omega)$ is the transmissibility function from cab-floor to seat, $S_{\ddot{x}_0}$ is the power spectral density of the input (cab floor) to the seat suspension which is assumed as an constant 0.2. w_f is the frequency-dependent weighting function according to ISO 2631/1:1997 standard. Figure 3.7 shows the weighting factor in 1/3 octave band at each center according to ISO 2631/1:1997 standard. Integration in the objective function can subsequently be turned into summation over each 1/3 octave band as:

$$F = \sqrt{\sum_{i=1}^n |H_s(i)|^2 \cdot \text{band width}^i \cdot S_{\ddot{x}_s} w_f(i)^2} \quad (3-25)$$

$$\text{band width}^i = f_u^i - f_l^i \quad (3-26)$$

$$f_u^i = f_c(i) \cdot 2^{\frac{1}{6}} \quad (3-27)$$

$$f_l^i = f_c(i) / 2^{\frac{1}{6}} \quad (3-28)$$

band widthⁱ is the total width of band of at the ith center of frequency $f_c(i)$. $H_s(i)$ and $w(i)$ demonstrate the magnitude of transmissibility from cab-floor to seat and the weighting factor values at the ith center of frequency, respectively.

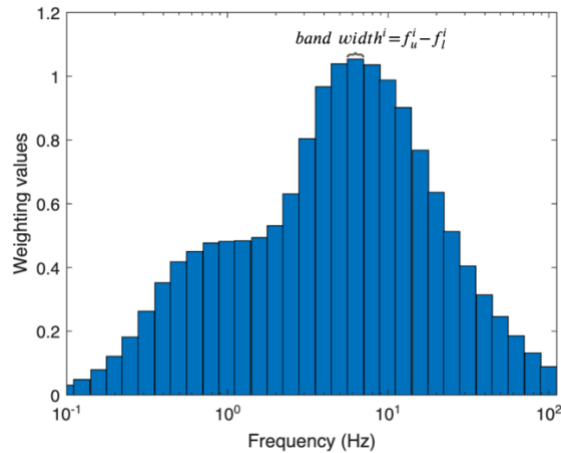


Figure 3.7: Description of band width calculation method based on ISO 2631/1:1997.

The design optimization problem can be formally formulated as: Find seat stiffness parameters, mass (m_s), damping coefficient (c_s) and stiffness (k_s),
to minimize: F
subject to side constraints:

$$3 \leq m_s \leq 30\text{kg} \quad (3-29)$$

$$10 \leq c_s \leq 10000 \text{ Ns/m} \quad (3-30)$$

$$k_{s1} \leq k_s \leq 500000 \text{ N/m} \quad (3-31)$$

Similar to Wan (Wan, 1998), different cases representing different lower bound of stiffness, ($k_{s1} = 2500, 5000, 10000, 20000 \text{ N/m}$) of the seat suspension has been investigated. The optimal mass of the seat suspension, m_s is found to be different at each optimization run. It sometimes converges to its lower bound, sometimes to its upper bound and sometimes to value between lower and upper bound. This has also been reported by Wan (Wan, 1998). Thus, in this study the value of seat mass has been initially set at 30 kg. Both standards ISO 2631/1:1985 & ISO 2631/3:1985 and ISO 2631/1:1997 are used to evaluate the frequency dependent weighting factor in the objective function. The above optimization problem is a nonlinear constraint optimization problem and thus the powerful sequential quadratic programming (SQP) technique implemented in MATLAB environment has been used to accurately identify the local optimum solution due to the non-convex nature of the problem. To assure capture of global optimum solution, the optimization problem has been solved using several random initial points in the design space and subsequently the minimum of the identified local minimums at each run has been chosen as the global optimum solution. The optimal results for different lower bound of stiffness are provided in Table 3.5 for both standards.

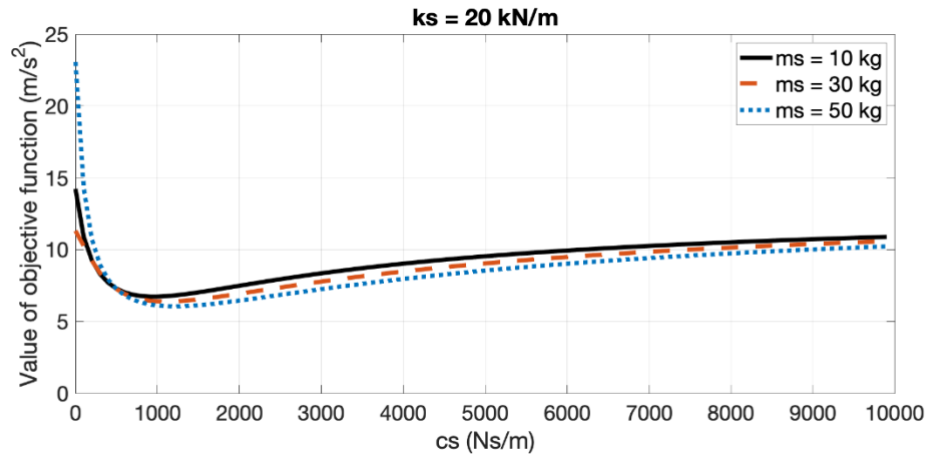
Results show that optimal stiffness converges to its lower bound irrespective of the old or new version of ISO 2631 standards used. Using stiffness different lower results different optimal value for the seat damping coefficient. While both old and new version of ISO 2631 standards yield increase in optimal damping coefficient by increasing the lower bound of stiffness, the optimal coefficient obtained using ISO 2631/1:1997 standard is lower than those based on standard ISO 2631/1:1985 & ISO 2631/3:1985. For instance optimum damping for the case 1 (stiffness lower bound set at 2.5 kN/m) is found to be 334.83 and 326.18 Ns/m based on ISO 2631/1:1985 & ISO 2631/3:1985 and ISO 2631/1:1997 standards, respectively. They increase, respectively, to 1081.62 N · s/m and 774.68 N · s/m for the case 4 (stiffness lower bound set at 20 kN/m). As it can be realized, the optimal damping coefficients based on ISO 2631/1:1997 standard for cases 1

and 4 is almost 2.6% and 28.4% lower than those based on ISO 2631/1:1985 & ISO 2631/3:1985, respectively. The value of objective function at optimum design-based on new version of ISO 2631 standard is also smaller than that based on older version under the same conditions.

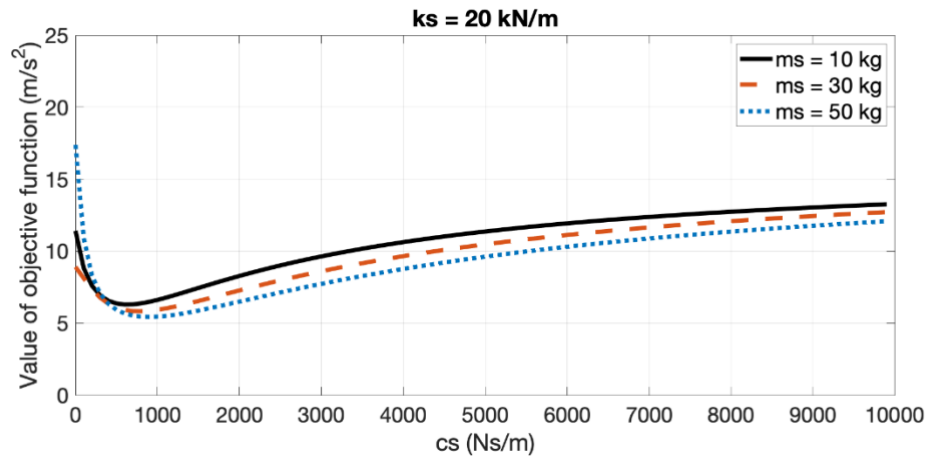
Table 3.5: Optimal values of the seat parameters obtained using ISO 2631 standards.

	ISO 2631/1:1985 & ISO 2631/3:1985						
	Damping c_s (Ns/m)		Stiffness k_s (kN/m)				Objective function value (m/s^2)
	Optimized value	Damping ratio (ζ_s)	Lower bound	Upper bound	Optimized value	Natural frequency	
Case 1	334.83	0.61	2.50	500.00	2.50	1.45	3.00
Case 2	483.78	0.62	5.00	500.00	5.00	2.05	3.80
Case 3	722.57	0.66	10.00	500.00	10.00	2.91	4.96
Case 4	1081.62	0.70	20.00	500.00	20.00	4.11	6.38
	ISO 2631/1:1997						
	Damping c_s (Ns/m)		Stiffness k_s (kN/m)				Objective function value (m/s^2)
	Optimized value	Damping ratio (ζ_s)	Lower bound	Upper bound	Optimized value	Natural frequency	
Case 1	326.18	0.60	2.50	500.00	2.50	1.45	2.79
Case 2	433.13	0.56	5.00	500.00	5.00	2.05	3.54
Case 3	560.67	0.51	10.00	500.00	10.00	2.90	4.47
Case 4	774.68	0.50	20.00	500.00	20.00	4.11	5.82

Figure 3.8 shows the variation of the objective function with respect to seat damping coefficient, c_s varying from its lower bound of 10 Ns/m to its upper bound of 10000 Ns/m for the optimal seat stiffness set at 20 kN/m (case 4) and different seat masses of 10 kg, 30 kg and 50 kg using both ISO 2631/1:1985 & ISO 2631/3:1985 and ISO 2631/1:1997 standards. Figure 3.8 clearly shows the optimum damping at which the objective function becomes minimum verifying the results in Table 3.5. Examination of Figure 3.5 reveals that optimum damping coefficients are almost insensitive to seat masses and very slightly increases by increasing the seat mass. It is also clear that decreasing and increasing damping below and above the optimal damping value, respectively increases the WBV (objective function value). Moreover, by increasing the damping coefficient beyond the optimal value, WBV slightly decreases by increasing the seat mass, while by decreasing the damping coefficient from its optimum value, the objective function shows the smaller value for the seat mass of 30 kg. Similar behavior has also been observed for other cases.



(a)

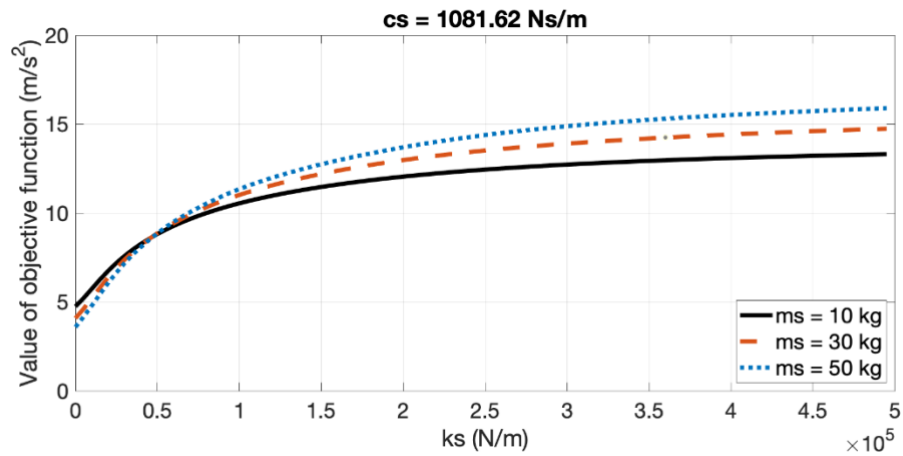


(b)

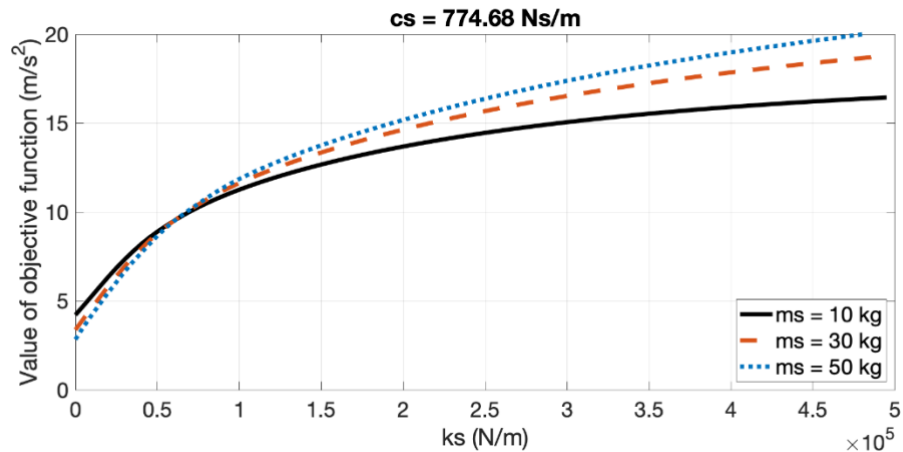
Figure 3.8: c_s versus objective value with varies m_s : (a) ISO 2631/1:1985 and ISO 2631/3:1985; (b) ISO 2631/1:1997

Figure 3.9 also shows the variation of objective function with respect to the stiffness varying from its lower bound set at 20000 N/m to its upper bound of 500000 N/m (case 4) for different masses (10-50 kg) while the damping values have been set at their optimum values of 1081.62 N · s/m and 774.68 N · s/m based on standards ISO 2631/1:1985 & ISO 2631/3:1985 and ISO 2631/1:1997, respectively. Results clearly show that minimum value of objective occurs at lower bound of stiffness (20000 N/m) irrespective of the seat masses confirming results in Table 3.5. Examination of results also reveal that increasing the seat stiffness beyond its optimum value increases the objective function substantially at first and then gradually flattening. Results for

different seat masses intersect at seat stiffness values of around 45 kN/m and 55 kN/m according to standard ISO 2631/1:1985 & ISO 2631/3:1985 and ISO 2631/1:1997, respectively. The value of objective function decreases with increasing the seat mass (m_s), when seat stiffness, k_s is smaller than the 50 kN/m. However, at higher than 50 kN/m, the value of the objective function increases with increasing the m_s .



(a)

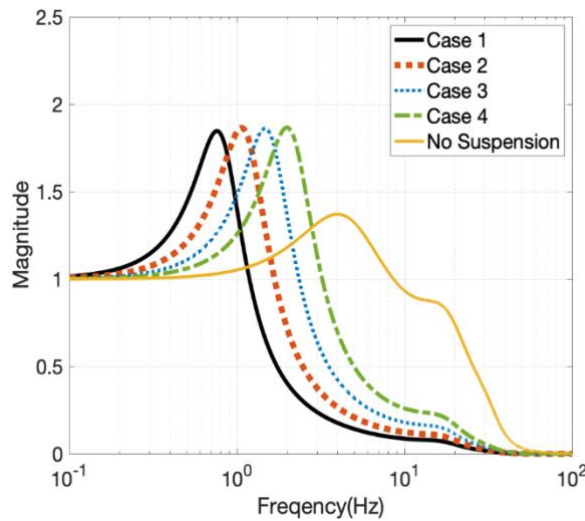


(b)

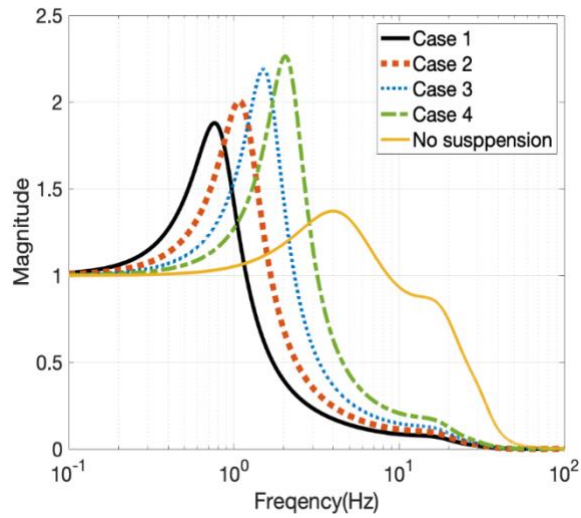
Figure 3.9: k_s versus objective value with varies m_s : (a) ISO 2631/1:1985 and ISO 2631/3:1985; (b) ISO 2631/1:1997.

Figure 3.10 shows the acceleration vibration transmissibility from the cabin floor to the operator head using the optimization results obtained based on both old and new versions of ISO 2631 standard. As it can be realized, natural frequency shifts from nearly 0.8 Hz in case 1 to almost

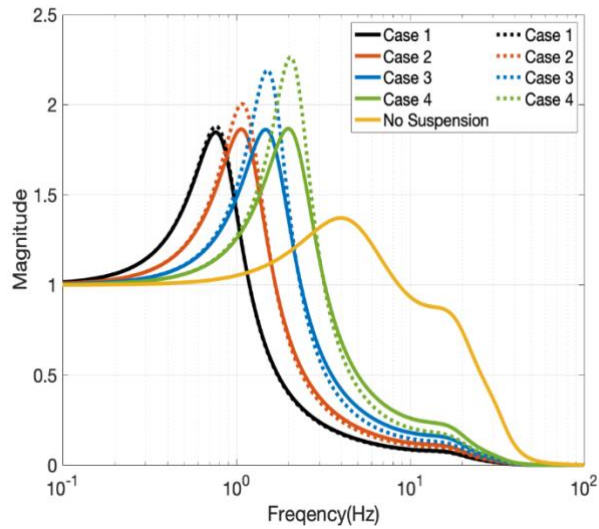
2 Hz in Case 4 irrespective of the standards used. The magnitude of the transmissibility, however increases substantially from case 1 to case 4 based on standard ISO 2631/1:1997 compared with that based on standard ISO 2631/1:1985 and ISO 2631/3:1985. This is in part due to the lower optimum damping obtained based on new ISO 2631 standard. This can be seen in Table 3.5 in which damping ratio decreases from case 1 to case 4. The peak magnitude in transmissibility directly related to the inverse of the damping ratio. Thus, reduction in damping ratio results in an increase in the transmissibility peak amplitude. Results also show that optimal passive suspension systems (case 1, seat stiffness-2500 N/m) greatly reduce vibration transmissibility to the operator head for the frequency range 1-80 Hz compared with no suspension (corresponding to rigid seat in which $k_s \rightarrow \infty$). It is noted that the suspension system design for case 1 (lowest seat stiffness of 2500 N/m) yields total static deflection of nearly 35 cm (14 in) considering both mass of human and seat (nearly 91 kg) which is practically realizable. For other cases the stroke is less than 35 cm. It is interesting to note that in the frequency range of 4-10 Hz, where the human body is most sensitive according to the no suspension case, the ISO 2631/1:1997 optimized results provide a lower transmissibility as can be observed from Figure 3.10 (c). Further examination of results in Figure 3.10 shows that for frequency above 1 Hz seat suspension with lowest stiffness is preferable while for the very low frequency range below 1 Hz, the seat suspension with highest possible stiffness provide better vibration isolation. Thus development of an adaptive seat suspension system whose stiffness can be autonomously varied, provides a unique opportunity to attenuate WBV in wide range of frequencies.



(a)



(b)



(c)

Figure 3.10: Transmissibility from cab-floor to operator head for optimal seat suspension design and no seat suspension: (a) ISO 2631/1:1985 and ISO 2631/3:1985; (b) ISO 2631/1:1997 (c) Comparison of two ISO standards. The solid lines and dotted lines represent the ISO 2631:1997 and ISO 2631: 1985, respectively.

3.4 Conclusion

A 5-DOF coupled human/seat suspension system has been formulated to investigate transmitted WBV in a seated human under vertical vibration. A design optimization strategy has also formulated to identify the optimal parameter of the passive seat suspension. The effect of different

optimization cases on WBV is investigated. Result show that optimization results always converge to lower bound of stiffness value and the damping coefficient increases as the stiffness lower bound increases. Moreover, the optimal damping using standard ISO 2631/1:1997 is lower than those based on ISO 2631/1:1985 and ISO 2631/3:1985. The optimal damping ratio, however, decreases as the lower bound stiffness increases using ISO 2631/1:1997 resulting in an increase in the transmissibility peak. Transmissibility results from the seat to head with no suspension in frequency range 0.6-80 Hz shows a first resonance peak between 4-8 Hz which is mainly generated by the chest resonance and a smaller second resonance around 10 Hz generated by the abdominal resonance. When resonating, these have great impact on the brain and the head and facial organs. Passive suspensions designed based on the weighting functions provided by ISO 2631/1:1985, ISO 2631/3:1985 and ISO 2631/1:1997 can significantly reduce the vibration transmissibility in the most sensitive range of the human body, while seat suspension designed based on ISO 2631/1:1997 slightly outperforms. Therefore, ISO 2631/1:1997 would be adopted in the subsequent semi-active seat suspension design.

Chapter 4: Development of an Adaptive MRE-Based Vibration Isolator

4.1 Introduction

Suppression of vibration-induced injuries to human operators in transportation has been a challenging task owing to varied aspects related to seated occupant compliance, anthropometry, and vibration conditions (Burström et al., 2015; Nishiyama et al., 2012). Various semi-active and active seat suspension systems featuring magneto-rheological (MR) fluids with variable damping properties have been proposed to alleviate the harmful effects of the transmitted vibration to the seated occupants (Gağorowski, 2012). However, limited studies have focused on the development of semi-active seat suspension based on MR elastomers (MREs) which are capable of changing their damping and stiffness properties simultaneously. These have been mainly limited to horizontal vibration isolation of seats using negative stiffness properties of MREs (Sun et al., 2015). Nevertheless, vertical vibration isolation of seat using MRE-based vibration isolators has been rarely investigated (W. Li et al., 2012). This is attributable to the fact that the stiffness of seat suspensions is required to be designed as soft as possible to have a lower natural frequency (ω_n) than excitation frequencies of interest, thereby providing effective vibration isolation above $\sqrt{2}\omega_n$ (Y. T. Choi & Wereley, 2022). At the same time, a large stiffness is required to avoid excessive deflection due to seated occupant weight. For instance, Liu et al. (Liu et al., 2020) developed an MRE-based semi-active seat suspension to provide vertical vibration isolation for seat applications. To avoid softening effect of MRE materials at large deformation, a low stroke limit of 5 mm was considered in their design, which may limit their practical application for seat suspensions. To address the above-mentioned trade-off, in the present study a novel semi-active seat suspension system employing an MRE-isolator unit together with parallel and series passive springs has been proposed. The parameters of the presented MRE isolator and the passive springs were obtained via a design optimization formulation. The proposed semi-active suspension system based on MREs can 1- allow large vertical deformation of the seat while maintaining MRE to operate within limited deformation regime at the same time; 2- providing sufficient frequency shift/vibration isolation.

4.2 Characterization of MREs

Designing smart devices based on MRE materials requires a robust material model capable of capturing the MRE dynamic behavior under both the magnetic field and mechanical deformation. The model can then be subsequently used for modeling and design optimization of MRE-based devices. To develop such material model, it is indeed necessary to firstly experimentally characterize MRE dynamic behavior under relatively wide ranges of magnetic and mechanical loadings. The characterization can be implemented in shear and tension/compression loading configurations. Since the shear mode operation of MREs requires much simpler configuration in terms of both design of device and characterization procedure, the present thesis, thus, mainly concerned with shear mode experimental characterization of MREs.

4.2.1 Fabrication of MRE samples

To implement characterization of MREs in shear mode, an isotropic MRE batch was fabricated in the laboratory. Succinctly, magnetically soft iron particles (SQ, BASF, Germany) were initially mixed with liquid silicone rubber (Eco-flux 00-20, USA). It should be noted that the volume concentration of the MRE sample was selected as 25% to maximize the MR effect (Liu et al., 2020). After thoroughly mixing the CIPs with silicone rubber, the mixture was degassed using a vacuum chamber in order to remove any potential air bobbles within the mixture. Then, the mixture was poured into a cylindrical mold with a diameter and thickness of 80 mm, and 1 mm, respectively. The MRE was then allowed to be cured at laboratory temperature (20°C) for 24 hrs. Since during curing the sample, no magnetic field was supplied, the fabricated MRE has an isotropic microstructure in which the magnetizable particles are randomly distributed within the rubber-like matrix. Subsequently, cylindrical MRE samples with a diameter of 20 mm were cut from the fabricated batch, which is suitable for characterization with commercially available magneto-rheometer.

4.2.2 Shear mode characterization

Simply, the characterization process allows to understand the dynamic behavior of MRE materials under external magnetic and mechanical loading. As mentioned before, even though MREs can be operated in shear as well as tension/compression mode, in this project our focus is dedicated towards the characterization of MRE in shear mode as it demands simpler characterization procedure and subsequent design of MRE isolator. For this purpose, an advanced magneto-

rheometer device model Discovery HR-3 from TA instrument equipped with an electromagnet cell was used for characterization purpose, as shown in Figure 4.1 (a). A schematic diagram of the rotational parallel plate configuration with magnetorheological (MR) unit attachment is shown in Fig.4.1 (b). To prevent slippage during the test, the MRE sample was clamped between the upper and lower geometry with an axial preload of around 10 N. The MR unit produces a consistent and uniform magnetic flux density up to 1 Tesla along the axis of the cylindrical MRE sample, which is essentially perpendicular to the direction of shear motion. The magnetic flux density and other information is measured by a Hall probe sensor, which is located directly below the MRE sample.

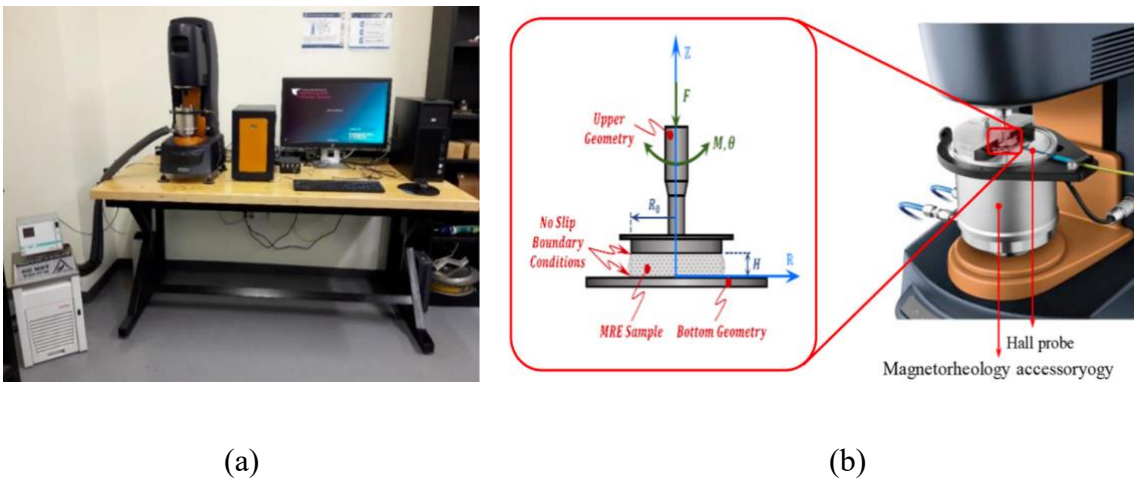


Figure 4.1: MREs testing system (a) The MREs testing system; (b) schematic diagram of the rotational parallel-plate setup of the rotary rheometer equipped with magneto-rheology accessory.

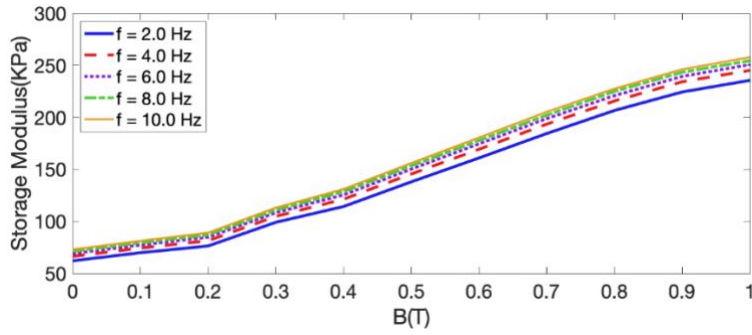
Series of experiments were conducted under varied mechanical and magnetic loadings. The input mechanical loading was sinusoidal with frequency varied from 0.2 Hz to 10 Hz. As mentioned before, prior application of sinusoidal oscillation, a pre-load of 10 N was applied to not only avoid slipping of the MRE samples at higher frequency but also to represent a real and practical situation which MREs experience in applications. The magnetic field was realized by the embedded electromagnetic unit within the magnetorheological cell. The value of magnetic flux density for characterization was varied from 0 T to 1.0 T. It should be noted that the TA instrument equipped with a temperature unit control that keep maintaining the temperature of the sample near 20°C during characterization tests.

4.2.3 Experimental data

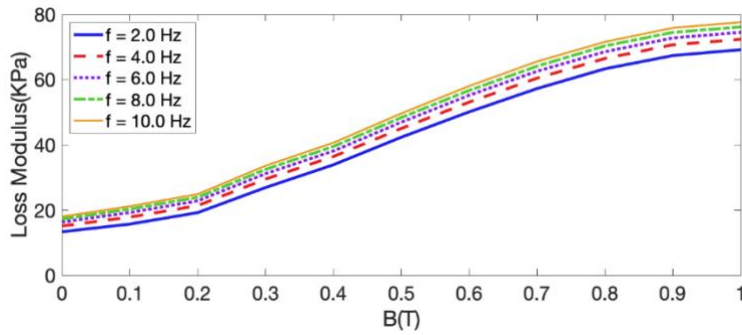
In this section, the identified shear mode characteristics of the MRE sample were described. Typically, these include evaluation of MRE sample with respect to their capacity for storing and dampening the input excitation energy. The former and latter respectively can be described by storage (G') and loss (G'') moduli. The available software for the TA instrument directly provides the measured values of G' and G'' from torque and angular displacement measurements in time domain. Figure 4.2 and Figure 4.3 show variations of the shear storage and loss moduli with respect to magnetic flux density. It should be emphasized that these data are obtained under frequency 0.2 Hz to 10 Hz and strain amplitude of 15% and 30%, respectively. Figure 4.2 (a) and 4.2 (b) illustrate the variation of measured storage and loss moduli with respect to magnetic flux density. The presented experimental data are related to strain amplitude of 15%. The experimental results reveal that both storage and loss moduli increase with the increase of magnetic flux density. This is mainly due to dipole-dipole interaction of magnetic particles within magnetic field, thereby squeezing the rubber-like matrix among them, which leads to stiffening effect of MREs. From the magnetic flux density of 0.2 T to 0.8 T, the slope of increasement show a higher increment in both storage and loss moduli. Results also were indicative of magnetic saturation of both storage and loss moduli, when magnetic field exceeds 0.9 T.

Figure 4.3 shows the variation of both storage and loss moduli with respect to magnetic field for the strain amplitude of 30%. Similar tendencies were also obtained here, when comparing to Figure 4.2. Both of storage and loss moduli increase steadily with magnetic flux density increases.

Results above generally show that both storage and loss moduli increase with increasing magnetic flux density, ranging from 0 to 1 T, irrespective of loading frequency and strain amplitude. Additionally, both the storage and loss moduli increase with increasing frequency and tend to become saturated when loading frequency exceeds 6 Hz. This phenomenon so-called strain-rate stiffening phenomenon has also been observed in (Meyers, 2012) under specific loading condition. This is because of the relaxation time of large molecules within MRE matrix, which cannot respond as fast as excitation input, thereby, experiencing more cyclic forces before relaxing, leading to stiffening of the matrix (Vatandoost et al., 2017).

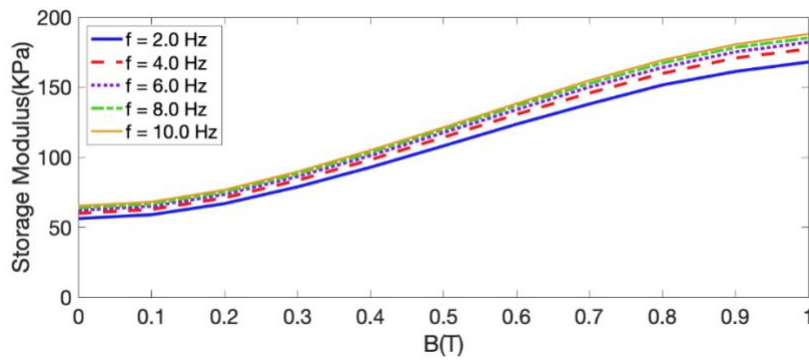


(a)

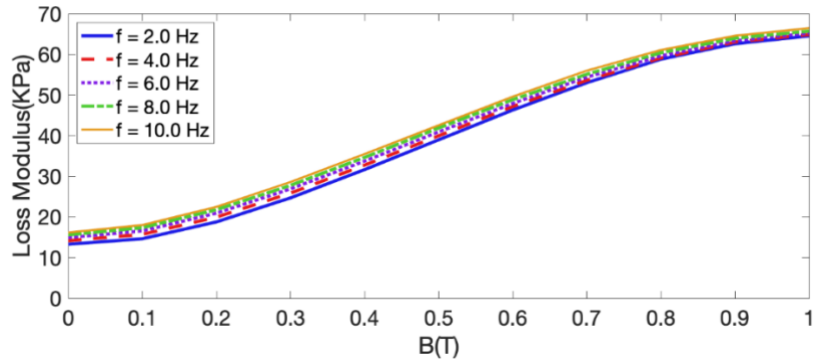


(b)

Figure 4.2: Variation of storage (a) and Loss (b) moduli with respect to applied magnetic flux densities for different loading frequency (Strain amplitude 15%).



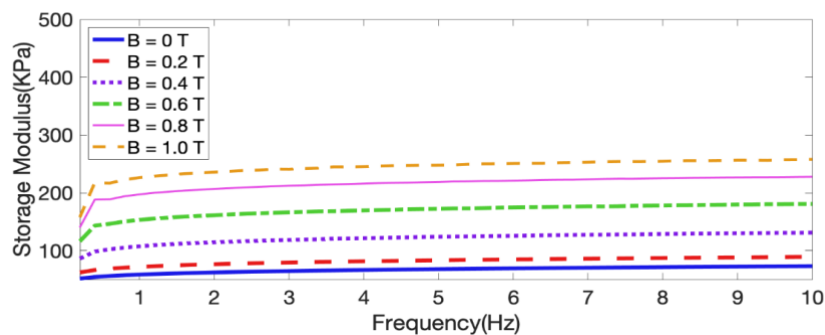
(a)



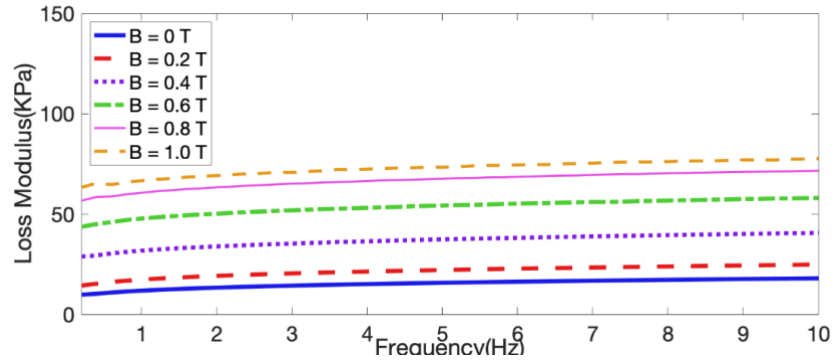
(b)

Figure 4.3: Variation of storage (a) and Loss (b) moduli with respect to applied magnetic flux densities for different loading frequency (Strain amplitude 30%).

Figure 4.4 illustrates the variation of both storage and loss moduli with respect to loading frequency, ranging from 0.2 Hz to 10 Hz for strain amplitude of 15%. Results shown in Figure 4.4 (a) were indicative of a nonlinear increment of storage modulus when frequency increasing from 0.2 Hz to 1 Hz. This is mainly because of transition from quasi-static regime to dynamic regime. It is noted that the slope of increment increases as the applied magnetic field increases. The storage modulus then tends to increase linearly (with very small positive slope) when frequency increases from 1 Hz to 10 Hz. Figure 4.4 (b) shows the variation of loss modulus with respect to frequency. It can be seen that loss modulus increases almost linearly with very small upward (positive) slope by increasing loading frequency.



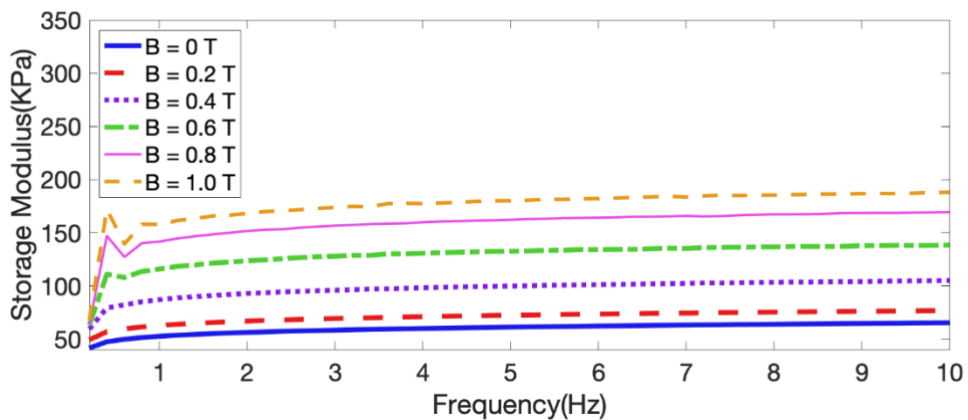
(a)



(b)

Figure 4.4: Variation of storage (a) and Loss (b) moduli with respect to frequency for different applied magnetic flux densities (Strain amplitude 15%).

Figure 4.5 shows the variation of storage and loss moduli with respect to loading frequency for strain amplitude of 30%. Results similarly show that the storage modulus increases slightly with increasing the loading frequency from 0.2 to 10 Hz irrespective of magnetic flux density. Examination of results reveal that at relatively higher level of magnetic field, storage modulus increases very rapid when frequency increases from 0.2 to 0.4 Hz and then with further increase in frequency it slight decreases. This behavior may be due to extremely nonlinear behavior of MRE at large strain amplitude and very low frequency range. With further increase in frequency, the storage modulus tends to increase relatively in a linear manner (very small positive slope) with respect to frequency. For instance, for magnetic flux density of 0.6 T when frequency increases from 1 to 10 Hz the storage modulus varies from 120 kPa to 135 kPa corresponding to a relative increment of 12.5 %



(a)

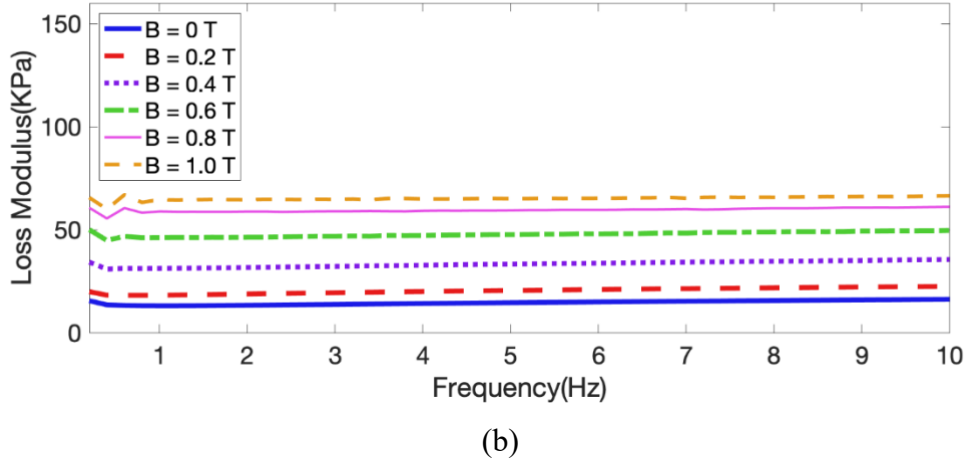


Figure 4.5: Variation of storage (a) and Loss (b) moduli with respect to frequency for different applied magnetic flux densities (Strain amplitude 30%).

Furthermore, further analysis of Figure 4.4 and Figure 4.5 show that both the storage and loss moduli for strain amplitude of 15% are higher than those of corresponding moduli for strain amplitude of 30%, irrespective of magnetic flux density. This confirms the strain softening of MREs at higher strain amplitudes.

4.2.4 Formulation of Dynamic Properties of MREs

Phenomenological data driven models are developed to predict the viscoelastic properties of the tested MREs as function of loading frequency and magnetic flux density. Based on the observed results, the variation of the MRE's storage G' and loss G'' moduli with respect to the driving frequency can be represented by a combination of gaussian and power functions. It is important to note that the selected function for magnetic field can represent the magnetic saturation of MRE modulus at high magnetic field to address this physical phenomenon. Hence, the mathematical models for the storage and loss moduli are formulated as:

$$G' (B, f) = \frac{2a_1 f^{a_2}}{1+e^{(-a_3(B+a_4))}} \quad (4-1)$$

$$G'' (B, f) = \frac{2b_1 f^{b_2}}{1+e^{(-b_3(B+b_4))}} \quad (4-2)$$

where G' and G'' represent the storage and the loss moduli, respectively, and both of them are functions of magnetic flux density (B) and excitation frequency (f). a_1, a_2, a_3, a_4 and b_1, b_2, b_3, b_4 are model's parameters to be determined through error minimization procedure. In order to obtain the parameters of the proposed model, the error functions are first defined as:

$$J_{G'} = \sum (G'_{\text{model}} - G'_{\text{expire}})^2 \quad (4-3)$$

$$J_G'' = \sum (G''_{\text{model}} - G''_{\text{expire}})^2 \quad (4-4)$$

By using the least square minimization method, the model parameters have been identified to minimize the errors between the predicted and the experimental results. Results for two different strain amplitude of 15% and 30% are provided in Tables 4.1 and 4.2, respectively.

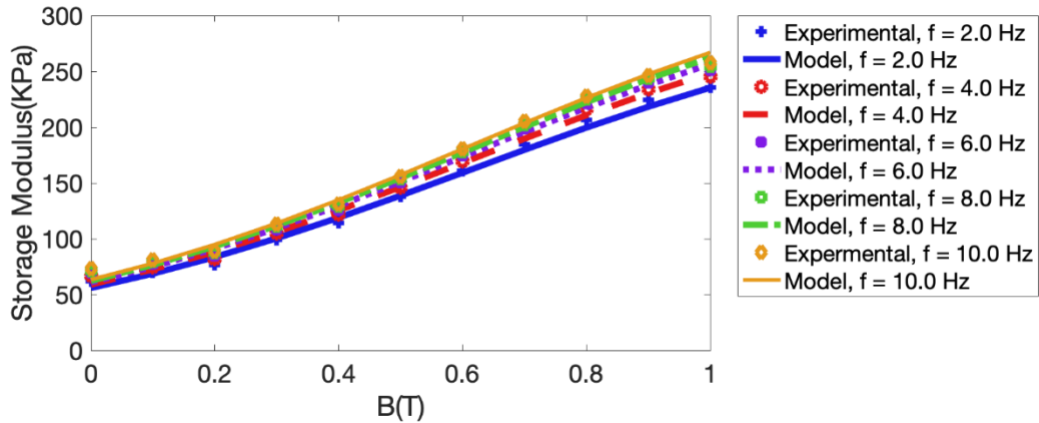
Table 4.1: Identified parameters (strain 15%)

a_1	a_2	a_3	a_4
$1.523 \cdot 10^5$	0.078	2.562	-0.608
b_1	b_2	b_3	b_4
$3.760 \cdot 10^4$	0.077	3.751	-0.452

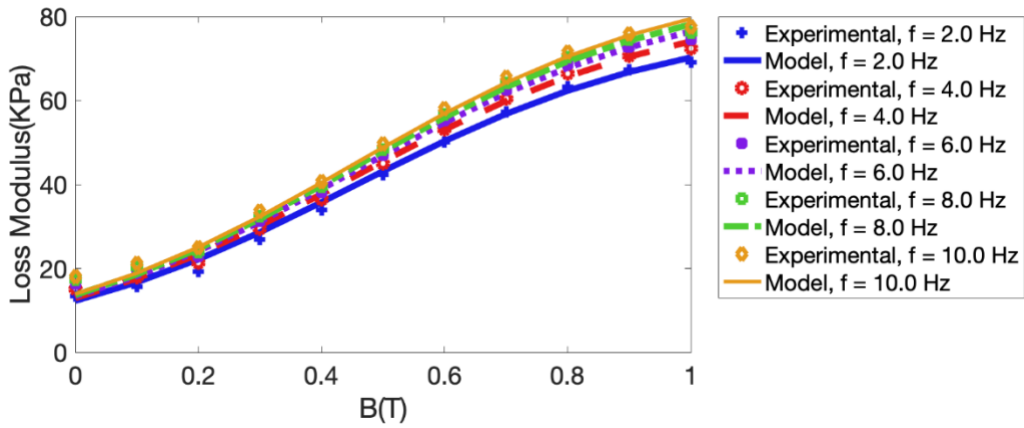
Table 4.2: Identified parameters (strain 30%).

a_1	a_2	a_3	a_4
$1.066 \cdot 10^5$	0.099	2.290	-0.563
b_1	b_2	b_3	b_4
$3.692 \cdot 10^4$	0.018	3.615	-0.458

Figure 4.6 shows the performance of the proposed model in prediction of storage and loss moduli for different loading frequencies and magnetic flux density for loading amplitude of 15%. Results show that the proposed model can effectively predict the behavior of MRE moduli as function of both loading frequency and magnetic flux density. Very good agreement exists between model and experimental results.



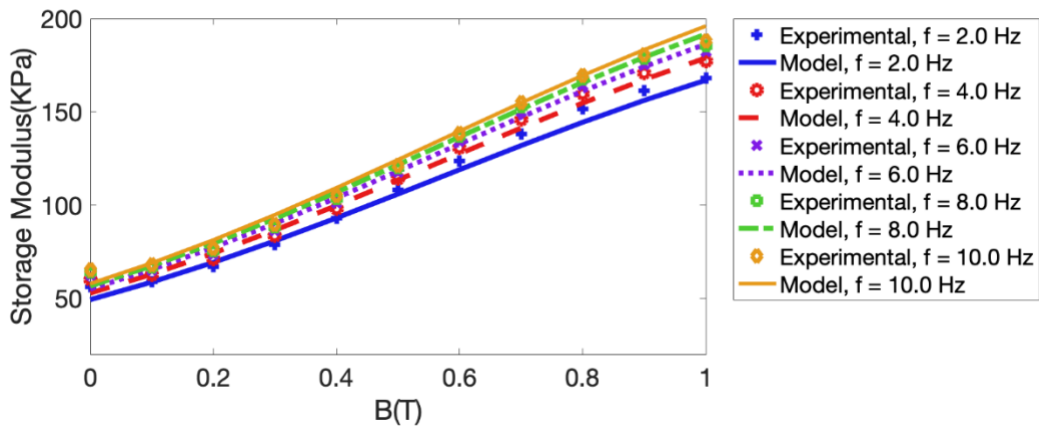
(a)



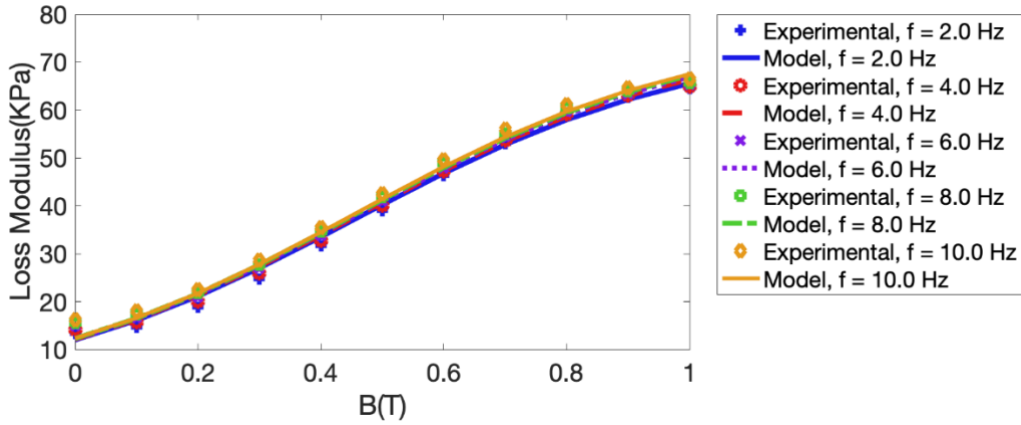
(b)

Figure 4.6: Comparison of storage and loss modulus prediction model with experimental data (Strain 15%).

Figure 4.7 also compares the model predicted storage and loss moduli with experimental data under different levels of loading frequency and magnetic flux density for loading amplitude set at 30%. Relatively similar agreements were obtained between the model and experimental results, when comparing to Figure 4.6.



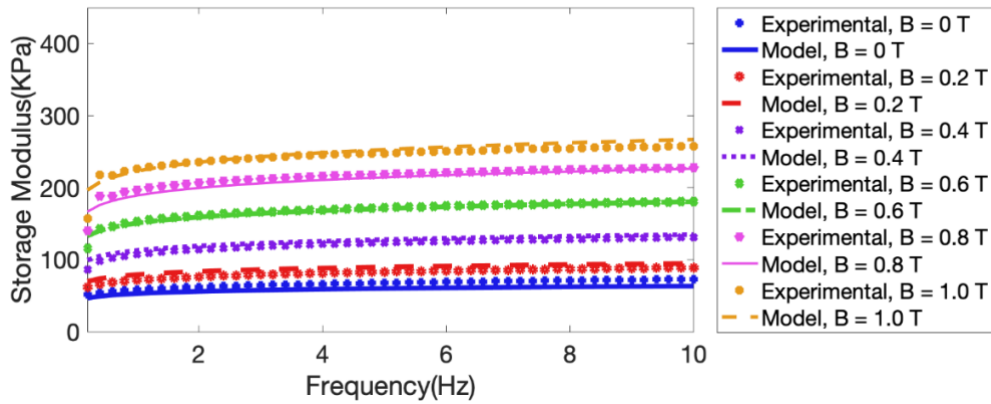
(a)



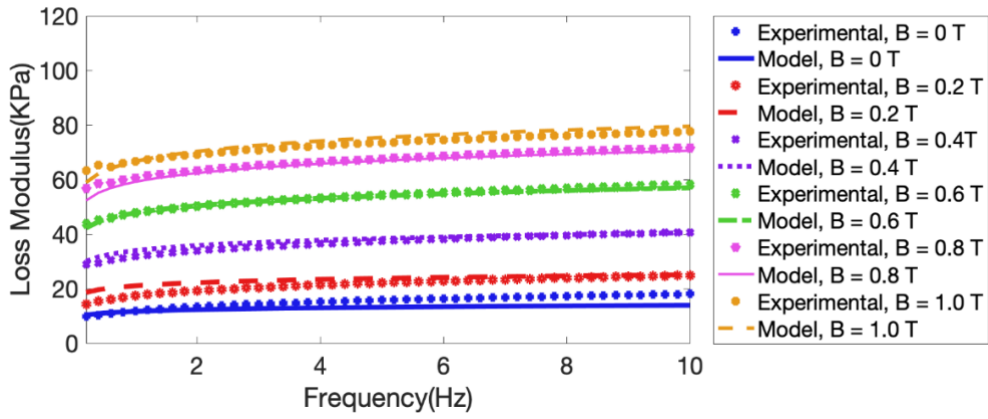
(b)

Figure 4.7: Comparison of storage and loss modulus prediction model with experimental data (Strain 30%).

Figures 4.8 and 4.9 further compare the results obtained by the proposed model and the experimental results, when storage and loss moduli are varied with respect to loading frequency for strain amplitude of 15% and 30%, respectively. The comparison also was applied for all the levels of magnetic flux densities, ranging from 0 T to 1 T.

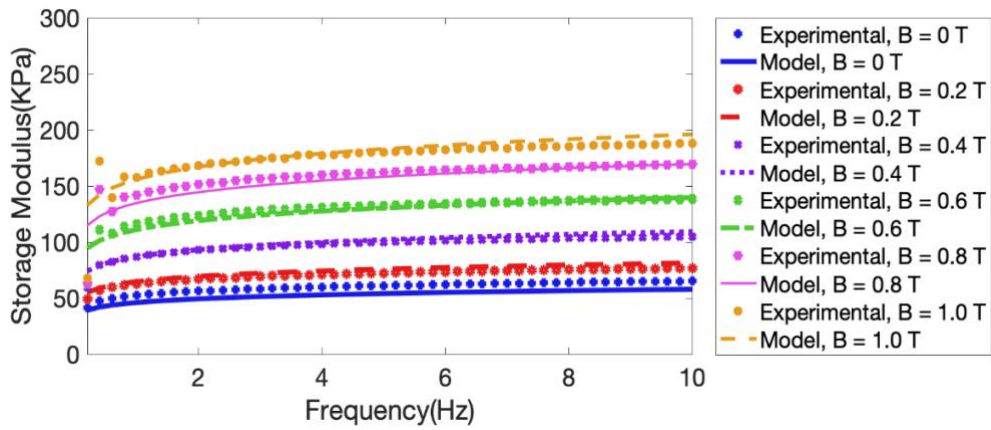


(a)

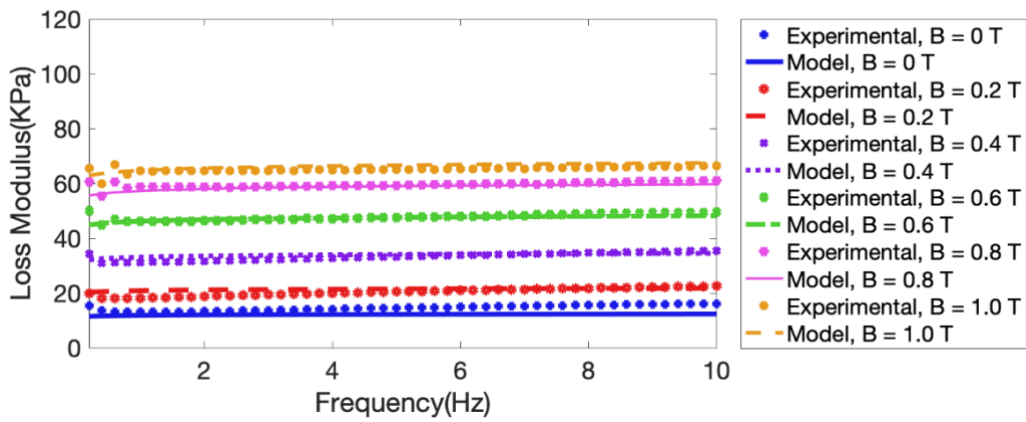


(b)

Figure 4.8: Comparison of storage and loss modulus prediction model with experimental data (Strain 15%).



(a)



(b)

Figure 4.9: Comparison of storage and loss modulus prediction model with experimental data (Strain 30%).

4.3 MRE-based Isolator Design

MREs show many potentials for applications in noise and vibration control, such as MRE isolators (Yang et al., 2013, 2016) and MRE absorbers (Sun et al., 2014, 2015) due to their variable stiffness and damping properties under the application of an external magnetic field. However, as compared with MR fluid, MREs demand relatively larger and bulkier electromagnet units to magnetically activate them as their total designed thickness is much higher than that of MR fluids. Thus, designing an electromagnetic unit which can provide enough magnetic field with minimal mass and space remains a continuous challenge in this field and thus need to be properly addressed. In this study, design optimization of an MRE-based vibration isolator or equipped with a C-shaped electromagnet is presented. The proposed MRE-based vibration isolator is expected to be used for seat suspension applications.

4.3.1 Schematic MRE Isolator

The sketch of the MRE isolator integrated with the seat suspension system is shown in Figure 4.10. Two cuboid MRE samples are installed in the middle of the electromagnet, which positioned underneath of the seat in order to leave some space for the passive suspension.

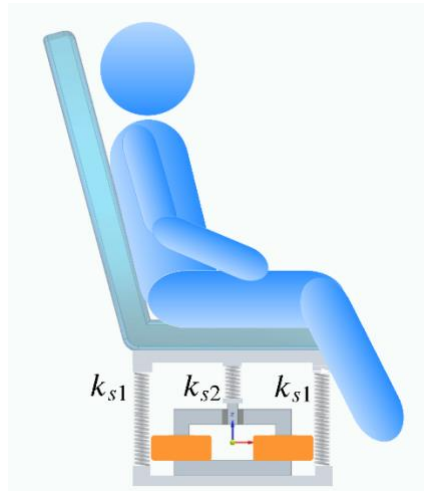


Figure 4.10: MRE isolator with parallel and series spring.

The schematic of the proposed MRE isolator with all important design parameters is shown in Figure 4.11. The MRE isolator consists of a connector that connects the seat to the MRE samples

from the upper section, a C-shaped steel core, two electromagnet coil windings, and two cuboid-shaped MRE samples under shear mode located in air gap. The geometrical parameters of the isolators are presented as x_1 to x_6 as shown in the Figure 4.11. It should be noted that x_c (thickness of the plate connecting the MREs to the connector) is assumed to be 20 mm. To design an electromagnetic circuit for MRE based isolator, it is required to maximize the magnetic flux density within MRE specimens in the gap of electromagnet while limiting space, mass and energy consumption of the isolator unit. At the same time, the off-state modulus of MREs should be sufficiently enough to withstand the weight of human operator on the seat.

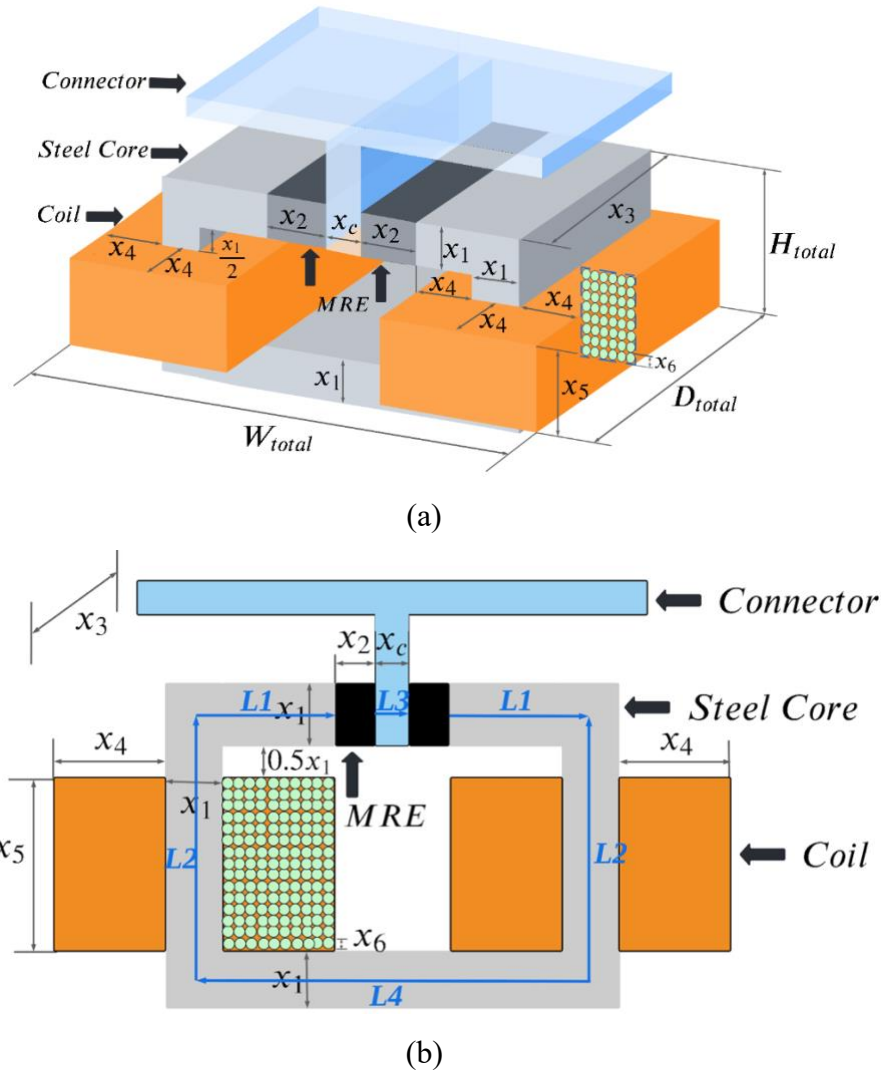


Figure 4.11: Schematic of Designed MRE Isolator: (a) 3D view, and (b) 2D view.

To implement the above-mentioned design optimization of the MRE isolator, the geometrical and physical parameters of the isolator unit should be related together using the Hopkinson's law (equivalent to Ohm's law in electrical circuits) as:

$$\oint H \cdot dl = NI = \mathcal{R}_t \phi \quad (4-5)$$

where H , and l are the applied magnetic field and length of the mean magnetic path of the core. N , I , \mathcal{R}_t , and ϕ are the copper wires' total number of turns, applied electrical current, total reluctance of the circuit, and magnetic flux in the air gap of the C-shaped core. Thus, substituting the length and reluctance of different part of the electromagnet circuit in equation (4-5) can yield:

$$NI = \phi(2\mathcal{R}_{MRE} + \mathcal{R}_{core}) \quad (4-6)$$

The reluctances of MRE and magnetic core can be calculated as $\mathcal{R}_{core} = l_{core}/(\mu_{core}A_{core})$, and $\mathcal{R}_{MRE} = l_{MRE}/(\mu_{MRE}A_{MRE})$. l_{core} , A_{core} , and μ_{core} are the length of steel core, cross-sectional area, and permeability. These can be similarly defined for MRE magnetic materials. As it can be seen in Figure 4.11, the cross-sectional areas of the core and MRE are the same, $A_{core} = A_{MRE}$. The number of coil turns can be approximated as (Vatandoost et al., 2020):

$$N = 2(fx_4x_5/A_{wire}) \quad (4-7)$$

where f is the practical filling factor of 0.8 when wrapping conductor wire around the bobbin core (Kazimierczuk, 2009). $A_{wire} = \pi x_6^2/4$ is the cross-sectional area of the conductor wire and x_6 is the diameter of the conductor wire. Besides, considering the continuity of the flux within a closed path magnetic circuit, the magnetic flux ϕ can be calculated as multiplication of magnetic flux density of MRE with its cross-sectional area:

$$\phi_{MRE} = B_{MRE}A_{MRE} = B_{MRE}x_1x_3 \quad (4-8)$$

4.3.2 Formulation of the Design Optimization

The aim is to maximize the magnetic flux density (B_{MRE}) passing through the electromagnet air gap filled with the MRE specimens. Considering equations (4-5) through (4-8), B_{MRE} can be calculated as:

$$B_{MRE} = \frac{NI}{\frac{1}{\mu_0} \left(\frac{2l_{MRE}}{\mu_{rMRE}} + \frac{l_{core}}{\mu_{rcore}} \right)} \quad (4-9)$$

where μ_0 is the vacuum permeability ($4\pi \times 10^{-7}$). $\mu_{r_{MRE}}$ and $\mu_{r_{core}}$ are the relative magnetic permeability of MRE and steel core materials, which their values are assumed to be around 3 and 1000, respectively (Vatandoost et al., 2020). Using Figure 4.11(b), the length of the steel core, l_{core} , and MRE, l_{MRE} , can be evaluated as:

$$l_{core} = 2L_1 + 2L_2 + L_3 + L_4 \quad (4-10)$$

$$L_1 = 0.5x_1 + x_4 \quad (4-11)$$

$$L_2 = x_5 + 2 \times 0.5x_1 + 0.5x_1 \quad (4-12)$$

$$L_3 = x_c \quad (4-13)$$

$$L_4 = x_c + 2L_1 + 2x_2 \quad (4-14)$$

$$l_{MRE} = 2x_2 \quad (4-15)$$

substituting Eq. (4-11) to (4-14) into Eq. (4-10) yields:

$$l_{core} = 5x_1 + 2x_2 + 4x_4 + 2x_5 + 2x_c \quad (4-16)$$

thus, the optimization can be formally formulated as minimization of the cost function J:

$$\text{Minimize: } J(\theta) = -B_{MRE} \quad (4-17)$$

where θ is the design parameters:

$$\theta = [x_1, x_2, x_3, x_4, x_5, x_6] \quad (4-18)$$

It is noted that the current I is set at 2A.

The above optimization is subjected to the following constraints including but are not limited to physical, geometrical and design requirements of the seat suspension:

$$\begin{aligned} 100 \text{ mm} &\leq H_{total} \leq 280 \text{ mm} \\ 100 \text{ mm} &\leq W_{total} \leq 400 \text{ mm} \\ 100 \text{ mm} &\leq D_{total} \leq 150 \text{ mm} \\ 5 \text{ kg} &\leq M_{total} \leq 25 \text{ kg} \\ 2.5 \text{ kN/m} &\leq k_{MRE_{off-state}} \\ 20 \text{ kN/m} &\leq k_{MRE_{on-state}} \\ CD &\leq 5 \end{aligned} \quad (4-19)$$

where H_{total} , W_{total} and D_{total} are the total height, width and depth of the MRE isolator device (constraint volume), respectively, as shown in Figure 4.11 (a). M_{total} is the total mass of the MRE isolator, and CD is the current density passing through the coil. $k_{MRE_{off-state}}$ and $k_{MRE_{on-state}}$

are the total quasi-static stiffness of MREs under zero and maximum magnetic flux density, which can be obtained from the shear storage modulus, according to Figure 4.11, as:

$$k_{\text{MRE}} = \frac{G'(\text{B},\omega)A_{\text{MRE}}}{l_{\text{MRE}}} = \frac{G'(\text{B},\omega)x_1x_3}{2x_2} \quad (4-20)$$

Noted that, the damping of MREs can be also related to the shear loss moduli as

$$c_{\text{MRE}} = \frac{G''(\text{B},\omega)A_{\text{MRE}}}{\omega l_{\text{MRE}}} = \frac{G''(\text{B},\omega)x_1x_3}{\omega 2x_2} \quad (4-21)$$

Table 4.3: Optimization Parameters.

Parameters	Optimized output	Lower bound	Upper bound
x_1 (mm)	30	30	150
x_2 (mm)	25	25	60
x_3 (mm)	100	100	250
x_4 (mm)	20	20	250
x_5 (mm)	45	30	250
x_6 (mm)	0.723	0.511	2.588
Number of turns		1838	

GA was initially used first to obtain the near-global minimum solution due to the stochastic nature of GA algorithm. SQP algorithm was subsequently used in which the optimal parameters from GA were used as initial inputs. SQP is a nonlinear gradient-based optimization algorithm capable of accurately capturing the local optimum solution near to starting initial point. Thus, combining GA and SQP will result a true global optimum solution. Repeating this procedure for many randomly generated initial points has resulted to the same optimum solution provided in Table 4.3. It is worth noting that, substituting the optimal parameters into Eq. (4-9), yields the following simple and linear relationship between the applied current and magnetic flux density:

$$B = 0.2705I \quad (4-23)$$

Eq. (4-23) is linear due the fact that in the magnetic circuit design presented above, linear permeabilities were assumed for magnetic materials in the circuit for the sake of simplicity.

4.4 Design Optimization of the Semi-active Seat Suspension System featuring MRE

4.4.1 Mathematical description of seat suspension system

Figure 4.12 shows a 6-DOF system containing the proposed conceptual design of a semi-active seat suspension system based on the optimally designed MRE isolator. Three passive springs are designed to be in parallel and series to the MRE isolator as shown in Figure 4.12.

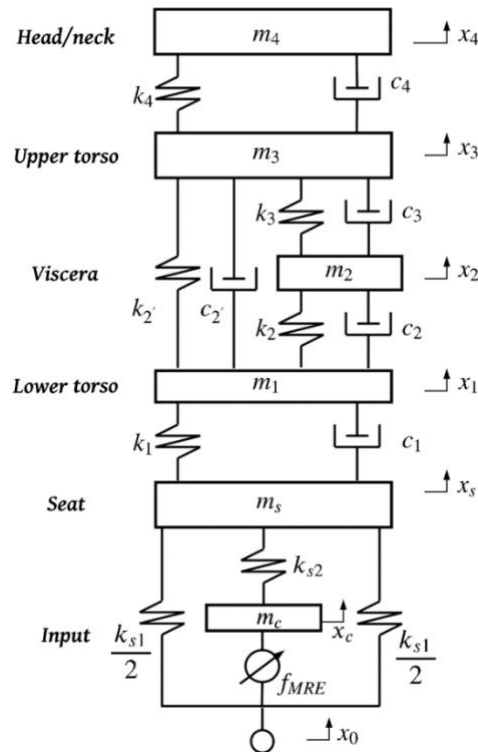


Figure 4.12: 6-DOF Lumped parameter model of seated human suspension system with MRE isolator.

The proposed configuration for the seat suspension allows large deformation of the seat while preventing MREs to undergo very large deformation which may substantially reduce their storage modulus. A design optimization was formulated to obtain optimal values of k_{s1} (parallel spring to the MRE isolator) and k_{s2} (spring in series with the MRE isolator) in such a way to maximize the frequency shift of the semi-active suspension system. The governing equations of the motion of the coupled seated human/semi-active seat suspension system shown in Figure 4.12 can be derived as:

$$m_4\ddot{x}_4 = k_4(x_3 - x_4) + c_4(\dot{x}_3 - \dot{x}_4) \quad (4-24)$$

$$m_3\ddot{x}_3 = k_2'(x_1 - x_3) + c_2'(\dot{x}_1 - \dot{x}_3) + k_3(x_2 - x_3) + c_3(\dot{x}_2 - \dot{x}_3) - k_4(x_3 - x_4) - c_4(\dot{x}_3 - \dot{x}_4) \quad (4-25)$$

$$m_2\ddot{x}_2 = k_2(x_1 - x_2) + c_2(\dot{x}_1 - \dot{x}_2) - k_3(x_2 - x_3) - c_3(\dot{x}_2 - \dot{x}_3) \quad (4-26)$$

$$m_1\ddot{x}_1 = k_1(x_s - x_1) + c_1(\dot{x}_s - \dot{x}_1) - k_2'(x_1 - x_3) - c_2'(\dot{x}_1 - \dot{x}_3) - k_2(x_1 - x_2) - c_2(\dot{x}_1 - \dot{x}_2) \quad (4-27)$$

$$m_s\ddot{x}_s = k_{s1}(x_0 - x_s) + k_{s2}(x_c - x_s) - k_1(x_s - x_1) - c_1(\dot{x}_s - \dot{x}_1) \quad (4-28)$$

$$m_c\ddot{x}_c = -k_{s2}(x_c - x_s) + k_{MRE}(x_0 - x_c) + c_{MRE}(\dot{x}_0 - \dot{x}_c) \quad (4-29)$$

The mass of the seat and seated human are considered to be 15 kg and 60.67 kg, respectively. The total mass of the MRE isolator's connector (nearly 100 g) is considered to be negligible

4.4.2 Optimization design of seat suspension system

The main goals for designing the parallel-series semi-active suspension are: (a) to allow large stroke for the suspension system while maintaining MRE to continue to operate within a reasonably low deformation (-7.5 mm ~ 7.5 mm); (b) increase the range of natural frequency of the system under a current range of 0-2 A; and (c) tolerate human body weight. Considering these design requirements, the design optimization problem can be formulated as: Find k_{s1} and k_{s2} to

$$\text{Minimize: } J = -(\omega_{n2} - \omega_{n1}) \quad (4-30)$$

where ω_{n1} and ω_{n2} are the natural frequency (rad/s) of the seat under applied current of $I = 0$ A and $I = 2$ A, respectively. Thus, from now on, the index 1 and 2 in the subsequent equations denote the parameter value at zero current and maximum current of 2A. Widening the resonance frequency range should be realized by a suitable control algorithm, thereby achieving a better performance of the MRE isolator system in terms of vibration isolation. It is noted that:

$$f_{n1} = \frac{1}{2\pi} \sqrt{\frac{k_{eq1}}{m_{total}}} \quad (4-31)$$

$$f_{n2} = \frac{1}{2\pi} \sqrt{\frac{k_{eq2}}{m_{total}}} \quad (4-32)$$

$$k_{eq1} = k_{s1} + \left(\frac{k_{s2}k_{MRE1}}{k_{s2} + k_{MRE1}} \right) \quad (4-33)$$

$$k_{eq2} = k_{s1} + \left(\frac{k_{s2}k_{MRE2}}{k_{s2} + k_{MRE2}} \right) \quad (4-34)$$

$$x_c \leq 7.5\text{mm} \quad (4-35)$$

where f_{n1} and f_{n2} are the natural frequency (Hz) of the seat suspension system from cab-floor to seat under the input current of 0 A and 2 A, respectively. k_{eq1} and k_{eq2} are the equivalent stiffness of the suspension system. It is noted that displacement of spring k_{s1} is basically seat displacement x_s as shown in Figure 4.12. The inequality constraint (Eq. 4.35) makes the displacement of MRE isolator limited to maximum value of 7.5 mm. This maximum displacement corresponds to a shear strain of nearly 30%. This can be further illuminated by Figure 4.13, showing that an MRE working under shear mode. Noted that the optimal thickness of MRE is obtained as 25 mm, as discussed in previous section (Table 4.3). Hence, the maximum strain of the material, defined as $\gamma = \frac{\text{displacement}}{\text{initial thickness}}$ is limited to maximum 30%. The last constrain reveals that the force of spring k_{s2} should be equal to the force generated by MRE elastomers.

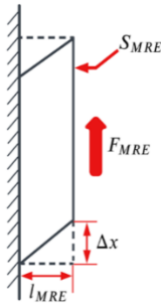


Figure 4.13: Schematic of MRE under shear mode.

The optimal values for passive springs in the proposed adaptive seat suspension are found to be 1.006 kN/m and 50kN/m for k_{s1} and k_{s2} , respectively. Optimal results together with lower and upper bounds are provided in Table 4.4. The equivalent stiffness of the optimized seat suspension system under zero current input is almost 8.9 kN/m while under applied current of 2 A, it is increased to 17.5 kN/m (Table 4.5). This corresponds to an absolute and relative increasement of 8.6 kN/m, and 96%, respectively.

Table 4.4: Optimized values of Parameters in MRE Isolator Design.

Stiffness	Optimization result	Lower bound	Upper bound
k_{s1} (N/m)	1006	1000	50000
k_{s2} (N/m)	50000	1000	50000

Table 4.5: Output values of optimized seat suspension.

Seat suspension coefficient	Optimized value
k_{eq1} (N/m)	8935
k_{eq2} (N/m)	17503
f_{n1} (Hz)	1.76
f_{n2} (Hz)	2.27

The natural frequency of the optimal adaptive seat suspension system varies from 1.76 Hz at zero current to 2.27 Hz at maximum current 2 A (29% relative frequency shift). The transmissibility from cab-floor to operator's head also is illustrated in Figure 4.15. Examination of results show that at in the frequency range of 4-10 Hz where the human shows the maximum sensitivity, rms transmitted acceleration is significantly reduced by the adaptive seat suspension under zero current compared with no suspension. For the low frequency range below 1 Hz, the adaptive seat suspension system under maximum current provides superior performance in which vibration transmissibility is slightly increased compared with no-suspension system.

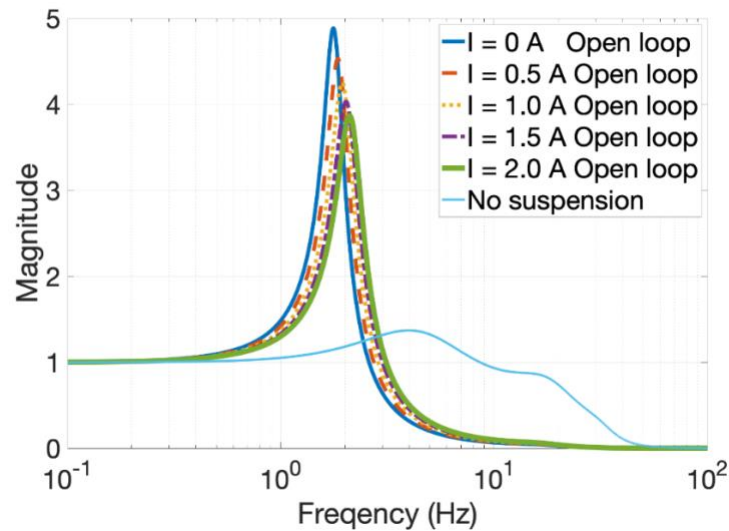


Figure 4.14: Transmissibility from cab-floor to operator's head for different currents.

4.5 Conclusion

The MRE samples were characterized in the laboratory in shear mode using a rotational magnetorheometer. The rheometer equipped with a magnetorheological attachment to measure its field-dependent viscoelastic properties of MREs. The tests were performed at different levels of applied

flux density from $B = 0$ T to $B = 1$ T over a wide frequency range, from 0.2 Hz to 10 Hz, while the temperature was kept stable at 20 °C. The tests were performed for two levels of strain amplitudes (15%, 30%). The effects of loading conditions (e.g., frequency and strain amplitude) and magnetic field strength on the elastic and loss moduli of MREs were studied and discussed. The results show that the mechanical properties such as storage and loss moduli significantly increase by increasing the applied magnetic field and tend to saturate at higher level of magnetic field ($B > 0.9$ T). The experimental characterization yielded development of field and frequency dependent phenomenological models. The developed models can predict the dynamic behavior of MREs over a relatively wide ranges of magnetic field and loading frequency. Subsequently, a C-shaped MRE isolator was optimally designed to yield maximum flux density in the gap while minimizing the total weight of isolator under different physical, geometrical, and seat suspension design requirements. To allow large deformation of the seat while maintaining MREs to be operated within nearly linear regime at relatively lower level of strain amplitude, three passive springs were incorporated to the semi-active seat. Two springs are parallel while one in series to the MRE isolator unit. The values of the optimal spring rate of the passive springs were subsequently identified to yield maximum frequency shift of the seat. Increasing current from zero to maximum 2 A, resulted in increasing the equivalent stiffness of the seat from 8.9 kN/m to 17.5 kN/m under relatively lower level of frequency, where human shows maximum sensitivity. The system's resonance frequency can be increased from 1.76 Hz to 2.27 Hz, corresponding to a frequency shift percentage of 28.98%.

Chapter 5: Development of Controllers for the Semi-Active Seat Suspension System

5.1 Introduction

The physical parameters (ex. stiffness and damping) of semi-active seat suspensions (e.g., those featuring MR materials) can be adjusted in response to varied excitation inputs. Over the past decades, the semi-active seat suspension systems have received many attentions. Choi and Wereley (Y. T. Choi & Wereley, 2022) designed an adaptively tunable MRE-based vibration absorber to improve the vibration reduction of a propeller aircraft seat. Sun et al. (Du et al., 2013) proposed a horizontal MRE-based vibration isolator to enhance the vibration isolation performance of a seat suspension. The adjustability of semi-active seat parameters can be only realized via a suitable control algorithm in response to an excitation input, thereby providing appropriate and essential coil current, and thus the magnetic field for MR materials. Various closed-loop control algorithms have been investigated to reduce the vibration transmissibility of a semi-active system efficiently (Nguyen et al., 2018; Stelzer et al., 2003; Vidya & Dharmana, 2017). Novel controllers inspired by machine learning algorithms have also gained significant interests in the recent years, such as Takagi-Sugeno fuzzy control (T-S Fuzzy) (Du et al., 2013; Kurczyk & Pawelczyk, 2013), neural network control (Liu et al., 2020) and neural network (NN)-PID control (Lin et al., 2015). Pang et al., (Pang et al., 2018) proposed a novel particle swarm optimization (PSO)-Fuzzy neural network (FNN) controller (PSO-FNN), that combines the advantages of PSO and NN, for adjusting the parameters of a vehicle semi-active seat suspension system featuring an MR damper. Results show that the designed controller can improve vibration mitigation performance of the seat under varied road excitations. Such innovative controller has not been applied for controlling MRE-based devices (e.g., MRE isolators/absorbers).

The purpose of this chapter is to propose a novel PSO-FNN controller to tune the physical parameters of the developed semi-active seat suspension system featuring an MRE-isolator and three parallel/series springs. Unlike the most previous studies on FNN controllers which typically use the Takagi-Sugeno algorithm, I developed the FNN part based on a descriptive based algorithm, namely, Mamdani method. The proposed PSO-Mamdani-based FNN, henceforth PSO-FNN, controller has never been developed for MRE-based devices. The goal is to find a real-time current command for MRE-isolator unit in order to minimize the cab-floor to head transmissibility in

response to a disturbance (e.g., input pulse or transient/steady state vibration) using the developed control algorithm. In this regard, a PSO algorithm is used to globally optimize the parameters of the membership functions (MFs) of the fuzzy-neural-network (FNN) algorithm. To accomplish this, the PSO algorithm is, firstly, compiled with a simple Mamdani-based fuzzy logic controller (FLC) as the training section. The detailed explanation of the training procedure will be illustrated in the subsequent section. The global optimized parameters are, subsequently, used in the FNN in order to meet the requirements of fast computing speed and high computational accuracy. Meanwhile, the concept of weighting factors according to neural network algorithm is adopted to locally optimize the MFs at the output layer in FNN controller. This is to compensate the equal width between each membership functions, so as to further improve the accuracy but avoid tedious calculation steps. The developed PSO-FNN controller is also compared with the classical On-Off (Skyhook) control algorithm. Finally, the performance of the controller for reducing the cab-floor to head transmissibility is evaluated under different external excitations. The excitations include superimposed harmonic motions, random noise, harmonics superimposed with random noise, and bump shocks.

5.2 The state-space model of 6-DOF system

Figure 5.1 shows again the 6-DOF model formulated in Chapter 4 for the sake of clarity. To facilitate the development of the control algorithm, a state-space model is formulated using Eqs. (4-24) to (4-29) in section 4.4 in Chapter 4.

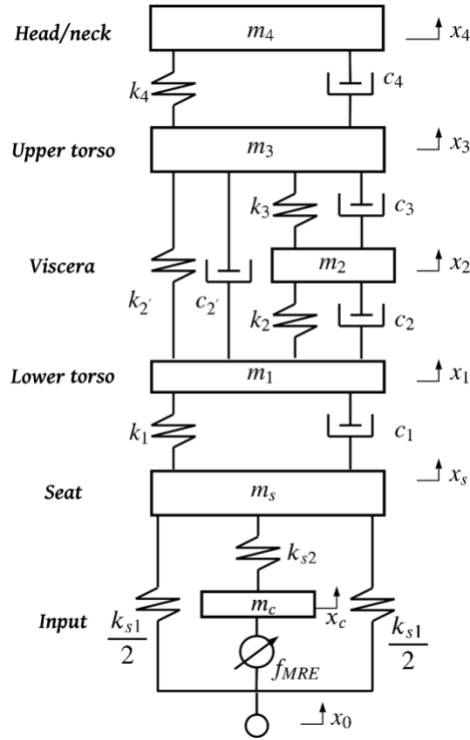


Figure 5.1: 6-DOF Lumped parameter model of seated human suspension system with MRE isolator

The mass, stiffness and damping matrices can be obtained using Eqs. (4-24) to (4-29) as:

$$M = \begin{bmatrix} m_4 & 0 & 0 & 0 & 0 & 0 \\ 0 & m_3 & 0 & 0 & 0 & 0 \\ 0 & 0 & m_2 & 0 & 0 & 0 \\ 0 & 0 & 0 & m_1 & 0 & 0 \\ 0 & 0 & 0 & 0 & m_s & 0 \\ 0 & 0 & 0 & 0 & 0 & m_c \end{bmatrix} \quad (5-1)$$

K =

$$\begin{bmatrix} k_4 & -k_4 & 0 & 0 & 0 & 0 \\ -k_4 & k_2' + k_3 + k_4 & -k_3 & -k_2' & 0 & 0 \\ 0 & -k_3 & k_2 + k_3 & -k_2 & 0 & 0 \\ 0 & -k_2' & -k_2 & k_1 + k_2' + k_2 & -k_1 & 0 \\ 0 & 0 & 0 & -k_1 & k_{s1} + k_{s2} + k_1 & -k_{s2} \\ 0 & 0 & 0 & 0 & -k_{s2} & k_{MRE} + k_{s2} \end{bmatrix} \quad (5-2)$$

C =

$$C = \begin{bmatrix} c_4 & -c_4 & 0 & 0 & 0 & 0 \\ -c_4 & c_2' + c_3 + c_4 & -c_3 & -c_2' & 0 & 0 \\ 0 & -c_3 & c_2 + c_3 & -c_2 & 0 & 0 \\ 0 & -c_2' & -c_2 & c_1 + c_2' + c_2 & -c_1 & 0 \\ 0 & 0 & 0 & -c_1 & c_1 & 0 \\ 0 & 0 & 0 & 0 & 0 & c_{MRE} \end{bmatrix} \quad (5-3)$$

The state vectors are defined as:

$$X = [x_4, x_3, x_2, x_1, x_s, x_c]^T \quad (5-4)$$

$$\dot{X} = [\dot{x}_4, \dot{x}_3, \dot{x}_2, \dot{x}_1, \dot{x}_s, \dot{x}_c]^T \quad (5-5)$$

Thus, by forming,

$$Y = \begin{bmatrix} \dot{X} \\ X \end{bmatrix} \quad (5-6)$$

$$\dot{Y} = \begin{bmatrix} \ddot{X} \\ \dot{X} \end{bmatrix} \quad (5-7)$$

$$A = \begin{bmatrix} [M] & [0] \\ [0] & [I] \end{bmatrix} \quad (5-8)$$

$$B = \begin{bmatrix} [C] & [K] \\ [-I] & [0] \end{bmatrix} \quad (5-9)$$

one can write the governing equations of motion in as a state-space form as:

$$[A]\dot{Y} + [B]Y = F(t) \quad (5-10)$$

in which

$$F(t) = [0,0,0,0, k_{s1}x_0, (k_{mre}x_0 + c_{mre}\dot{x}_0),0,0,0,0,0] \quad (5-11)$$

Using finite difference method, \dot{Y} , in Eq. (5.10) can be approximated as:

$$\dot{Y} = \frac{Y_{t+1} - Y_t}{\Delta t} \quad (5-12)$$

Thus Eq. (10) can be written as:

$$[A] \frac{Y_{t+1} - Y_t}{\Delta t} + [B]Y_t = F(t) \quad (5-13)$$

and solving for Y_{t+1} yields:

$$Y_{t+1} = Y_t + \Delta t[A]^{-1}(F(t) - [B]Y_t) \quad (5-14)$$

Thus, the displacement, velocity and acceleration at each time step can be obtained using previous time step information.

The input signal from the cab-floor is regarded as the main disturbance signal entering into the seat suspension system. Various input excitations have been considered to investigate the performance of the design controllers. Particularly, superimposed harmonic excitations in which rotor passage frequencies of Bell-412 helicopter as provided in Table 5.1 (Wickramasinghe, 2013) has been superimposed and applied with and without random noise to the base floor of the optimally designed MRE-based seat suspension. Performance evaluation has also been conducted under purely random excitation and transient bump shock.

Table 5.1: Synthesized Helicopter Floor Reference Signal.

Frequency (Hz)	5.4	10.8	16.2	21.6	27	32.4	37.8	43.2
Harmonic (N/rev)	1/rev	2/rev	3/rev	4/rev	5/rev	6/rev	7/rev	8/rev
Amplitude (g)	0.03	0.03	0.01	0.03	0.01	0.01	0.01	0.03

It is noted that the input is in the form of base acceleration as given in Eq. (5-15). However, in the state-space model, a description of displacement and velocity are required. These can be obtained by taking integration of the input acceleration as:

$$a_0 = A \sin(\omega t) \quad (5-15)$$

$$x_0 = \frac{-A \sin(\omega t)}{\omega^2} \quad (5-16)$$

$$v_0 = \frac{-A \cos(\omega t)}{\omega} \quad (5-17)$$

5.3 On-Off Skyhook Control

The implementation of semi-active suspension is possible using several control approaches. The skyhook control rule proposed by Karnopp et al. (Krasnicki, 1981), has been widely adopted in many reported studies (Ivers & Miller, 1989) as a simple yet effective and practical algorithm for the semi-active suspensions. It has been shown that the skyhook control limits the resonant oscillations of the spring mass to achieve superior vibration attenuation in the isolation frequency region. Rakheja and Sankar (Rakheja & Sanka, 1986) developed a straightforward on-off control strategy where the on-off state of the MR damper are determined by the displacement and relative velocity information between the base input and the mass where the MR damper is connected. An On-Off Skyhook controller for the proposed seat suspension can be simply described as:

$$I = \begin{cases} 2 \text{ A, } \dot{x}_s(\dot{x}_s - \dot{x}_0) \geq 0 \\ 0 \text{ A, } \dot{x}_s(\dot{x}_s - \dot{x}_0) < 0 \end{cases} \quad (5-18)$$

where I is the controllable current input to MRE isolator. The relationship between the magnetic flux density in the MRE region and applied current were obtained using optimal configuration of MRE isolator described in Chapter 4 (see Eq. (4-23)).

The induced MRE force can be written as:

$$F_{\text{MRE}} = k_{\text{MRE}}(x_0 - x_c) + c_{\text{MRE}}(\dot{x}_0 - \dot{x}_c) \quad (5-19)$$

where k_{MRE} and c_{MRE} the stiffness and damping of MREs, which have been described and formulated using the optimal configuration of MRE isolator described in Chapter 4 (see Eq. (4-20) and Eq. (4-21)). Substituting for k_{MRE} and c_{MRE} the optimal configuration of MRE isolator in Eq. (5-19) yields:

$$F_{\text{MRE}} = 0.15G'(B, f)(x_0 - x_c) + (0.15/\omega)G''(B, f)(\dot{x}_0 - \dot{x}_c) \quad (5-20)$$

where $G'(B, f)$ and $G''(B, f)$ are the field and frequency dependent storage and loss moduli derived in Chapter 4. x_0 and x_c denote the displacement of cab-floor/excitation and the MRE isolator's connector, respectively and \dot{x}_0 and \dot{x}_c are the velocity of the cab-floor/excitation and the MRE isolator's connector.

5.4 Particle Swarm Optimization-Fuzzy Neural Network Control

The block diagram of the proposed PSO-FNN is shown in Figure 5.2. The acceleration of the operator's head (a_4) and the relative velocity of the seat and floor (v_r) are measured parameters under the base excitation transmitted to the seat suspension system from the cab floor. These signals will be collected for the first 0.1 second duration as the training set of the PSO-FLC algorithm. The sampling frequency is considered as 1000 Hz (sampling at each 0.001 sec). The acceleration of the operator's head acceleration and relative velocity of the seat and floor response signals are also input to the FNN controller.

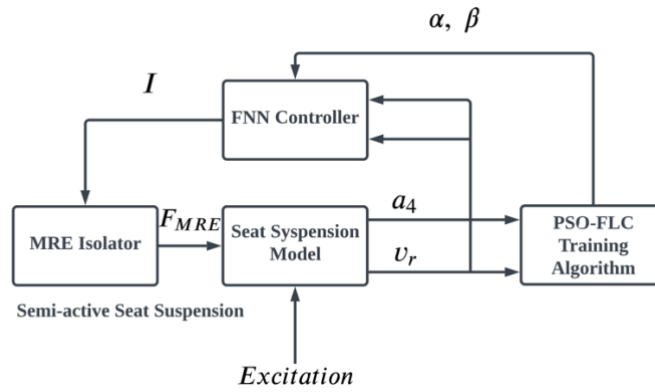


Figure 5.2: PSO-FNN Controller Diagram.

The primary purpose of the PSO-FLC training algorithm is to identify optimal parameters of the membership functions (MF) of the FNN controller. The FNN controller has two inputs: The first input (a_4) is the acceleration of head, and the second input (v_r) is the relative velocity between seat and cab-floor. The output of the FNN controller is the control current I to magnetically activate the MRE isolator unit. The gaussian membership functions are adopted for the FNN controller. Each set of fuzzification functions combines seven gaussian functions. Here, for the sake of simplicity, each gaussian function's width is assumed to be the same, and the distance between center (mean value) of each function to the adjacent function is also considered to be the same as shown in Figure 5.3. Considering this, the start and end points of each fuzzy set's horizontal axis (for instance $-\alpha$ and α for the input acceleration head) are the only parameters that required to be optimally identified from which the center positions of each MFs at equal intervals can be subsequently identified. It is noted $-\alpha$ and α are the start and end point of input 1, acceleration of the head (a_4) as shown in Figure 5.3, Similarly, the start and end point of the input 2, relative velocity between seat and cab floor (v_r), are $-\beta$ and β . It is worth mentioning that the start and end points of the output layer are fixed as -2 and 2 , respectively, as the minimum and maximum values of the control current. The current will vary within the range from 0 - 2 A, when the command current of FNN is lower than 0 A, the output current will be set as 0 A.

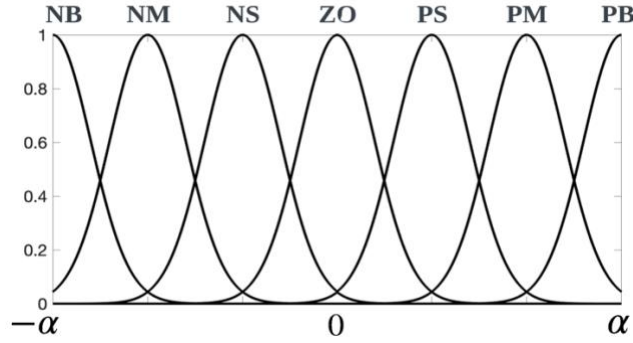


Figure 5.3: FNN controllers' optimized membership functions

5.5 PSO-FLC training procedure

To find α and β in detail, firstly, 50 sets of initial particles, where the position of each particle demonstrates the MFs parameters' information, are randomly generated for the PSO. Thus, there are 50 different FLC at each generation. Then, two FLC input signals: Input 1 (a_4) and Input 2 (v_r) firstly go through the FLC controller, and the output current I would activate the MRE-based isolator to adjust the mechanical properties of seat suspension. The rms of a_4 under the control of each FLC is collected as the fitness value of PSO algorithm. The objective is to find the globally best MFs parameters to minimize the acceleration response of head.

After the PSO-FLC training procedure, the fuzzification layer of the FNN controller is fixed while a_4 and v_r are still used as inputs to the FNN controller. The principle of FNN will be explained in detail later. The backpropagation is basically utilized to achieve a fast real-time local optimal solution while maintaining the accuracy due to the equal width of each MFs.

5.5.1 Mamdani-Based Fuzzy Neural Network Control

A fuzzy neural network is created to boost the effectiveness of fuzzy logic controllers (FLC). Mapping the fuzzy logic controller to the neural network (NN) architecture, will yield a real-time local optimization. The classical fuzzy logic control heavily relies on the expertise of control designers, which may substantially reduce the controller's accuracy. However, the combination of FLC and NN can simplify the reliance on the expert experience as compared with the traditional FLC up to a certain extent. There are two basic forms of FLC, one is Mamdani based FLC, the other one is Takagi-Sugeno based FLC (Klir & Yuan, 1995). Since Mamdani-based fuzzy logic controller uses language to describe mathematical relationships, this adds complexity to the traditional NN structures. As a result, the widely used Takagi-Sugeno based fuzzy NN controller

(TS-FNN) has been widely used (Takagi & Sugeno, 1985; Zhongyu et al., 2008). Although T-S FNN is intuitive and straight forward in mathematical calculation, there are too many parameters to be adjusted. The Mamdani-FNN has the benefit of operating more effectively in non-linear circumstances. Cai et al. (Chai et al., 2009) proposed the Mamdani model based adaptive neural fuzzy inference system that offers significant advantages in nonlinear modeling, evaluation of membership functions in consequent parts, the scale of training data, and the number of adjusted parameters. This is a new hybrid approach in computational intelligence. The computation procedure of Mamdani based FNN is discussed here.

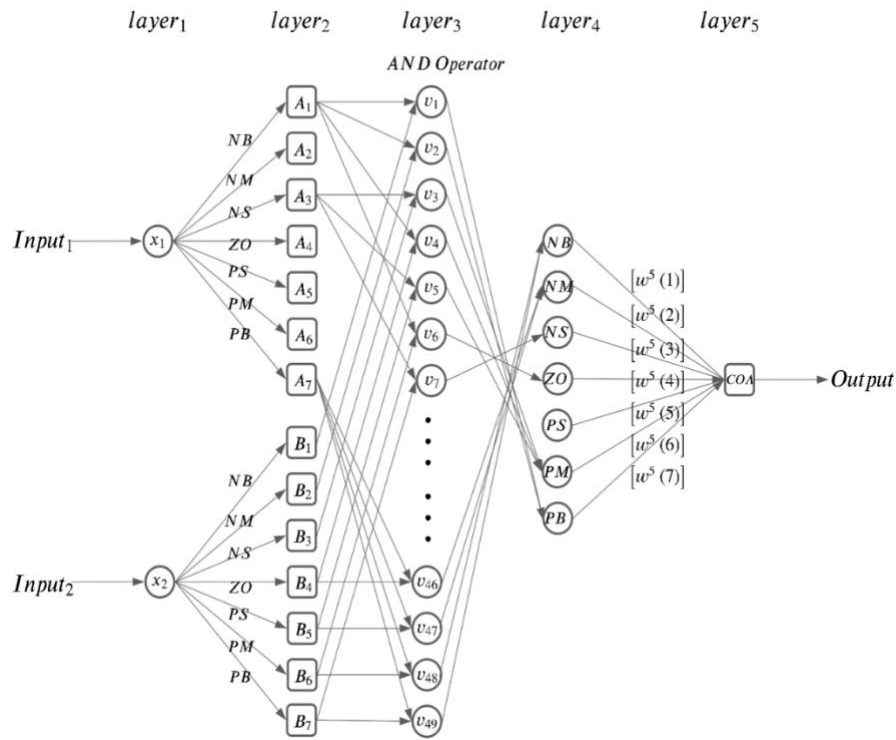


Figure 5.4: Architecture of Mamdani-based fuzzy neural network.

Figure 5.4 illustrates the structure of the Mamdani-based FNN (M-FNN). Input 1 and input 2 are the frequency weighted acceleration of head a_4 and the relative velocity between seat and cabin floor v_r respectively. I_n^i and O_m^i are defined as the input and output of the i^{th} layer, and the n and m are the number of neurons at each layer. Thus, considering Figure 5.4, we have:

Layer 1

$$I_1^1 = x_1 = O_1^1 \quad (5-21)$$

$$I^1_2 = x_2 = O^1_2 \quad (5-22)$$

It is noted that Layer 1 is the input layer, whose input and output are the same.

Layer 2

Layer 2 is the fuzzification layer. Here the gaussian membership function is adopted. c and σ are the center and the width of gaussian function respectively which are designed as:

$$O^2_{1,m} = \mu_{A_m} = e^{\frac{-(x_1 - c_{1,m})^2}{2\sigma_{1,m}^2}}, m = 1, 2, \dots, 7; \quad (5-23)$$

$$O^2_{2,m} = \mu_{B_{m-7}} = e^{\frac{-(x_2 - c_{2,m-7})^2}{2\sigma_{2,m-7}^2}}, m = 8, 9, \dots, 14. \quad (5-24)$$

in which μ_{A_m} and $\mu_{B_{m-7}}$ are the fuzzified values and also the input to layer 3.

Layer 3

Layer 3 is the implication layer with AND operator which can be mathematically expressed as:

$$O^3_{n,m} = \min(\mu_{A_n}, \mu_{B_m}), n = 1, 2, \dots, 7; m = 1, 2, \dots, 7. \quad (5-25)$$

Layer 4

Layer 4 is the fuzzy inference layer. The inference rules are provided in Table 5.2. The two inputs of the fuzzy controller are respectively NB (negative big), NM (negative medium), NS (negative small), ZO (zero), PS (positive small), PM (positive middle), PB (positive big) 7 language fuzzy sets to describe, forming 49 control rules. The destination of each neuron in Layer 3 is determined according to the descriptive rules in Table 5.2.

Table 5.2: Fuzzy logic control rules of control system.

F_{MRE}		a_4						
		NB	NM	NS	ZO	PS	PM	PB
v_r	NB	PB	PB	PM	PM	PM	PS	PS
	NM	PB	PM	PM	PS	PS	PS	ZO
	NS	PM	PM	PS	PS	ZO	NS	NM
	ZO	PM	PS	PS	ZO	NS	NS	NM
	PS	PM	PS	ZO	NS	NS	NM	NM
	PM	ZO	NS	NS	NS	NM	NM	NB
	PB	NS	NS	NM	NM	NM	NB	NB

Layer 5

Layer 5 is the defuzzification layer. The inputs of layer 5 are the output of layer 4 but being weighted by ω^5_n . The defuzzification method is selected as center of area (COA) (Klir & Yuan, 1995) as:

$$\text{COA} = \frac{\sum_{i=1}^7 (\text{Area}^4_i \cdot \text{Centroid}_i)}{\sum_{i=1}^7 \text{Area}^4_i} \quad (5-26)$$

where Area^4_i and Centroid_i are the area and geometric centers of each membership function in layer 4, respectively. The output of layer 5 can be obtained as:

$$O^5 = \frac{\sum_{i=1}^7 (\omega^5_i \cdot O^4_i \cdot \text{Centroid}_i)}{\sum_{i=1}^7 O^4_i} \quad (5-27)$$

A back-propagation procedure is implemented as a feedback process of the FNN controller. By using the gradient decent method, the weighing factor ω^5_n updated as:

$$E = \frac{1}{2} (d - O^5)^2 \quad (5-28)$$

$$\delta^5 = \frac{\partial E}{\partial O^5} = -(d - O^5) \quad (5-29)$$

$$\Delta \omega^5_i = \frac{\partial E}{\partial \omega^5_i} = \frac{\partial E}{\partial O^5} \cdot \frac{\partial O^5}{\partial \omega^5_i} = \delta^5 \cdot \frac{O^4_i \cdot \text{Centroid}_i}{\sum_{i=1}^7 O^4_i} \quad (5-30)$$

$$\omega^5_{i+1} = \omega^5_i - \eta \Delta \omega^5_i \quad (5-31)$$

E is the error function which is determined using the desired current d and the actual control current O^5 . η is the learning rate, which is selected as 0.1. The desired current can be obtained by comparing the magnitude of transmissibility under specific input frequencies. As Figure 4.14 illustrates, under a specific excitation frequency, in order to reduce the transmissibility from floor to head, there is a theoretical best value of input current, and the controller will be fine-tuned at this desired optimal input current, but because the actual external excitation has random noise, a constant current cannot be directly input. This is one of the important reasons why the input current needs to change at any time.

5.5.2 Particle Swarm Optimization-Fuzzy Training Algorithm

In the traditional FLC, the initial parameters are selected based on intuition and experience which pose some limitations in its practical applications. If the initial parameters are not properly selected and tuned, they may substantially affect and deteriorate the controller performance. In view of these shortcomings, a variety of feasible solutions have been proposed, one scheme is to utilize

global optimization algorithms such as simulated annealing, genetic and evolutionary algorithms to automatically identify the global optimal parameters of the FLC. Among stochastic based optimization algorithms, the PSO algorithm is a relatively new global optimization algorithm, which has attracted extensive attention in many fields (Ab Talib et al., 2021; Poli et al., 2007). Compared with other evolutionary algorithms, the PSO algorithm has the characteristics of fast convergence speed, less setting parameters, extremely simple program implementation, and profound intelligence background. In this research study FLC has been effectively combined with PSO to overcome the limitations of the conventional FLC parameters.

The basic idea of the PSO algorithm is to randomly initialize the particle position and velocity. Using Eq. (5-32) and Eq. (5-33), PSO continuously updates the position and speed of each particle to eventually find the optimal solution of the problem in the given design space. In each iteration, the particle needs to use two extrema: the individual extremum and the global extremum. The so-called individual extremum is the optimal solution of the individual particle up to the current number of iterations while the global extremum is the optimal solution found by the entire population so far. It can be seen that the particle has a memory function and can remember the optimal solution searched by itself. Through continuous updating, the next generation population is generated. In this process, the entire population conducts a comprehensive search of the solution space.

$$v(t + 1) = \omega \times v(t) + c_1 \times r_1 \times (p_{id}(t) - x(t)) + c_2 \times r_2 \times (p_{gd}(t) - x(t)) \quad (5-32)$$

$$x(t + 1) = x(t) + v(t + 1) \quad (5-33)$$

in Eqs. (5-32) and (5-33), ω is the inertia weight, which controls the speed of the particle flight; c_1 and c_2 are the acceleration constants, which are usually taken as 2, r_1 and r_2 are random numbers uniformly distributed in $[0,1]$, p_{id} is the position of the d_{th} dimension of the individual best value of each particle, p_{gd} is the position of the d_{th} dimension of the global best value in the entire population, t is the current iteration number.

Particles cooperate and share information with each other that consists of three parts, which together determine the spatial search direction of the particle. Among them, the first part $\omega \times v(t)$ is the weighted last speed of the particle, indicating the current state of the particle; the second part $c_1 \times r_1 \times (p_{id}(t) - x(t))$ represents the independent thinking ability of the particle, so that the particle has a strong enough global search ability to avoid local minima; the third part

$c_2 \times r_2 \times (p_{gd}(t) - x(t))$ reflects the exchange and sharing of information among particles.

In Eq. (5-32), the value of ω should not be too large or too small as the larger the ω value, the larger the particle's flying speed scalar is. Conversely, very small values of ω , particles tend to perform fine-grained local exploration. A linear decreasing method is adopted as Eq. (5-34), so that the particle swarm has a high global search ability at the beginning, and then the algorithm tends to perform a local search to avoid the oscillation of the larger moving speed in the neighborhood of the optimized solution.

$$\omega = \omega_{\max} - \text{iter} \times \frac{\omega_{\max} - \omega_{\min}}{\text{iter}_{\max}} \quad (5-34)$$

The training algorithm of the PSO-FNN Controller is shown in Figure 5.5. Step 1 to Step 5 are the specific calculation process of PSO and its flowchart as described below.

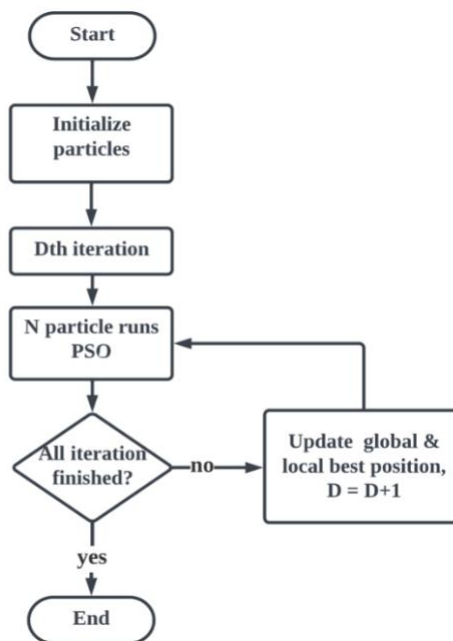


Figure 5.5: Flow chart of PSO algorithm.

Step 1: Parameter setting: fuzzy membership functions' contraction vectors α , β , practical group size N , maximum inertia weight ω_{\max} , minimum inertia weight ω_{\min} , etc., randomly initialize particle velocity.

Step 2: Calculate the fitness value of N particles with the feedforward step of FLC. The fitness value is rms of acceleration of head.

Step 3: Select the individual extreme value p_{id} and the global extreme value p_{gd} according to the fitness value.

Step 4: Update particle velocity and position.

Step 5: Update the particle fitness value to guide the completion of all iterations.

Step 6: Bring the fuzzy parameters α and β that have been globally searched by the PSO algorithm into the FNN.

Step 7: The membership functions of FNN remain unchanged, and the local optimal solution is found by adjusting the weights of the Layer 5 ω^5_i in the fuzzy neural network.

As stated above, 50 initial particles are scattered in a reasonable range of space, and then, the rms value of a_4' output by the seat suspension system within 0.1 second of the different FLCs represented by each particle is used as the fitness value of the PSO. After the training of the set number of iterations, the global optimal setting range of the membership function are found to be 3.1810 and 0.1459 for α and β , respectively.

5.6 Simulation investigation and discussion

In this section, a series of simulations under different external loading excitation modes are implemented and discussed. At the same time, the performance of the developed PSO-FNN controller, ON-OFF controller and passive system are compared. Comparisons are also made in the time domain, frequency domain, with and without ISO 2631/1:1997 based frequency weighting filters and applied control current.

5.6.1 Superimposed Harmonic Excitation

Superposition of sinusoidal excitation, that emulates the main N/rev vibrations on a Bell-412 helicopter as give in Table 5.1, is considered to evaluate the performance of the proposed MRE-based seat suspension and PSO-FNN controller. This excitation provides an approximate profile of the main rotor harmonics across a broad range of flight.

Figure 5.7 provides a comparison of the acceleration of operator's head using the PSO-FNN, ON-OFF and passive control strategies. The comparison is illustrated for both with and without frequency weighting filter. Both the PSO-FNN and the ON-OFF controllers have a very significant vibration isolation effect compared to the passive suspension under the superimposed sinusoidal loadings/disturbances. PSO-FNN controller provides smoother response and slightly lower amplitude compared with on-off controller. The results shown in Figure 5.7, as the maximum vibration amplitude is reduced while the vibration has been significantly isolated using PSO-FNN and ON-OFF control strategies. It is noted that PSO-FNN controller is slightly outperforms ON-OFF controller in reducing the head acceleration an provides smoother acceleration response.

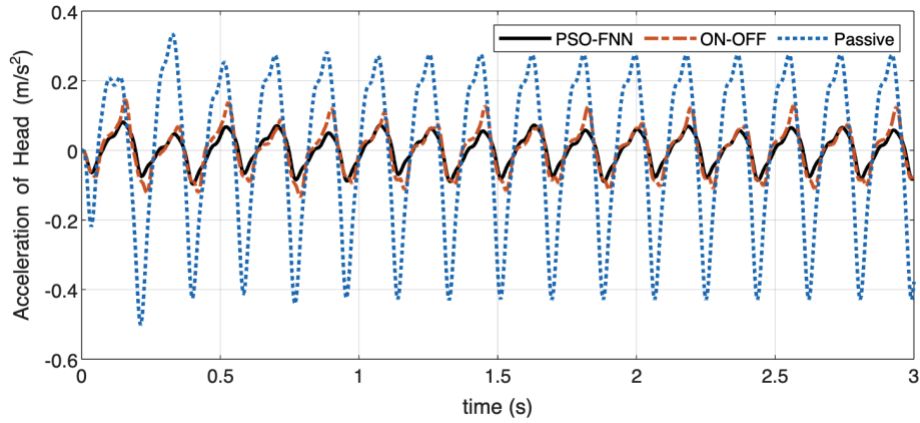


Figure 5.6: Acceleration of head in time domain under harmonic excitation.

The frequency domain analysis under superimposed sinusoidal excitation is also conducted and results are shown in Figure 5.8. It can be realized that the PSO-FNN outperforms in the 3-12 Hz interval, where the human body is most sensitive.

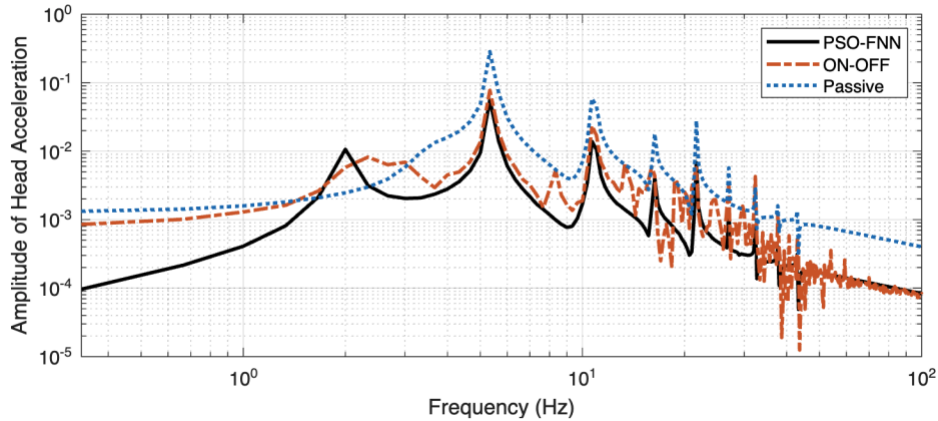


Figure 5.7: Acceleration of head in frequency domain under harmonic excitation.

Figure 5.9 shows the input control current versus time for the PSO-FNN and ON-OFF control strategies. Results clearly show that PSO-FNN requires less control effort even compared with ON-OFF controller. This is of paramount importance as it avoids the temperature rise issue in windings often encountered in practical applications. It is noted that temperature can significantly affect the MRE's viscoelastic properties and subsequently MR effect. Besides, the PSO-FNN is also more environmentally friendly to energy saving as compared to ON-OFF controller, which most of the time demands very high current of 2 A, as shown in Figure 5.9.

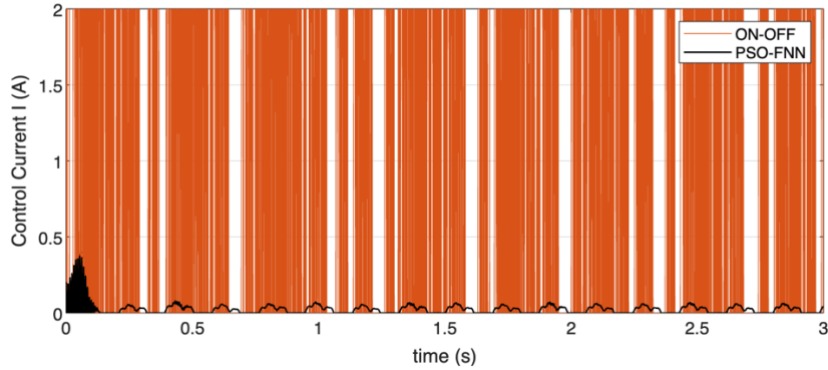


Figure 5.8: The control current for MRE isolator when seat suspension experiences superimposed harmonic excitation as an input.

5.6.2 Random Noise Excitation

A random white noise excitation with 0.223 rms (Fereidooni et al., 2017) is applied to the semi-active seat suspension system in order to evaluate its performance in reducing vibration transmitted to human sitting on the seat.

Figure 5.10 shows the acceleration of the head when human sitting on the seat, subjected to random noise. Results in Figure 5.10 clearly show that the PSO-FNN controller outperform ON-OFF controller. It is not that while PSO-FNN controller has provided significant vibration reduction compared with passive system, on-off controller was not able to provide satisfactory performance.

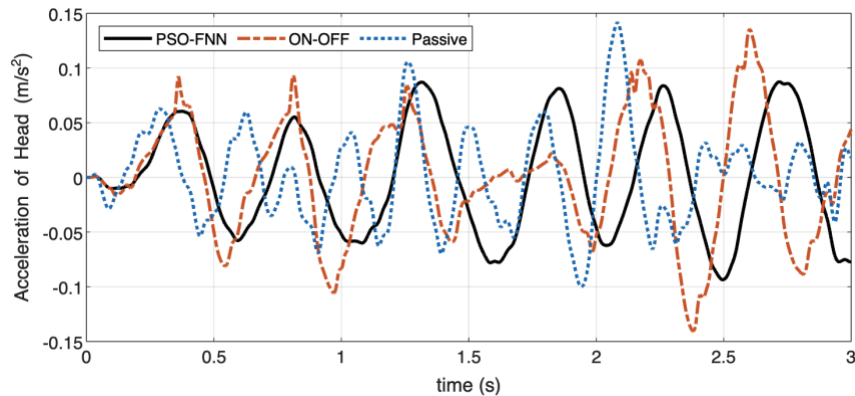


Figure 5.9: Acceleration of head in time domain under random noise excitation.

The frequency spectrum under random vibration is provided in Figure 5.11. As it can be realized, the PSO-FNN controller outperforms best in wide range of frequency, particularly in the most sensitive frequency interval for the human body (4-10 Hz), while the ON-OFF controller

does not even perform as good as the passive suspension, except at very high frequency range.

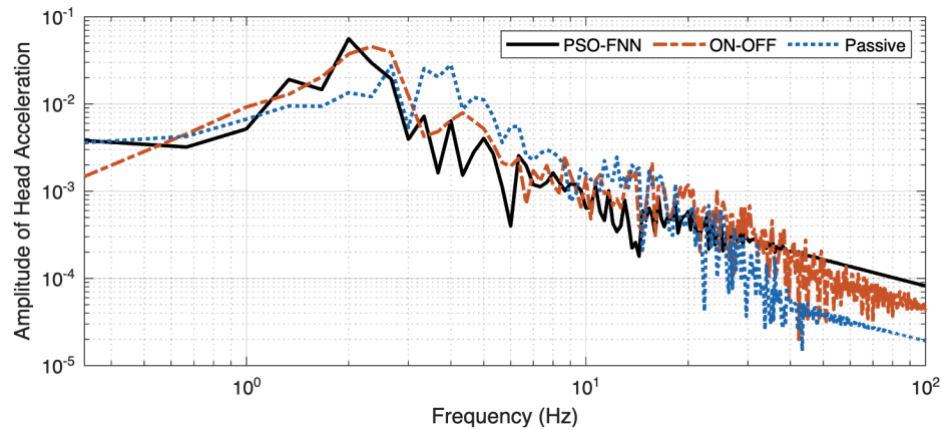


Figure 5.10: Acceleration of head in frequency domain under random noise excitation.

Figure 5.12 shows the required command current control for the ON-OFF and PSO-FNN controllers. It can be observed that the PSO-FNN controller not only provides the best vibration isolation under random vibration, but also saves more power when comparing to the ON-OFF controller.

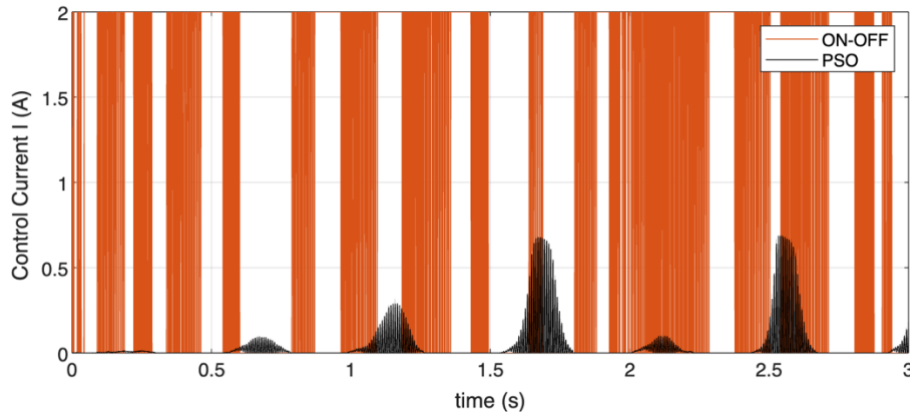


Figure 5.11: Current input under random noise excitation.

5.6.3 Simultaneous application of superimposed harmonics and random noise excitation

The external excitation input that superimposes harmonic vibration with random noise is more in line with the real situation of the helicopter during the flight. This excitation combines superimposed harmonics and random white noise excitations discussed before in previous sections.

Figure 5.13 shows the results for the acceleration of head, in response to a superimposed random and harmonic excitation. Results confirm that the PSO-FNN outperforms the ON-OFF

controller for both cases. Figure 5.14 also shows the frequency domain analysis of the above-mentioned superimposed signals of random and harmonic oscillation. Results generally were indicative of the outperformance of the PSO-FNN controllers in comparison with the ON-OFF and passive strategies within the frequency range that human shows maximum sensitivity (4-10 Hz).

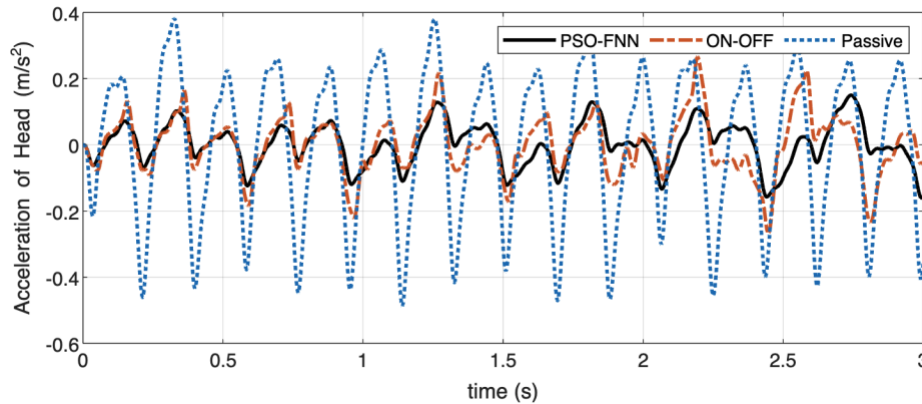


Figure 5.12: Acceleration of head in time domain under harmonic and random noise excitation.

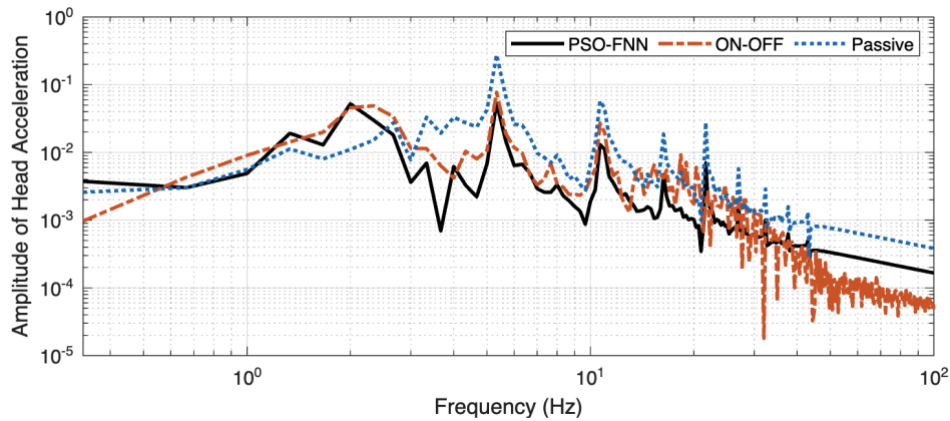


Figure 5.13: Acceleration of head in frequency domain under harmonic random noise excitation.

Figure 5.15 shows the amount of the command current required for implementing the semi-active controllers. Similar to the previous cases, it can be observed that the PSO-FNN demands much less current than that of ON-OFF controller.

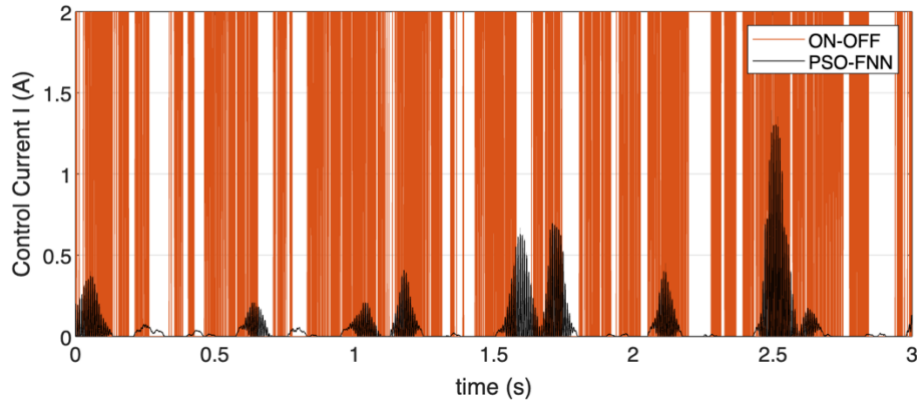


Figure 5.14: Current input under harmonic random noise excitation

5.6.4 Bump Shock Excitation

The bump shock excitation can be described as:

$$x_0 = \begin{cases} \frac{h_0(1-\cos(\omega_0 t 2\pi))}{2} & \frac{6}{\omega_0} \leq t \leq \frac{8}{\omega_0} \\ 0 & \text{otherwise} \end{cases} \quad (5-52)$$

where $h_0 = 0.01\text{m}$ denotes the height of the bump shock transferred to the seat and $\omega_0 = 10 \text{ rad/s}$.

The results presented in Figure 5.16 demonstrates the variation of the human head acceleration in the time domain interval. It can be noticed that the PSO-FNN performs slightly better than the ON-OFF controller in mitigating the head acceleration.

Figure 5.17 provides the corresponding frequency spectrum response of acceleration of the head when the seat is excited by a bump shock. Within the most sensitive range of frequency for human (4-10 Hz), both the controllers reveal relatively the same performance in acceleration reduction of the head, while both dramatically show better performance in comparison with the passive seat suspension.

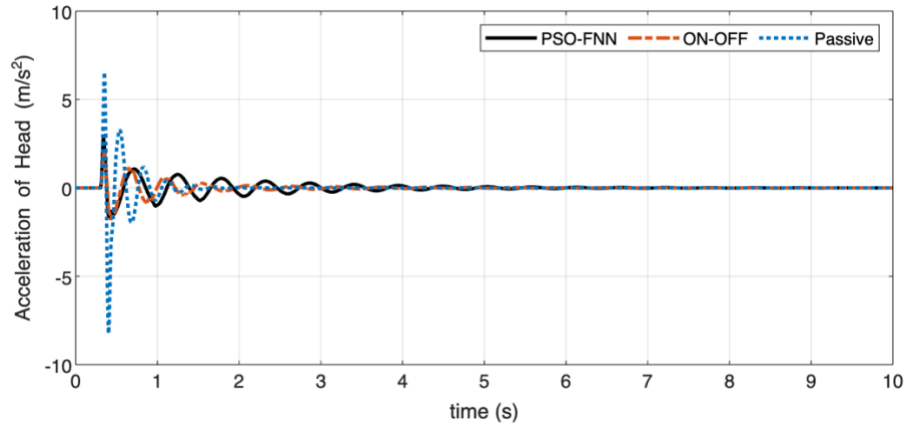


Figure 5.15: Acceleration of head in time domain under bump shock excitation.

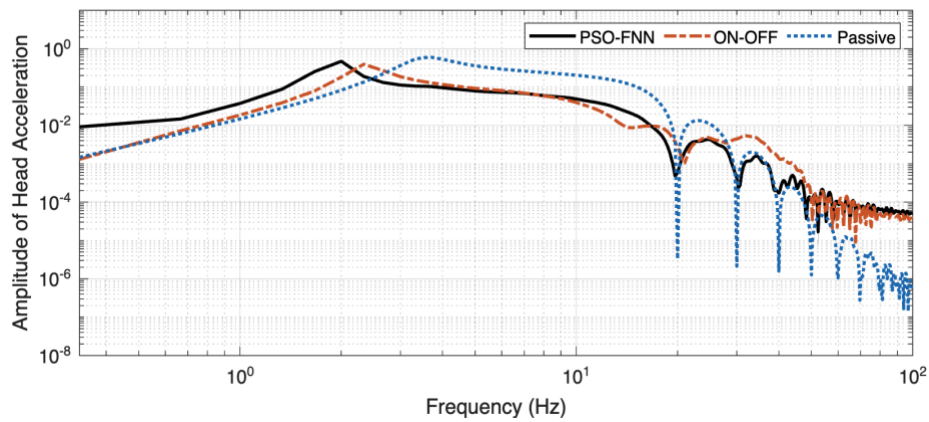


Figure 5.16: Acceleration of head in frequency domain under bump shock excitation.

Figure 5.18 shows the required current by the ON-OFF and PSO-FNN controllers. It can be deduced that for ON-OFF controller the required current command is maximum of 2A after 0.4s, and turns off after 1.7s. Especially from 1.6s to 1.8s, the ON-OFF controller commands a relatively high volume of power consumption, which is not practical as keeping current at the maximum value will lead to overheating of the windings, thereby damaging the electromagnetic circuit of the MRE isolator. On the contrary, PSO-FNN controller needs less current to achieve relatively similar results presented in Figures 5.16 and 5.17 for bump shock. Thus, the PSO-FNN controller is still the best choice for this transient excitation.

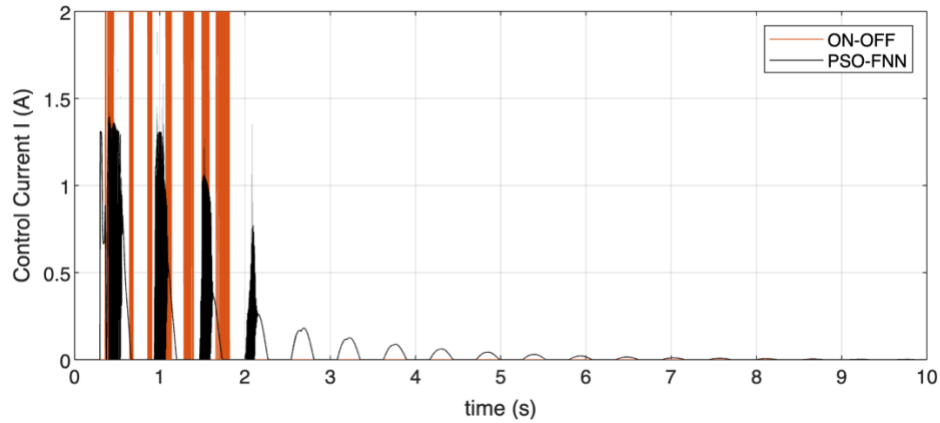


Figure 5.17: Current input under bump shock excitation.

The quantified vibration isolation of the operator’s head under superimposed harmonics combined with random noise excitation and bump shock excitation are investigated using different control strategies. The results are provided in Tables 5.3 and 5.4.

According to Table 5.4, the PSO-FNN and ON-OFF vibration isolation strategies provided sufficient mitigation of the vibration. However, the rms are reduced by 62.59% and 49.51% using PSO-FNN and ON-OFF, respectively compared with passive system. This can quantitatively confirm the outperformance of the proposed PSO-FNN controller compared with the ON-OFF controller.

Table 5.3: Vibration reduction under harmonic and random noise excitation.

	PSO-FNN	ON-OFF	Passive
Weighted rms	0.0652 m/s ²	0.0880 m/s ²	0.1743 m/s ²
Reduction of rms	62.59 %	49.51 %	0 %

Table 5.5 similarly shows the reduction rms when the seat is subjected to the bump shock excitation. Analysis of Table 5.5 reveals that the rms values of PSO-FNN and ON-OFF controller were reduced by 72.69% and 72.22%, respectively, compared with the passive suspension.

Table 5.4: Vibration reduction under bump shock excitation.

	PSO-FNN	ON-OFF	Passive
Weighted rms	0.2547 m/s ²	0.2591 m/s ²	0.9327 m/s ²
Reduction of rms	72.69%	72.22%	0 %

5.7 Conclusion

This chapter mainly presents the implementation of two control strategies for the designed semi-active seat suspension integrated with the MRE isolator subjected to superimposed harmonic, random noise, superimposed harmonic and random noise, and bump shock excitations. The performance of the designed PSO-FNN controller which combines PSO, fuzzy control and neural network has been compared with widely used on-off control strategy. The output acceleration of the human head is discussed in both time and frequency domains. Furthermore, the required control command current for two controllers is discussed considering different excitation inputs. Results generally showed that PSO-FNN slightly outperforms ON-OFF while requiring substantially lower control current compared with ON-OFF controller. And in comparison, PSO-FNN controller provides lower weighted rms than that of ON-OFF controller.

Chapter 6: Conclusion and Future Recommendations

6.1 Conclusion

Helicopter pilots are exposed to various significantly high levels of WBV. The WBV leads to discomfort environment, which are known as the main harmful sources to the operators' health. The main aim of this research study is to reduce the impact of WBV on the aircrew operators by designing a novel MRE-based semi-active seat suspension capable of isolating vibration within the frequency range in which human is most sensitive. Four major steps were taken towards developing the proposed semi-active seat suspension system: 1- To choose a biodynamic human body model in sitting posture to verify the performance of designed semi-active seat suspension system; 2- Optimally design and assess a passive seat suspension system according to the old version of evaluation of WBV standard (ISO 2631/1:1985, ISO 2631/3:1985) and the new version (ISO 2631/1:1997) to investigate the mechanical dynamic effects on the human head; 3- Develop an MRE-based vibration isolator as the adjustable unit to vary the stiffness and damping of the semi-active seat suspension; 4- Propose novel control strategy (PSO-FNN controller) to mitigate the vibration transmitted to the human body so as to improve the comfort level of helicopter pilots under representative vibration.

The 4-DOF human body model proposed by Wan et al., (Wan & Schimmels, 1995) was used in this work as it provides a crucial basis for the design and control of MRE-based semi-active seat suspension. To verify the effect of mechanical properties on the seat suspension system, a 5-DOF passive seat suspension is developed. The 5-DOF model combines the 4-DOF human body model together with a single-DOF seat suspension. To obtain the optimal parameters of the seat, a design optimization was implemented considering the objective function suggested by Wan (Wan, 1998) who considered the frequency weighting factors according to ISO 2631/1:1985. However, in present study the objective function was formulated based on both older version and new version (ISO 2631/1:1997) to investigate the effect of modified frequency weighting factors in the updated new ISO standard. Results of design optimization demonstrated that the stiffness of the seat always converges to the lower bound, while the damping lies within the considered lower and upper bounds. Optimization results show slight decrease in optimal damping and objective function using new standard compared with those based on older version. The transmissibility from cab-floor to head revealed that the passive suspension system based on the ISO 2631/1:1997 weighting factors

performs better than that based on the the older version in the frequency range where the human body' is most sensitive. Therefore, ISO 2631/1:1997 were adopted in the subsequent chapter of related to the design of semi-active seat suspension.

To develop the proposed semi-active seat suspension system, an MRE vibration isolator with a C-shaped core was optimally designed and integrated to the 5 DOF human-seat system. For the design optimization of the MRE isolator, several cylindrical MRE samples were fabricated and characterized in the shear mode using a magneto-rheometer. The tests were performed at different levels of applied flux density from $B = 0$ T to $B = 1$ T over a wide frequency range, from 0.2 Hz to 10 Hz, while the temperature was kept stable at 20 °C. The tests were performed at two different strain amplitude levels (15%, 30%). The elastic and loss moduli of MREs were then identified and modeled as function of frequency and applied magnetic flux density. The findings demonstrated the storage and loss moduli tend to saturate for magnetic flux density beyond 0.9 T. The developed MRE material model is based on 30% strain amplitude due to relatively large deformation of MRE in seat suspension. The designed MRE isolator was capable of changing its stiffness from 8.94 kN/m to 17.5 kN/m within the input current range from 0-2 A.

It is worth noting that in the proposed semi-active seat design, three passive springs, two in parallel and one in series with MRE-base isolator, were also considered to allow large stroke required while preventing MRE to operate at very large deformation, which show nonlinear strain softening behavior. The passive springs were also optimally designed to the maximize the frequency shift of the seat isolator under maximum current.

Finally, a PSO-FNN controller combining particle swarm optimization algorithm, fuzzy logic control and neural network structure is proposed and compared its performance was compared with the conventional ON-OFF controller and passive suspension system in mitigation of transmitted vibration. The PSO-FNN controller has generally showed better vibration isolation performance compared with ON-OFF controller while also required much lower control current under various excitation conditions.

6.2 Future Recommendations

The following main recommendations can be drawn from the simulation and experimental results obtained during the thesis study.

1. The MRE-based “parallel- series” semi-active suspension system was designed with passive springs in series and parallel to the designed MRE isolator in order to prevent MREs undergo

very nonlinear deformation. Developments in new generation of MRE materials may increase the range of their linearity, thereby allowing large deformation, and thus higher vibration isolation performance.

2. A hard magnetorheological elastomer (H-MRE) can be adopted in future work because of its ability to reduce stiffness by applying a magnetic field in the opposite direction. The natural frequency range can thus be expanded compared to the soft MRE material used in this study.
3. Experimental verification of the optimally designed MRE-based suspension systems and also performance evaluation of the proposed PSO-FNN controller in an experiment hardware-in-the loop system would also be important tasks for the future study.

References

- Ab Talib, M. H., Mat Darus, I. Z., Mohd Samin, P., Mohd Yatim, H., Ardani, M. I., Shaharuddin, N. M. R., & Hadi, M. S. (2021). Vibration control of semi-active suspension system using PID controller with advanced firefly algorithm and particle swarm optimization. *Journal of Ambient Intelligence and Humanized Computing*, 12(1), 1119–1137.
- Alem, N. M., Nusholtz, G. S., & Melvin, J. W. (1984). Head and neck response to axial impacts. *SAE Transactions*, 927–940.
- Ballard, M. T., Madison, A. M., & Chancey, V. C. (2020). *Human Response Effects to Whole Body Vibration in Aviation: A Brief Review*.
- Boileau, P.-É., & Rakheja, S. (1998). Whole-body vertical biodynamic response characteristics of the seated vehicle driver: Measurement and model development. *International Journal of Industrial Ergonomics*, 22(6), 449–472.
- Burström, L., Nilsson, T., & Wahlström, J. (2015). Whole-body vibration and the risk of low back pain and sciatica: A systematic review and meta-analysis. *International Archives of Occupational and Environmental Health*, 88(4), 403–418.
- Cesari, D., & Ramet, M. (1982). Pelvic tolerance and protection criteria in side impact. *SAE Transactions*, 3554–3563.
- Chai, Y., Jia, L., & Zhang, Z. (2009). Mamdani model based adaptive neural fuzzy inference system and its application. *International Journal of Computer and Information Engineering*, 3(3), 663–670.
- Chen, Y., Wickramasinghe, V., & Zimcik, D. (2009). Development of adaptive seat mounts for helicopter aircrew body vibration reduction. *Journal of Vibration and Control*, 15(12), 1809–1825.
- Chen, Y., Wickramasinghe, V., & Zimcik, D. G. (2011). Development of adaptive helicopter seat for aircrew vibration reduction. *Journal of Intelligent Material Systems and Structures*, 22(5), 489–502.
- Choi, Y. T., & Wereley, N. M. (2022). Adaptively tunable magnetorheological elastomer-based vibration absorber for a propeller aircraft seat. *AIP Advances*, 12(3), 035332.
- Choi, Y.-T., & Wereley, N. M. (2005). Biodynamic response mitigation to shock loads using magnetorheological helicopter crew seat suspensions. *Journal of Aircraft*, 42(5), 1288–1295.
- Coermann, R. R. (1962). The mechanical impedance of the human body in sitting and standing position at low frequencies. *Human Factors*, 4(5), 227–253.
- Dargahi, A., Sedaghati, R., & Rakheja, S. (2019). On the properties of magnetorheological elastomers in shear mode: Design, fabrication and characterization. *Composites Part B*:

Engineering, 159, 269–283.

- Delahaye, R.-P., Auffret, R., Doury, P., Kleitz, C., & Leger, A. (1982). *Physiopathology and pathology of spinal injuries in Aerospace medicine*. ADVISORY GROUP FOR AEROSPACE RESEARCH AND DEVELOPMENT NEUILLY-SUR-SEINE (FRANCE).
- Delahaye, R.-P., Pannier, R., Seris, H., Auffret, R., Carre, R., & Mangin, H. (1970). *Physiopathology and pathology of affections of the spine in aerospace medicine*. ADVISORY GROUP FOR AEROSPACE RESEARCH AND DEVELOPMENT NEUILLY-SUR-SEINE (FRANCE).
- Du, H., Lam, J., Cheung, K. C., Li, W., & Zhang, N. (2013). Direct voltage control of magnetorheological damper for vehicle suspensions. *Smart Materials and Structures*, 22(10), 105016.
- Du, H., Li, W., & Zhang, N. (2011). Semi-active variable stiffness vibration control of vehicle seat suspension using an MR elastomer isolator. *Smart Materials and Structures*, 20(10), 105003.
- Fereidooni, A., Graham, S., Chen, E., & Wickramasinghe, V. K. (2017). Investigation of a parallel active vibration isolation mount for mitigating N/rev helicopter vibrations. *25th AIAA/AHS Adaptive Structures Conference*, 1441.
- Gagorowski, A. (2012). Controlling the magnetorheological suspension of a vehicle seat including the biomechanics of the driver. *Central European Journal of Engineering*, 2(2), 264–278.
- Gan, Z., Hillis, A. J., & Darling, J. (2013). Development of a biodynamic model of a seated human body exposed to low frequency whole-body vibration. *International Conference on Vibration Problems, -ICOVP*.
- Griffin, M. J., & Erdreich, J. (1991). *Handbook of human vibration*. Acoustical Society of America.
- Hiemenz, G. J., Hu, W., & Wereley, N. M. (2008). Semi-active magnetorheological helicopter crew seat suspension for vibration isolation. *Journal of Aircraft*, 45(3), 945–953.
- ISO 2631/1, 1985, “Evaluation of Human Exposure to Whole-body Vibration — Part 1: General Requirements”, International Organization for Standardization.
- ISO 2631/3, 1985, “Evaluation of Human Exposure to Whole-Body Vibration — Part 3: Evaluation of Exposure to Whole-body z-axis Vertical Vibration in the Frequency Range 0.1 to 0.63 Hz”, International Organization for Standardization.
- ISO 2631/1, 1997, “Mechanical vibration and shock - Evaluation of human exposure to whole-body vibration - Part 1: General requirements”, International Organization for Standardization.
- ISO 5982, 1981, “Vibration and Shock —Mechanical Driving Point Impedance of Human Body”, International Organization for Standardization.

- ISO 7962, 1989, “Vibration and Shock —Mechanical Transmissibility of the Human Body in the z Direction”, International Organization for Standardization.
- Ivers, D. E., & Miller, L. R. (1989). *Experimental comparison of passive, semi-active on/off, and semi-active continuous suspensions*. SAE Technical Paper.
- Jalili, N. (2002). A comparative study and analysis of semi-active vibration-control systems. *J. Vib. Acoust.*, 124(4), 593–605.
- Kazimierczuk, M. K. (2009). *High-frequency magnetic components*. John Wiley & Sons.
- Klir, G., & Yuan, B. (1995). *Fuzzy sets and fuzzy logic* (Vol. 4). Prentice hall New Jersey.
- Krasnicki, E. J. (1981). The experimental performance of an on-off active damper. *Shock and Vibration Information Center The Shock and Vibration Bull, Pt. 1 p 125-131(SEE N 83-10216 01-31)*.
- Kurczyk, S., & Pawełczyk, M. (2013). Fuzzy control for semi-active vehicle suspension. *Journal of Low Frequency Noise, Vibration and Active Control*, 32(3), 217–225.
- Li, W., Zhang, X., & Du, H. (2012). Development and simulation evaluation of a magnetorheological elastomer isolator for seat vibration control. *Journal of Intelligent Material Systems and Structures*, 23(9), 1041–1048.
- Li, Y., Li, J., Li, W., & Du, H. (2014). A state-of-the-art review on magnetorheological elastomer devices. *Smart Materials and Structures*, 23(12), 123001.
- Liang, C.-C., & Chiang, C.-F. (2006). A study on biodynamic models of seated human subjects exposed to vertical vibration. *International Journal of Industrial Ergonomics*, 36(10), 869–890.
- Lin, C., Liu, W., & Ren, H. (2015). Neutral network-PID control algorithm for semi-active suspensions with magneto-rheological damper. *Journal of Vibroengineering*, 17(8), 4432–4444.
- Liu, C., Hemmatian, M., Sedaghati, R., & Wen, G. (2020). Development and control of magnetorheological elastomer-based semi-active seat suspension isolator using adaptive neural network. *Frontiers in Materials*, 7, 171.
- Ma, T., Bi, F., Wang, X., Tian, C., Lin, J., Wang, J., & Pang, G. (2021). Optimized fuzzy skyhook control for semi-active vehicle suspension with new inverse model of magnetorheological fluid damper. *Energies*, 14(6), 1674.
- Meyers, M. (2012). *Shock waves and high-strain-rate phenomena in metals: Concepts and applications*.
- Morillas, J. R., & de Vicente, J. (2020). Magnetorheology: A review. *Soft Matter*, 16(42), 9614–9642.

- Muksian, R., & Nash Jr, C. D. (1974). A model for the response of seated humans to sinusoidal displacements of the seat. *Journal of Biomechanics*, 7(3), 209–215.
- Nguyen, X. B., Komatsuzaki, T., Iwata, Y., & Asanuma, H. (2018). Robust adaptive controller for semi-active control of uncertain structures using a magnetorheological elastomer-based isolator. *Journal of Sound and Vibration*, 434, 192–212.
- Nishiyama, K., Harada, N., Tsujimura, H., Ishitake, T., Sakakibara, H., & Matsumoto, Y. (2012). Relatedness of occupational exposure to whole-body vibration and health, principally back symptoms. *Sangyo Eiseigaku Zasshi= Journal of Occupational Health*, 54(4), 121–140.
- Oh, H. E., Park, D. J., Park, J. P., Ahn, S. J., & Jeong, W. B. (2017). Digital filter design of frequency weighting function to measure and assess human vibration. *Noise Control Engineering Journal*, 65(3), 183–190.
- Pang, H., Liu, F., & Xu, Z. (2018). Variable universe fuzzy control for vehicle semi-active suspension system with MR damper combining fuzzy neural network and particle swarm optimization. *Neurocomputing*, 306, 130–140.
- Poli, R., Kennedy, J., & Blackwell, T. (2007). Particle swarm optimization. *Swarm Intelligence*, 1(1), 33–57.
- Qi, S., Yu, M., Fu, J., Zhu, M., Xie, Y., & Li, W. (2018). An EPDM/MVQ polymer blend based magnetorheological elastomer with good thermostability and mechanical performance. *Soft Matter*, 14(42), 8521–8528.
- Rakheja, S., Dewangan, K. N., Dong, R. G., & Marcotte, P. (2020). Whole-body vibration biodynamics-a critical review: I. Experimental biodynamics. *International Journal of Vehicle Performance*, 6(1), 1–51.
- Rakheja, S., Dewangan, K. N., Dong, R. G., Marcotte, P., & Pranesh, A. (2020). Whole-body vibration biodynamics-a critical review: II. Biodynamic modelling. *International Journal of Vehicle Performance*, 6(1), 52–84.
- Rakheja, S., & Sanka, S. (1986). *Effectiveness of on-off damper in isolating dynamical systems. Shock and Vibration Bulletin*, Vol. 57, pp. 146-156, 1986.
- Rimell, A. N., & Mansfield, N. J. (2007). Design of digital filters for frequency weightings required for risk assessments of workers exposed to vibration. *Industrial Health*, 45(4), 512–519.
- Stelzer, G. J., Schulz, M. J., Kim, J., & Allemang, R. J. (2003). A magnetorheological semi-active isolator to reduce noise and vibration transmissibility in automobiles. *Journal of Intelligent Material Systems and Structures*, 14(12), 743–765.
- Sun, S. S., Chen, Y., Yang, J., Tian, T. F., Deng, H. X., Li, W. H., Du, H., & Alici, G. (2014). The development of an adaptive tuned magnetorheological elastomer absorber working in

- squeeze mode. *Smart Materials and Structures*, 23(7), 075009.
- Sun, S. S., Yang, J., Deng, H. X., Du, H., Li, W. H., Alici, G., & Nakano, M. (2015). Horizontal vibration reduction of a seat suspension using negative changing stiffness magnetorheological elastomer isolators. *International Journal of Vehicle Design*, 1–3, 104–118.
- Sutrisno, J., Purwanto, A., & Mazlan, S. A. (2015). Recent progress on magnetorheological solids: Materials, fabrication, testing, and applications. *Advanced Engineering Materials*, 17(5), 563–597.
- Takagi, T., & Sugeno, M. (1985). Fuzzy identification of systems and its applications to modeling and control. *IEEE Transactions on Systems, Man, and Cybernetics*, 1, 116–132.
- Truszczyńska, A., Lewkowicz, R., Truszczyński, O., Rapala, K., & Wojtkowiak, M. (2012). Back pain in Polish military helicopter pilots. *International Journal of Occupational Medicine and Environmental Health*, 25(3), 258–264.
- Vatandoost, H., Norouzi, M., Alehashem, S. M. S., & Smoukov, S. K. (2017). A novel phenomenological model for dynamic behavior of magnetorheological elastomers in tension–compression mode. *Smart Materials and Structures*, 26(6), 065011.
- Vatandoost, H., Rakheja, S., Sedaghati, R., & Hemmatian, M. (2020). Compensation of magnetic force of an electromagnet for compression mode characterization of magnetorheological elastomers. *IEEE Transactions on Magnetics*, 57(1), 1–14.
- Vidya, V., & Dharmana, M. M. (2017). Model reference based intelligent control of an active suspension system for vehicles. *2017 International Conference on Circuit, Power and Computing Technologies (ICCPCT)*, 1–5.
- Wan, Y. (1998). *An investigation into linear and nonlinear optimal seat suspension designs*. Marquette University.
- Wan, Y., & Schimmels, J. M. (1995). A simple model that captures the essential dynamics of a seated human exposed to whole body vibration. *Advances in Bioengineering*.
- Wan, Y., & Schimmels, J. M. (1997). *Optimal seat suspension design based on minimum “simulated subjective response.”*
- Wei, L., & Griffin, J. (1998). The prediction of seat transmissibility from measures of seat impedance. *Journal of Sound and Vibration*, 214(1), 121–137.
- Wickramasinghe, V. K. (2013). *Dynamics control approaches to improve vibratory environment of the helicopter aircrew*. Carleton University.
- Yang, J., Du, H., Li, W., Li, Y., Li, J., Sun, S., & Deng, H. X. (2013). Experimental study and modeling of a novel magnetorheological elastomer isolator. *Smart Materials and*

Structures, 22(11), 117001.

Yang, J., Sun, S., Tian, T., Li, W., Du, H., Alici, G., & Nakano, M. (2016). Development of a novel multi-layer MRE isolator for suppression of building vibrations under seismic events. *Mechanical Systems and Signal Processing*, 70, 811–820.

Yarra, S., Gordaninejad, F., Behrooz, M., Pekcan, G., Itani, A. M., & Publicover, N. (2018). Performance of a large-scale magnetorheological elastomer-based vibration isolator for highway bridges. *Journal of Intelligent Material Systems and Structures*, 29(20), 3890–3901.

Zhang, W., Ma, Z., Jin, A., Yang, J., & Zhang, Y. (2015). An improved human biodynamic model considering the interaction between feet and ground. *SAE International Journal of Commercial Vehicles*, 8(2015-01-0612), 13–19.

Zhongyu, Z., Xie, W., & Hong, H. (2008). Identification of Takagi-Sugeno (TS) fuzzy model with evolutionary parallel gradient search. *NAFIPS 2008-2008 Annual Meeting of the North American Fuzzy Information Processing Society*, 1–6.